SURFACE ANALYSIS OF POLYMER BLENDS

by

Stuart Thomas Jackson

A thesis presented for the degree of

Doctor of Philosophy

December 1992

Department of Engineering Materials

Faculty of Engineering

University of Sheffield

ABSTRACT

A surface analysis study was performed on poly(vinyl chloride) (PVC), poly(methyl methacrylate) (PMMA) and their blends, using X-ray photoelectron spectroscopy (XPS) and time of flight secondary ion mass spectroscopy (ToFSIMS). Miscible blends were prepared by solution casting from butan-2-one, immiscible blends were prepared by spin casting and solution casting from tetrahydrofuran. ToFSIMS studies on different areas of homo-PMMA showed that the method of partial quantification used, normalization of peak intensities (NPI's), gave standard errors within ±2% for elemental and quasi-elemental ions, and ±5% for molecular ions. NPI-ion dose profiles were obtained for specific ions for PMMA and PVC, and for poly(cyclic aromatic) (PCA) ions. These studies showed that (1) the fragmentation routes of ions with similar profiles can be related, (2) the limit of the static SIMS regime is dependent on the secondary ion being observed, (3) PCA ions are detectable at relatively low ion doses, and (4) beyond an ion dose of *ca.* 7×10^{13} ions cm^{-2}, PVC and PMMA graphitize at the surface. Studies on miscible PVC/PMMA blends showed that there was a slight surface enrichment of PMMA across the blend composition range. This did not manifest itself as a complete surface overlayer and was probably due to differences in surface free energy. This part of the study exposed possible limitations in the NPI method which need to be addressed in future studies. An ion that was due to both polymers in the miscible blend was observed at m/z=51$^-$ and assigned to ClO^-. The NPI-bulk composition plot for this ion reached a maximum near the centre of the composition range. Surface enrichment of PMMA was also found to be in evidence for immiscible PVC/PMMA blends. This was due to differences in specific gravities of the homopolymers. The domain diameters of the dispersed phase were found to be dependent on the rate of solvent removal. Imaging of phase separated surfaces by ToFSIMS was achieved across the composition range. Comparison of these images with microanalytical and imaging XPS showed that improved lateral resolution was available to ToFSIMS imaging. At the film/glass interface for blends cast directly into petri dishes, PDMS contamination and residual solvent were observed. Doubts remain as to the sampling depth for elemental ions by ToFSIMS.

CONTENTS

ACKNOWLEDGEMENTS

It gives me deep pleasure to acknowledge the people who have helped me to reach this stage. First I would like to thank those who were directly involved with this research project: Robert Short, my supervisor, whose enthusiasm and excellent supervision has been a key factor in determining the success of this research; Hugh Munro, my industrial supervisor, for external guidance of the project and many useful discussions; Suky Singh and Bob Litchfield at Courtaulds PLC, for Kratos Prism ToFSIMS instrument time (when ours was down) and DSC respectively; Dave Briggs, Graham Beamson, and Stan Davies at ICI's Wilton Research Centre, for VG ESCASCOPE and Scienta ESCA300 instrument time; Martin Davies and Andrew Tudor at the University of Nottingham for Raman-IR instrument time; Ercan Adem and Nicki Forsyth at Fisons Surface Science for VG ESCASCOPE instrument time; Marisa Fernandez at Imperial College, for providing PS/PVME samples (which didn't actually make it to the thesis, but were useful all the same!); Frank Jones for his useful discussions and supervision during my Masters Degree (thanks in this respect also go to Bryan Ellis); Paul Denison, for initial guidance in the use of the ToFSIMS and XPS instruments; Jose Luis Angulo Sanchez for helping me get to grips with polymer blend thermodynamics; Bev Lane for help with the DSC; Peter Korgul and Dawn Bussey for guidance in the use of SEM; and finally for their joint contributions to our knowledge base, the other members of the Sheffield Surface Science group who are at present, Alison Ward, Amir Ameen, Danghan Wang, Chris Barran, Martin Horsley, and Malcolm Butler, and who were in the past, Morgan Alexander, Dave Pawson and Liam O'Toole. This project was jointly funded by a University of Sheffield Scholarship and sponsorship from Courtaulds PLC. To both institutions, a big thank you. Not directly involved with the project, but still vitally important, were the following people: Frances Upchurch for masses of help with references and general library services; Carole Plant and her collegues for secretarial services; Ian Watts, Graham Hough, Pat Brookes, Frank Fletcher, Ian Lomas, Gordon Waddams and Jim Smedley for technical assistance; Denise Jordan from Academic Computing Services, who patiently guided me through no less than two spreadsheet and three word processing packages; and to everyone in the Elmfield building for making it such a good place to work. A special debt of gratitude is owed to Diana Bennett and her family, for providing me with accomodation at a time of great need. My brother John is thanked for letting me use his room when I was writing up, and for helping me to make some of the diagrams. To everyone who helped me at Fisher-More, Widnes Sixth Form College, Hull University and VSEL...you are all gratefully acknowledged.

Lots of love and thanks go to Jodi, for all her encouragement, inspiration and support during this unbelievably busy time.

Many, many thanks also go to everyone in my family, both in the US and over here, for all sorts of kindness. Especially my mum, Monica, who's always had the uncanny knack of knowing what's best! This work is dedicated to her, with much love.

CHAPTER ONE - Introduction

The blending of polymers to obtain new materials has gained increasing importance in the polymer industry in recent years. The main driving forces for this are the relative cheapness and versatility that this option provides for the industrialist. The ability to physically mix two existing products in some way rather than having to chemically synthesize a new material can involve considerable financial savings. The versatility of blending arises from the capability of varying impact resistance or processability characteristics of the final material by a simple change in blend composition.

One of the difficulties involved in blending is that very few polymer-polymer pairs can produce a homogeneous final material. This depends on the miscibility of the polymers, *i.e.* whether the polymers can mix intimately at a molecular level. Immiscibility of a polymer blend does not however preclude it from use, and many phase separated polymer blends have found use in various engineering and general purpose applications.

Whereas the bulk properties of many polymer blends have been extensively investigated, very few blends have had their surface properties examined. The surface structure of a material, which can differ markedly from that of the bulk, has a large influence on its surface properties. In order to have a greater understanding of such properties it is necessary to obtain a knowledge of the chemical structure of the surface.

In the past two decades, the most common surface analysis as applied to polymer surfaces has been that of X-ray photoelectron spectroscopy (XPS). This technique has the ability to probe the surface to a depth of 10nm. Over the last ten years, a more surface sensitive technique has developed which has been applied to polymers, namely static secondary ion mass spectroscopy (SSIMS). This provides analysis of surfaces to a depth of *ca.* 1nm.

While some polymer blends have had their surfaces analysed by XPS, prior to this study, no blend had been examined by SSIMS. The objective of this study was to extend the surface analysis of polymer blends to include the use of SSIMS. The approach used was combined analysis of blends using XPS and ToFSIMS (a SSIMS instrument with a time-of-flight mass analyser). The blend system chosen for examination was that of poly(vinyl chloride) (PVC) and poly(methyl methacrylate), a system which under different preparation conditions can produce miscible and immiscible blends.

In this thesis, following an overview of polymer blends and the associated thermodynamical principles involved in mixing polymers, a summary of the techniques

involved and previous surface studies on polymer blends is presented. The experimental section covers three separate areas of the research project. The first is involved with surface studies on the homopolymers, with particular emphasis on the effects of primary ion dose on secondary ion formation. The second area looks at surface studies on miscible blends. The third area examines immiscible blends.

CHAPTER TWO - Polymer Blends

2.1 Classification of polymer-polymer mixtures

Before a detailed treatise on polymer blends is presented it is necessary to distinguish the various classes of polymer-polymer mixtures in order to establish the type of materials which are within the scope of this study.

2.1.1 Blends

Polymer blends in general comprise of two distinct polymeric components which are in some way mixed or blended together. The resulting material can be either single phase or two phase. Whether homogeneity or heterogeneity exists in a polymer blend is dependant on the miscibility of the two components, *i.e.*, the ability of the two components to mix intimately at a molecular level. Most commercial polymer blends available at present are immiscible, heterogeneous materials in which a dispersed phase is contained within a continuous matrix phase. Some miscible single phase blends are available but these are commercially rare. The reasons for the comparative lack of miscible blends can be explained by examining the thermodynamics of polymer blends, which will be done in sections 2.3 and 2.4. Both miscible and immiscible polymer blends are examined in this study.

2.1.2 Copolymers

Three types of copolymer exist; block, graft and star-block copolymers. They differ from polymer blends by virtue of covalent bonding existing between dissimilar polymer types on the same macromolecule. With block copolymers two or more types of monomer can be polymerised within the same linear chain. With graft copolymers, side chains of one monomer type are polymerised at reaction sites on a linear chain of a different polymer type. The reaction sites on the main chain are usually dienes. Star-block copolymers consist of a multifunctional central molecule from which three or more individual block copolymer chains can be polymerised. Although copolymers are extremely important within the polymer industry they are only considered here if they form one component of a simple blend.

2.1.3 Interpenetrating networks (IPN's)

IPN's are materials in which two dissimilar polymeric chains form interlocking ring structures. There are a number of ways of preparing such mixtures and all include a crosslinking stage. These materials do not have great commercial importance, but have been used academically to study the thermodynamics of miscibility. IPN's are not considered in this study.

2.2 The role of polymer blends in the polymer industry

In the early days of polymer science, most research was aimed at synthesising new monomer structures for polymerisation. In recent times, more effort has been directed towards the modification of existing monomers and polymers. One route is that of blending.

The attractiveness of blending to the polymer industry is obvious. The possibility of obtaining new materials relatively simply without developing a new chemistry is a strong commercial driving force.

For thermodynamic reasons, most polymer-polymer pairs are immiscible. Miscibility however is not a prerequisite for utility, which is fortunate because, as already mentioned, the vast majority of commercially available polymer blend systems are immiscible polymer pairs.

There are two primary reasons for blending polymers; to improve impact resistance or to improve processability characteristics. Both properties cannot usually be improved simultaneously.

2.2.1 Immiscible Blends

The primary utility of heterogeneous polymer blends is their ability to improve the impact strength of glassy polymers. The glassy polymer forms the matrix phase. The secondary "domain" phase usually consists of discrete elastomeric beads dispersed through the matrix. Consequently these blends are sometimes known as "rubber toughened" polymers.

A prime example of such blends is high impact polystyrene (HIPS). This is polystyrene toughened by polybutadiene rubber. Conventional mixing of these polymers using a two-roll mill or a Banbury mixer leads to an unsuccessful blend. The reason for this is that such mixing does not bestow mechanical compatibility to the blend, *i.e.*, there is no adhesion between the dispersed phase and the matrix. The only successful way to blend is to dissolve the rubber in styrene monomer and polymerise *in situ*. As the rubber is a polymer diene, styrene can react at the double bonds in the polybutadiene backbone and limited graft copolymerisation occurs. The final material is not classed as a copolymer

as only a small amount of styrene/butadiene copolymer exists at the interfaces between the homopolystyrene matrix and the dispersed gelled rubber phase.

Another highly successful commercial blend is that of ABS, acrylonitrile butadiene styrene, a blend which unlike HIPS, is tough enough to be used in engineering applications. There are two main routes to obtaining ABS. The first route involves mixing polybutadiene on a two roll mill with styrene acrylonitrile polymer (SAN). The second route involves *in situ* polymerisation of SAN in a polybutadiene latex. The different routes give different ultimate properties.

The success of rubber toughened polymers is due to their toughening mechanisms. These are based on a combination of multiple crazing within the glassy matrix and shear yielding at the rubber particle sites.

2.2.2 Miscible Blends

The major utility of single phase polymer blends is that of improving processability. As there is intimate mixing, mechanical compatibility of the components is assured.

The initial observation of polymer-polymer miscibility was made by Emmett [1] as long ago as 1944. This followed the patenting two years earlier [2] of a blend of poly(vinyl chloride) (PVC) and butadiene-acrylonitrile copolymer (nitrile rubber). It was subsequently observed that nitrile rubber could act as a very efficient high molecular weight plasticiser for PVC. The conventional PVC plasticiser, dioctyl phthalate (DOP) was not appropriate for some applications. Due to the high volatility of DOP (a result of its low molecular weight and migration behaviour), plasticiser loss was being experienced in some PVC applications. This was of particular concern in the cable and food packaging industries. Nitrile rubber, with its high molecular weight and natural mechanical compatibility was an ideal plasticiser for PVC in these applications.

If nitrile rubber blended with PVC was the first commercially successful miscible blend, without doubt the *most* successful miscible blend has been that of poly(phenylene oxide) (PPO) and polystyrene (PS). PPO was first introduced in 1964 by General Electric as a tough, temperature resistant engineering thermoplastic. Unfortunately one of the problems found with this high glass transition temperature (195°C) material was its fabrication limitations. The injection moulding temperatures required (>210°C) made the pendant methyl groups subject to oxidation. It was found that melt mixing the PPO with small amounts of polystyrene gave a miscible blend with a single glass transition temperature, a major characteristic of a miscible polymer blend, between that of PPO and PS (T_g=95°C). Additionally, inert fillers could be added to reduce the total cost of the final material, without significantly altering the final properties of the blend. This blend was patented by General Electric in 1968 under the trade name Noryl [3]. The material is extremely versatile, is easier to process than PPO and is higher in heat resistance and toughness than polystyrene. It is available in a number of compositions, each one tailored to different applications and is used in numerous engineering plastic situations where toughness and heat resistance are required.

In the field of metallurgy, for most of this century, much research has been concentrated on obtaining new alloys in order to develop new materials for improved performance in various applications. It is only comparatively recently that the same thing has happened in the polymer industry. The driving force of improved price/performance behaviour will continue the research into new blends. The result of this will be that more miscible blends will find their way into the commercial market.

2.3 Polymer blend thermodynamics: an introduction

In order to understand the behaviour of polymer blends more completely, for example, why phase separation occurs in some blends and not in others, it is necessary to discuss the thermodynamics of mixing of the polymers.

The following discussion is based on four reviews of polymer blend thermodynamics by Fernandez [4], Olabisi *et al* [5], Carpenter[6] and Orwoll[7], and describes the development of various models which take into account the numerous thermodynamic characteristics of polymer mixing. Such characteristics include miscibility, immiscibility and different types of phase separation mechanisms, volume changes on mixing, positive and negative deviations from Raoult's law, asymmetry in coexistence curves, and both upper and lower critical solution temperature behaviour. These terms will be explained and examined as the discussion progresses.

2.3.1 Free energy of mixing

Processes in nature are governed by the optimisation of free energy, which consists of enthalpic and entropic contributions. When mixing two components at temperature T, the change in Gibbs free energy of mixing [8] is given by

$$\Delta G_{mix} = \Delta H_{mix} - T\Delta S_{mix} \qquad ...(2.1)$$

where ΔH_{mix} is the change in enthalpy, a measure of heating changes during mixing, and ΔS_{mix} is the change in entropy, the change of the degree of disorder resulting from mixing . If on mixing there is a reduction of total free energy then ΔG_{mix} is negative. Such a reduction in free energy is favourable for mixing of components. The condition that ΔG_{mix} is less than zero is necessary, but not a sufficient condition for miscibility, and this will be examined in the next section. At this early stage however, a superficial examination of the terms involved in this equation can give us an indication of why most polymer-polymer pairs are immiscible.

Consider a two component (binary) mixture of molecules A and B. Both are small molecules with low molecular weight. Imagine that six molecules of A and six molecules of B can be isolated, are all of the same size and can be placed on a simple lattice in any order, as in figure 2.1(a). There are a large number of combinations of

positioning all of the molecules on the lattice. The disorder that results on mixing molecules A and B is therefore great compared to the unmixed components.

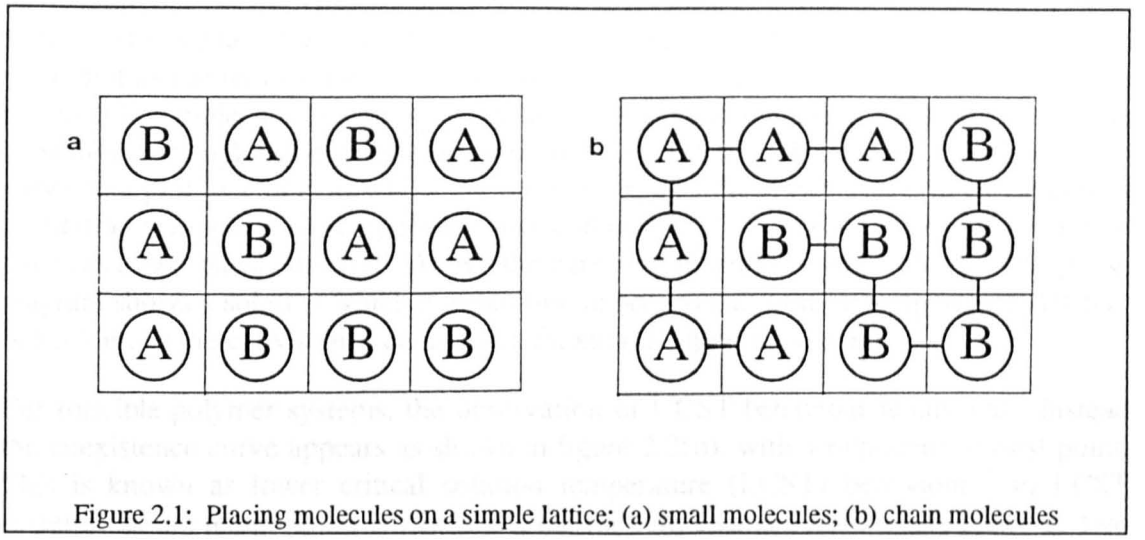

Figure 2.1: Placing molecules on a simple lattice; (a) small molecules; (b) chain molecules

Now consider that the six molecules of A and the six molecules of B are bound together in two chains, one of A and one of B. When these are positioned on the lattice, as in figure 2.1(b), the number of combinations are markedly reduced if the chain-like nature is to be retained. Therefore the degree of disorder that results from mixing chain-like molecules is much less than that of the low molecular weight components. This is a very simplistic view of a highly complex situation, but it does indicate that with high molecular weight components, the entropy gain on mixing is much less than when using components of low molecular weight.

In equation 2.1 the $T\Delta S_{mix}$ term is subtracted.* Any positive value of $T\Delta S_{mix}$ contributes to reducing ΔG_{mix} but the entropy gain is so small with high molecular weight components that, even taking into account high temperatures of mixing, this term can be negligible in comparison with low molecular weight counterparts.

The enthalpy term is essentially a measure of the heat changes that take place on mixing. When components A and B are mixed, three different enthalpic situations can arise: (i) heat is evolved into the surroundings; (ii) no net heat change occurs; or (iii) heat is absorbed from the surroundings. The convention used in thermodynamics for these three cases is that enthalpy is (i) negative, (ii) zero or (iii) positive. A positive enthalpy (endothermic reaction) is unfavourable to mixing. A negative enthalpy (exothermic reaction) is favourable to mixing and implies some form of intermolecular interaction between the two components.

As the contribution to the free energy of mixing by the entropic contribution is so small when using high molecular weight components, it is the enthalpic term which usually dominates the free energy, and determines whether it is negative or positive. Only a very few polymer-polymer pairs can specifically interact at a molecular level and therefore give a negative free energy of mixing.. The vast majority of binary polymer mixtures undergo endothermic or negligible heat changes on mixing, making the free energy positive. This is why so many polymer blends are immiscible pairs.

* which makes ΔG_{mix} more negative

2.3.2 Critical solution temperature behaviour

As there is a temperature term in equation 2.1, mixing is a temperature dependent phenomenon. As the temperature increases the $T\Delta S_{mix}$ increases and as this term is subtracted in equation 2.1, as the term gets bigger, ΔG_{mix} reduces. It would therefore seem that as the temperature increases, mixing should improve. This is in fact the case for most low molecular weight systems and many homopolymers in solution. The phase behaviour for such systems is illustrated in figure 2.2(a). This shows the coexistence curve (the plot of points at which the mixture changes from two phase to single phase) plotted as a function of temperature and composition. Below this curve the solution exists as a two phase material. Above the curve the material is single phase. This phase diagram shows a solution which is exhibiting upper critical solution temperature (UCST) behaviour, as the coexistence curve has a maximum, uppermost point.

For miscible polymer systems, the observation of UCST behaviour is unusual. Instead the coexistence curve appears as shown in figure 2.2(b), with a minimum, lowest point. This is known as lower critical solution temperature (LCST) behaviour. In LCST systems, as the temperature is increased, the mixture changes from single phase to two phase. This seems to contradict the initial impression from equation 2.1 that mixing increases with temperature. However, when the ideas from the previous section are taken into account, LCST behaviour in such systems seems more reasonable. As already stated, entropy gains are negligible in high molecular weight mixtures, regardless of temperature, so the contribution to ΔG_{mix} from the temperature/entropy term is minimal. For a miscible polymer blend, enthalpy is generally negative due to favourable specific interactions between the component molecules. As the temperature increases, molecular vibrations can break down these often weak interactions and hence cause demixing of the blend.

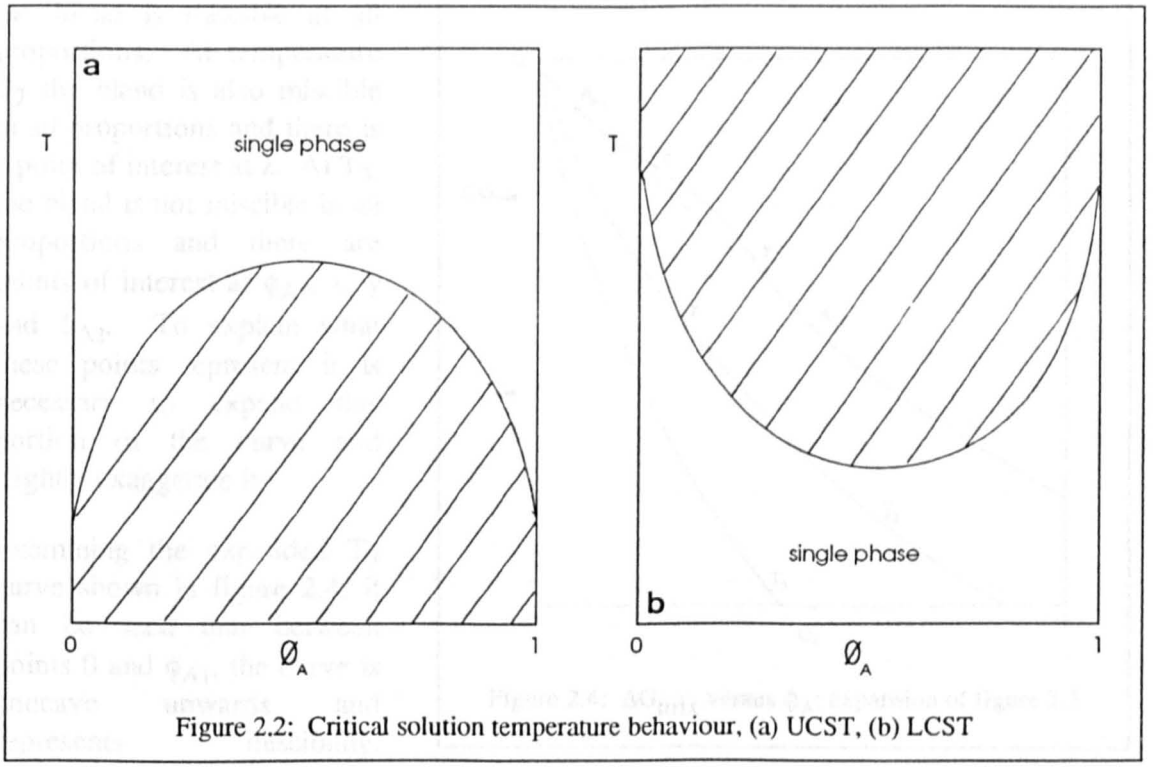

Figure 2.2: Critical solution temperature behaviour, (a) UCST, (b) LCST

Coexistence curves are in reality more complex than indicated in figure 2.2. To examine coexistence curves more closely and at the same time explain the *criticality* of the solution temperature, composition and temperature dependence of the free energy of mixing must be addressed.

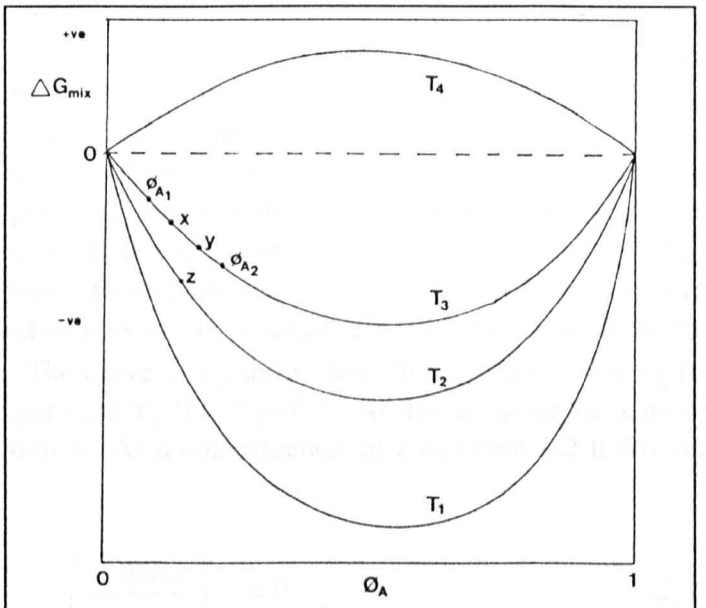

Figure 2.3: ΔG_{mix} versus ϕ_A for four different temperatures

Figure 2.3 shows four plots of ΔG_{mix} versus composition ϕ_A (equal to $1-\phi_B$) at temperatures T_1, T_2, T_3 and T_4. ΔG_{mix} is positive for all compositions at T_4 and represents a temperature at which the blend is totally immiscible. The curves shown at temperatures T_1, T_2 and T_3 all give negative values for ΔG_{mix} for all compositions. At temperature T_1 the curve is concave upwards at all compositions. Upward concavity in the free energy/composition curve is an additional requirement for miscibility, *i.e.*,

$$\left(\frac{d^2\Delta G}{d\phi_A^2}\right)_{P,T} = 0 \qquad \ldots(2.2)$$

Therefore, at temperature T_1, the blend is miscible at all proportions. At temperature T_2 the blend is also miscible in all proportions and there is a point of interest at z. At T_3, the blend is not miscible in all proportions and there are points of interest at ϕ_{A1}, x, y and ϕ_{A2}. To explain what these points represent it is necessary to expand this portion of the curve and slightly exaggerate it.

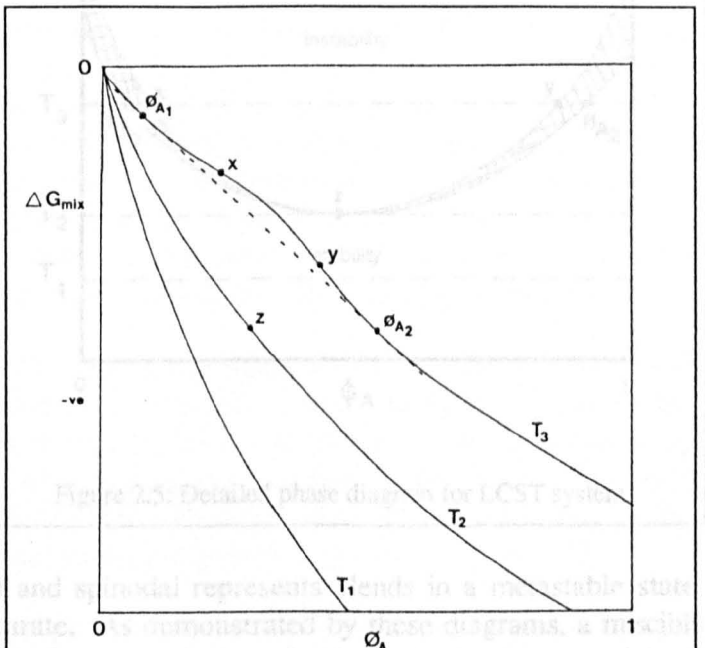

Figure 2.4: ΔG_{mix} versus ϕ_A; expansion of figure 2.3

Examining the expanded T_3 curve shown in figure 2.4, it can be seen that between points 0 and ϕ_{A1}, the curve is concave upwards and represents miscibility.

Beyond ϕ_{A1} the curve is still concave upwards until an inflection point occurs at x. Beyond this point the curve is concave downwards until another inflection point is reached at y, at which point the curve begins to be concave upwards again. Beyond point ϕ_{A2} the system is miscible in all proportions. Points ϕ_{A1} and ϕ_{A2} occur at minima in the two upwardly concave sections of the curve. This can be seen as the dashed line drawn through these points being tangential to the curve. Between points x and y, the lowest free energy is achieved by the system forming a second phase at concentration ϕ_{A2} in equilibrium with the first phase at concentration ϕ_{A1}. The mixture is therefore immiscible between these two points. Between points ϕ_{A1} and x, and points y and ϕ_{A2}, a single phase solution occurs which is metastable with respect to the two phase system. ϕ_{A1} is known as the solubility limit of polymer B in polymer A, and ϕ_{A2} is the solubility limit of polymer A in polymer B. The curve at T_2 shows how ΔG_{mix} varies with ϕ_A for a binary system at its critical temperature T_c (*i.e.* $T_2=T_c$). At this temperature x and y coalesce at the critical concentration z. As a consequence, at z equation 2.2 holds and additionally,

$$\left(\frac{d^3\Delta G_{mix}}{d\phi_A^3}\right)_{T,P} = 0 \qquad ...(2.3)$$

We can transfer this information to make a more detailed phase diagram. Figure 2.5 shows the phase diagram for a blend exhibiting LCST behaviour. It is similar to that shown in figure 2.2(b) except that the coexistence curve between single phase and two phase regions is now a shaded area bounded by a solid and a dashed line. The solid line is the locus of all points ϕ_{A1} and ϕ_{A2} and is known as the binodal curve. The dashed line is the locus of all points x and y and is called the spinodal curve. Blend compositions raised to temperatures above the spinodal will be unstable and will phase separate. Below the binodal, the blends are stable, single phase compositions. The shaded area between the binodal and spinodal represents blends in a metastable state, which may or may not phase separate. As demonstrated by these diagrams, a miscible blend will phase separate on heating, but the mechanism of phase separation is dependant on which temperature/composition point the blend is heated to.

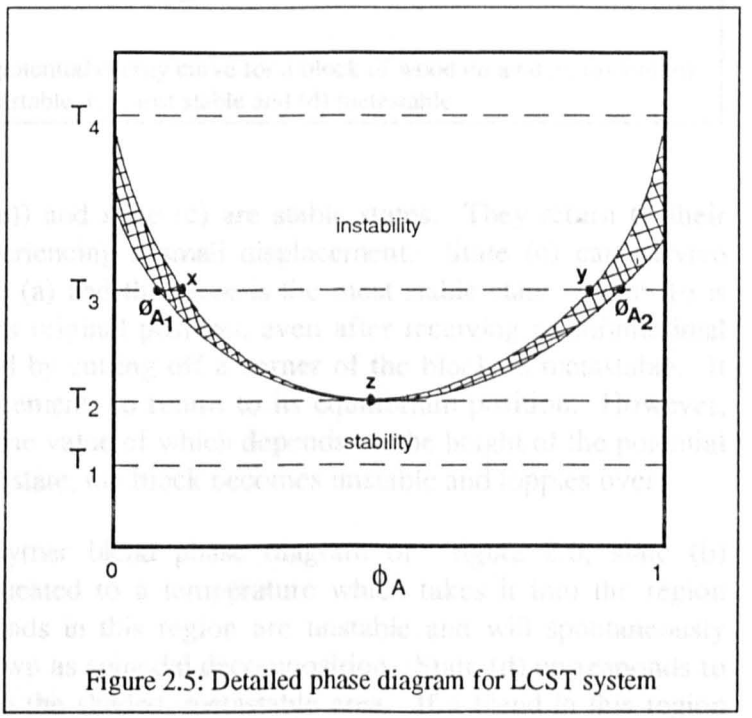

Figure 2.5: Detailed phase diagram for LCST system

2.3.3 Mechanisms of phase separation

Instability and metastability in solutions are complex concepts to grasp, yet both are paramount to understanding phase separation behaviour. To illustrate phase stability, a mechanical analogue can be used. Figure 2.6 shows four possible states of a block of wood on a table. Beneath these, a curve is displayed which represents the potential energy of the block as it passes through the various states. The curve is equivalent to the position of the centre of mass of the block with respect to some fixed reference point, e.g., the table. By examining how each state reacts to small linear displacements, the stability of each state is demonstrated.

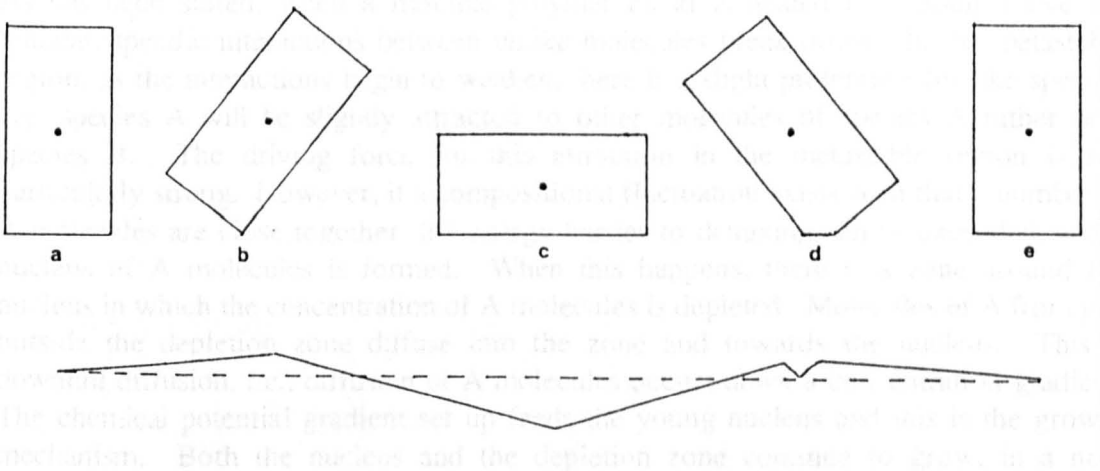

Figure 2.6: States of stability and potential energy curve for a block of wood on a table; (a) and (e) stable; (b) unstable, (c) most stable and (d) metastable

State (a) (equivalent to state (e)) and state (c) are stable states. They return to their equilibrium positions after experiencing a small displacement. State (c) can survive greater displacements than state (a) and therefore is the most stable state. State (b) is unstable. It cannot return to its original position, even after receiving an infinitesimal displacement. State (d), created by cutting off a corner of the block, is metastable. It can withstand very small displacements to return to its equilibrium position. However, beyond a certain displacement, the value of which depends on the height of the potential energy barriers surrounding this state, the block becomes unstable and topples over.

Using this analogy in the polymer blend phase diagram of figure 2.6, state (b) corresponds to a composition heated to a temperature which takes it into the region above the spinodal curve. Blends in this region are unstable and will spontaneously phase separate by a process known as spinodal decomposition. State (d) corresponds to a blend composition heated into the shaded, metastable area. If a blend in this region phase separates, the process is by nucleation and growth.

A summary of the kinetics of phase separation mechanisms (not important in the context of this thesis) can be found in reference 5.

2.3.3.1 Nucleation and growth

When a LCST type binary polymer blend is heated into the region between the binodal and the spinodal, the blend remains single phase but is a metastable "parent" phase. Nucleation is the process by which fragments of a new, more stable phase form within the parent phase. An increase in free energy is required to cause this nucleation and this occurs as a result of small perturbations in composition. This is analogous to the small linear displacements in the mechanical model of figure 2.6. The minimum increase in free energy required for nucleation is defined as the activation energy of the system at a particular temperature/composition point and is equal in value to the energetic barrier to demixing.

As has been stated, when a miscible polymer blend is heated to a point above the binodal, specific interactions between unlike molecules break down. In the metastable region, as the interactions begin to weaken, there is a slight preference for like species, e.g. species A will be slightly attracted to other molecules of species A rather than species B. The driving force for this attraction in the metastable region is not particularly strong. However, if a compositional fluctuation exists such that a number of A molecules are close together, the energy barrier to demixing can be exceeded, and a nucleus of A molecules is formed. When this happens, there is a zone around the nucleus in which the concentration of A molecules is depleted. Molecules of A from just outside the depletion zone diffuse into the zone and towards the nucleus. This is downhill diffusion, *i.e.*, diffusion of A molecules occurs *down* a concentration gradient. The chemical potential gradient set up feeds the young nucleus and this is the growth mechanism. Both the nucleus and the depletion zone continue to grow, in a now spontaneous process which is similar to crystallisation.

Many nuclei are formed in the same period of time, and a dispersed two phase system results as shown in figure 2.7. This phase separation is accompanied by a reduction in free energy. Referring to figure 2.5, if a composition is heated into the metastable shaded region at temperature T_3, nucleation and growth will result in two phases being formed, one of concentration ϕ_{A1}, the other of concentration ϕ_{A2}.

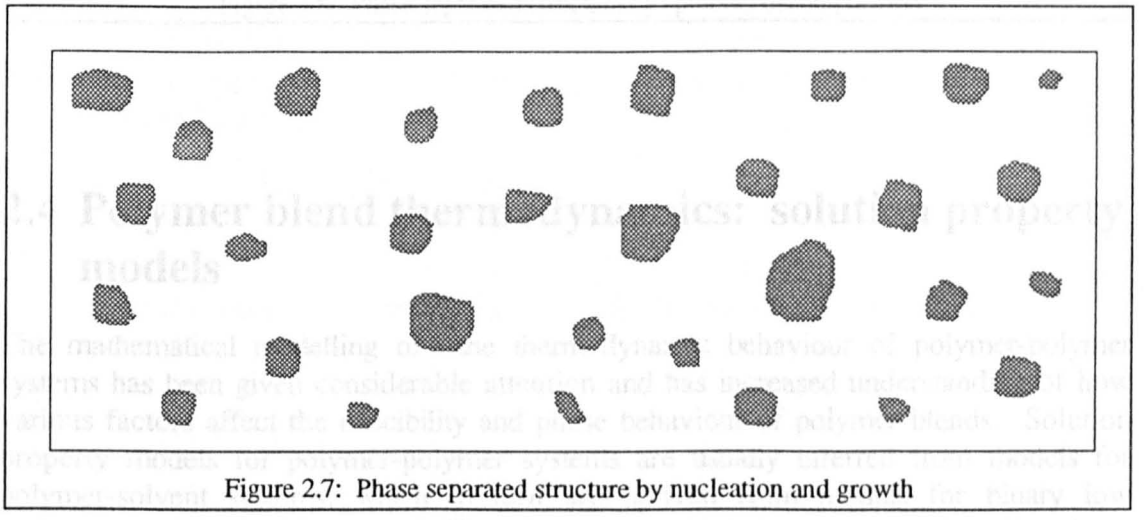

Figure 2.7: Phase separated structure by nucleation and growth

2.3.3.2 Spinodal decomposition

If a LCST type blend is heated to a point above the spinodal, the blend is unstable. Specific interactions between unlike molecules will have broken down completely and there will be a strong preference for like species, *i.e.*, species A will be attracted to other molecules of species A. Very small compositional fluctuations within the unstable parent phase will spontaneously promote rapid and continuous growth of a more stable phase. The driving force for this phase separation is the very strong attractive forces between like molecules, which will allow them to diffuse uphill from the parent phase into the stable phase, *i.e.*, diffusion of molecules is *up* a concentration gradient. The direction of diffusion is the major difference between spinodal decomposition and nucleation and growth. Again referring to figure 2.5, if phase separation occurs at T_3 from a point within the unstable region, the two phases formed will have concentrations ϕ_{A1} and ϕ_{A2} as in the case for nucleation and growth.

Although this mechanism can cause phase separation patterns similar to that due to nucleation and growth shown in figure 2.7, it is more likely that the phase structure formed is of an interconnected nature as seen in figure 2.8.

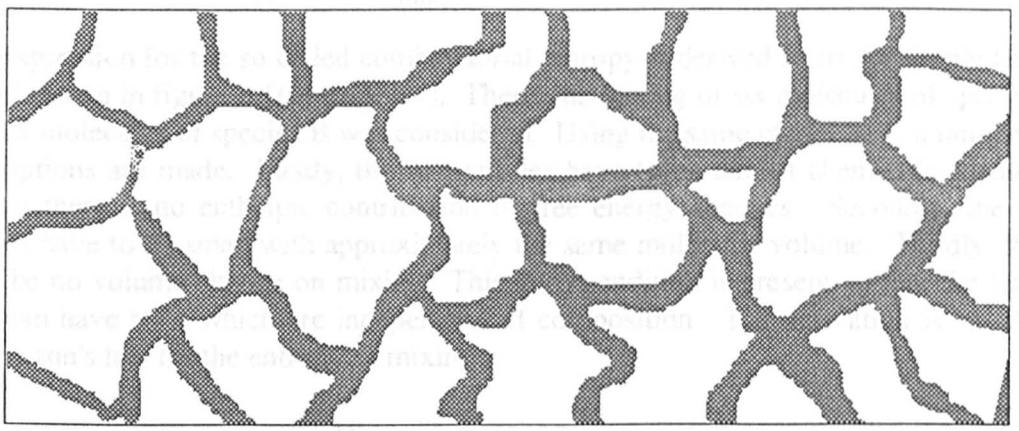

Figure 2.8: Phase separated structure by spinodal decomposition

2.4 Polymer blend thermodynamics: solution property models

The mathematical modelling of the thermodynamic behaviour of polymer-polymer systems has been given considerable attention and has increased understanding of how various factors affect the miscibility and phase behaviour of polymer blends. Solution property models for polymer-polymer systems are usually inferred from models for polymer-solvent systems, which in turn are derived from models for binary low molecular weight liquid mixtures. The whole range of solution concentrations have been considered, *i.e.* dilute solution theories, moderately concentrated solution theories and

in the glassy state and in the melt, and the high degree of molecular entanglement, the only models of interest in this context are concentrated solution theories.

Four concentrated solution theories are presented here; the ideal solution model; the regular solution model; the Flory-Huggins model and the equation of state model. Only the latter two are generally applied to polymer blends, but the former pair help to pave the way. Only brief summaries of each model are presented here. Much more comprehensive derivations are found in the reviews by Carpenter [6] and Olabisi *et al* [5].

2.4.1 Ideal solution theory

Ideal solutions are always completely miscible. This is a very rare situation, but ideal solutions do exist, examples of which are benzene + toluene and cyclohexane + CCl_4. They are formed when two components mixed together yield free energy changes which are due solely to entropy contributions. This of course is an entropy *gain* by each component, due to the extra degrees of freedom each component experiences in solution. With reference to equation 2.1, this definition means that there is no enthalpic contribution to free energy, *i.e.*, $\Delta H_{mix}=0$.

The expression for the so called combinatorial entropy is derived from the simple lattice model shown in figure 2.1(a) (page 17). There, the mixing of six molecules of species A and six molecules of species B was considered. Using the same model here, a number of assumptions are made. Firstly, the two species have to be almost chemically identical, so that there is no enthalpic contribution to free energy changes. Secondly, the two species have to be small with approximately the same molecular volume. Thirdly, there must be no volume change on mixing. This third condition is present so that the lattice sites can have sizes which are independent of composition. The derivation is based on Boltzmann's law for the entropy of mixing

$$\Delta S_{mix} = k \ln \Omega \qquad ...(2.4)$$

where k is the Boltzmann constant and Ω is the number of ways of arranging N_A and N_B molecules on a simple lattice which has $N=N_A+N_B$ sites [9]. By simple combination considerations, this is found to be

$$\Omega = \frac{N!}{N_A! N_B!}. \qquad ...(2.5)$$

Substituting into equation 2.4 and using Stirling's approximation for factorials:

$$\ln x! \approx x \ln x - x \qquad ...(2.6)$$

the expression for combinatorial entropy becomes

$$\Delta S_{mix} = -k(N_A + N_B)(x_A \ln x_A + x_B \ln x_B) \qquad ...(2.7)$$

where x_i is the mole fraction of component i ($=N_i/N$). From equation 1, the Gibbs free energy of mixing becomes

$$\Delta G_{mix} = kT(N_A + N_B)(x_A \ln x_A + x_B \ln x_B). \quad ...(2.8)$$

A characteristic of an ideal solution is that it obeys Raoult's law at all compositions. This law states that the ratio of the vapour pressures of component A in a mixture, p_A, to that of pure component A, p_A^*, is equal to the mole fraction of A in the mixture, *i.e.*

$$p_A = x_A p_A^*. \quad ...(2.9)$$

There are many disadvantages to ideal solution theory: most solutions (and *all* polymer blends) deviate substantially from Raoult's law; phase separation and therefore critical solution temperature behaviour cannot be accounted for; volume changes on mixing are precluded; and the enthalpy of mixing must be zero, a situation which is rare. The theory however does provide a good basis for the regular solution model.

2.4.2 Regular solution theory

First introduced by Hildebrand [10] the concept of the regular solution simplifies the examination of solutions which deviate from ideality, by allowing for non-zero enthalpies of mixing. The entropy of mixing is retained from ideal solution theory, *i.e.*, it is the same as in equation 2.7. The enthalpy of mixing for regular solutions is developed in terms of an exchange energy ω,

$$\omega = \frac{\varepsilon_{AA} + \varepsilon_{BB}}{2} - \varepsilon_{AB} \quad ...(2.10)$$

where ε_{ij} is the contact energy between components i and j. It is assumed that mixing is random, therefore the enthalpy can be given by

$$\Delta H_{mix} = (N_A + N_B) z \omega x_A x_B \quad ...(2.11)$$

where z is the coordination number. This gives a Gibbs free energy of mixing of

$$\Delta G_{mix} = (N_A + N_B)\left(z\omega x_A x_B + kT(x_A \ln x_A + x_B \ln x_B)\right) \quad ...(2.12)$$

This model can predict UCST behaviour and positive deviations from Raoult's law. This is acceptable for many low molecular weight solutions, but for solutions involving polymers, further refinement is required.

2.4.3 Flory-Huggins theory

It was Flory that first observed the irregular solution behaviour in mixtures of polymers and solvents [11]. Large negative deviations from Raoult's law were evident in such mixtures and of course, LCST behaviour. Both Flory and Huggins [12] independently

developed the following necessary refinements to the regular solution theory. Central to the theory is the concept of the lattice shown in figure 2.1(b) (page 17) in which the sites of the lattice represent exchangeable units for entropy calculations and polymer molecules can occupy many adjacent sites. For polymer-solvent systems each lattice site represents the size of a solvent molecule or a solvent sized segment of polymer molecule.

The combinatorial entropy of mixing is now given by

$$\Delta S_{mix}^{comb} = -R(n_A \ln \phi_A + n_B \ln \phi_B) \qquad ...(2.13)$$

where R is the gas constant, n_i is the number of moles and ϕ_i is the volume fraction of component i. Here component A represents solvent and component B is the polymer. The only real difference between this and the ideal solution entropy of equation 2.7 is that volume fractions have replaced mole fractions. Because of the very large number of solvent molecules compared to polymer molecules, the enthalpy of mixing of equation 2.11 approximates to

$$\Delta H_{mix} = z\omega n_A \phi_B \,, \qquad ...(2.14)$$

because ϕ_A tends to 1 and n_B tends to zero. The combinatorial expression for entropy does not take into account specific intermolecular interactions. This is introduced into a complete entropy expression using an entropic interaction term χ_S, so that

$$\Delta S_{mix} = \Delta S_{mix}^{comb} + R\chi_S n_A \phi_B . \qquad ...(2.15)$$

It is usual to think of such interactions as having an enthalpic contribution χ_H as well as an entropic part. From this reasoning is derived the Flory-Huggins interaction parameter χ given by

$$\chi = \frac{z\omega}{RT} - \chi_S \,. \qquad ...(2.16)$$

It is more correct to think of this term as the Flory-Huggins interaction *function*, as it has been shown that χ is dependent on temperature, composition and molecular weight distribution of the polymer.

The final expression for the Gibbs free energy is thus given by

$$\Delta G_{mix} = RT(n_A \ln \phi_A + n_B \ln \phi_B + \chi n_A \phi_B). \qquad ...(2.17)$$

For polymer blends, the same ideas apply and additionally, the molecular weights of both polymers can be brought into the expression for entropy, such that equation 2.17 becomes

$$\Delta G_{mix} = RT\left(\frac{w_A \ln \phi_A}{M_A} + \frac{w_B \ln \phi_B}{M_B} + \chi n_A \phi_B\right) \qquad ...(2.18)$$

where w_i and M_i are the weight fraction and molecular weight of component i. With polymers M_i will be large and therefore entropic contributions to ΔG_{mix} will be small. Enthalpic contributions are however largely independent of molecular weight and free energy is dominated by ΔH_{mix} (which incorporates the χ term). This is confirmation of the ideas first discussed in section 2.3.1.

The Flory-Huggins theory has been of great use since its introduction. One of the most recent uses was demonstrated in a review by Coleman *et al* [13] in which a practical guide to polymer miscibility was presented. As mentioned, χ is a temperature dependent function, and a critical value χ_c can be defined at the critical temperature T_c as being the upper limit for miscibility across the composition range. Coleman's guide proposed that polymer miscibility could be predicted on the basis of a balance between favourable specific interactions (described in terms of the value of χ_c) and unfavourable physical forces (described in terms of the difference between Hildebrand solubility parameters). When looking for new miscible polymer blend systems, the guide suggests minimising χ. If χ is close to zero, the favourable interactions present drive the system towards miscibility. How large the difference in solubility parameters can be depends on the strength of the interactions.

Although its major triumph is in its ability to predict asymmetric coexistence curves, the Flory-Huggins theory does have one major drawback in that it is unable to predict LCST behaviour. Also the theory cannot account for structural differences between components: the lattice theory idealises sites as having similar local structures, for example, the same coordination number z is used for the mixture and for both pure components. This leads to no volume changes on mixing, and enthalpy changes arising only from differences in contact energies. Additionally, because χ has been found empirically to be composition dependent, its physical meaning as a molecular contact parameter is diminished. To address these problems, a new approach is required. This is provided in the equation of state model.

2.4.4 Equation of state theory

The final model presented here, also developed mainly by Flory [14], is based on statistical thermodynamics and corresponding states theory. Although it agrees with experimental data better than the Flory-Huggins theory, its clarity does tend to get lost in mathematical complexity. Only a brief summary is given here.

This model is known as the equation of state theory because the thermodynamical properties of solutions are related to the equation of state characteristics of the pure unmixed components. This allows the influence of, say, the structural differences of the pure components to be taken into account.

The equation of state theory involves a combination of corresponding states theory, particularly the concept of reduced variables which relate physical properties of the pure components to those in solution, and the cell model (as opposed to the lattice model) which introduces statistical thermodynamics. The cell model considers a three dimensional space which is divided into cells of a certain size. Each cell contains a

molecule which can move only within its own cell in the case of solids, to a neighbouring cell in the case of liquids, or through several cells in the case of gases.

To develop this treatment, the case of a pure liquid must first be considered. Statistical thermodynamics deals with *average* behaviour in which thermodynamic properties are described in terms of averages of molecular properties. The concept of a molecular partition function Ω is introduced, which gives an indication of the average number of states which are thermally accessible to a molecule at the temperature of the system. This however does not take into account interaction of particles. To do this a special kind of partition function is required, known as a canonical ensemble, Q.

Rather than determining entropy and enthalpy separately, the Helmholtz free energy A is obtained directly using the canonical ensemble;

$$A = -kT \ln Q. \qquad ...(2.19)$$

Q is a combination of two terms, the partition function Ω for N non-interacting particles and E_0, the mean intermolecular energy for the system. Ω depends on geometrical factors such as the "hard-core" volume or actual value of volume for a molecule within a cell. It is also a function of 3Nc, the number of degrees of freedom which are available to the molecule, where c is a reducing factor (ranging between 0 and 1) which reduces the number of degrees of freedom available, to take into account the bound nature of the molecules.

E_0 depends on the number of contact points per molecule, s, the number of nearest neighbours Nx/2, and the interaction energy per contact, η/υ. The canonical function can then be simplified to

$$Q = [\gamma^{1/3}(\upsilon^{1/3} - \upsilon^{*1/3})]^{3Nxc} \exp\left(\frac{Nxs\eta}{2\upsilon kT}\right) \qquad ...(2.20)$$

where γ is a geometrical term based on molecule length and volume, υ is the volume of the cell, υ^* is the hard-core volume of the molecule, and x is the number of cell sized segments in the molecular chain.

Reduced variables $\overline{p} = p/p^*$, $\overline{\upsilon} = \upsilon/\upsilon^*$ and $\overline{T} = T/T^*$ are then used and the equation of state for a pure liquid is given by

$$\frac{\overline{p}\,\overline{\upsilon}}{\overline{T}} = \frac{\overline{\upsilon}^{1/3}}{\left(\overline{\upsilon}^{1/3} - 1\right)} - \left(\frac{1}{\overline{\upsilon}\overline{T}}\right) \qquad ...(2.21)$$

which can then be inserted into the canonical ensemble.

Binary mixtures are now considered. Each term in the canonical ensemble is now made up as contributions from both components e.g. $N=N_A+N_B$ etc

$$Q = \Omega_c\left(\tilde{v}^{1/3} - 1\right)^{3Nc\bar{r}} \exp\left(-\frac{E_0}{kT}\right) \qquad ...(2.22)$$

where Ω_c is the number of distinguishable configurational arrangements for molecules in the mixture and $\bar{x} = (x_A N_A + x_B N_B)/N$.

For mixtures, E_0 considers only nearest neighbour interactions and an exchange energy parameter η (similar to ω in the Flory-Huggins theory) is defined along with a site fraction θ which is the probability that a cell site will contain a certain species. The E_0 expression is now

$$E_0 = \left(-\frac{\bar{x}Ns}{2v}\right)(\theta_A\eta_{AA} + \theta_B\eta_{BB} - \theta_A\theta_B\eta). \qquad ...(2.23)$$

From the canonical ensemble and the Helmholtz expression, equations are derived for ΔH_{mix}, ΔS_{mix} and ΔG_{mix}. The enthalpy of mixing is based on E_0 calculations and is given by

$$\Delta H_{mix} = \bar{x}N\upsilon^*\left[\phi_A p_A^*\left(\frac{1}{\tilde{v}_A} - \frac{1}{\tilde{v}}\right) + \phi_B p_B^*\left(\frac{1}{\tilde{v}_B} - \frac{1}{\tilde{v}}\right) + \left(\frac{\phi_A\theta_B}{\tilde{v}}\right)X_{AB}\right]. \qquad ...(2.24)$$

Although the idea of a Flory-Huggins type single interaction parameter is abandoned in this model, the introduction of X_{AB} into equation 2.24 makes ΔH_{mix} easier to handle. It is a contact interaction parameter defined to take into account s, η and v*.

The entropy expression is

$$\Delta S_{mix} = \Delta S_c + \Delta S_R \qquad ...(2.25)$$

where ΔS_c is the combinatorial entropy of the Flory-Huggins theory and ΔS_R is known as the residual entropy. It represents the influence exerted on the properties of the mixture by the distinctive structural characteristics of the pure components and is arrived at through the characteristic parameters thus,

$$\Delta S_R = -3\left(\frac{N_A p_A^* V_A^* \tilde{T}_A}{T}\right)\ln\left[\frac{\tilde{v}_A^{1/3} - 1}{\tilde{v}^{1/3} - 1}\right] - 3\left(\frac{N_B p_B^* V_B^* \tilde{T}_B}{T}\right)\ln\left[\frac{\tilde{v}_B^{1/3} - 1}{\tilde{v}^{1/3} - 1}\right] \qquad ...(2.26)$$

and the final expression for ΔG_{mix} is obtained by substituting equations 2.24, 2.25 and 2.26 into equation 2.1. An expression for the volume change on mixing can also be obtained:

$$\Delta V_{mix} = \left(\frac{V_0}{\tilde{v}_0}\right)\left\{\tilde{v} - (\phi_A\tilde{v}_A + \phi_B\tilde{v}_B)\right\} \qquad ...(2.27)$$

where V_0 is the unmixed volume and $\overline{v}_0 = \phi_1 \overline{v}_1 + \phi_2 \overline{v}_2$.

There is little doubt about the academic success of this theory. It is the most accurate concentrated solution model available but many minor adjustments need to be made to make theory fit to specific systems.

CHAPTER THREE - Surface Studies of Polymers and Polymer Blends

3.1 Introduction

3.1.1 The need for surface analysis

There are many ways in which surface properties of materials manifest themselves, and understanding and manipulation of these properties can make significant improvements to our everyday lives.

The chemical structure of a material's surface can differ markedly from the bulk. There are several reasons for this, examples of which are migration of low surface energy impurities and adsorption of environmental species. The most important reason however is this: in a pure material, the molecules at the surface will have less nearest neighbours as those in the bulk. There will not therefore be as much intermolecular activity at the surface which can lead to reorganisation and reorientation of molecules.

It is the surface structure of a material which has greatest influence on its surface related properties. Therefore an understanding of surface properties depends on a detailed knowledge of the chemical structure of the surface. In the context of this thesis, the surface of a material is defined as being no more than the outermost 10nm of the material. Techniques which probe either chemical or physical features within the top 10nm are considered as surface analytical techniques.

There are many techniques used in a material's surface analysis. A detailed summary of these techniques can be found in Riviere's book [15]. For polymers and polymer blends, a most powerful combination of techniques is that of X-ray photoelectron spectroscopy (XPS) and static secondary ion mass spectroscopy (SSIMS). In this chapter the two techniques are described in detail. This is followed by a brief summary of some of the more important studies on polymers and polymer blends using these techniques. Finally, a description of surface studies on the blend system of PVC and PMMA will be given; this blend was chosen for analysis in the present study.

3.2 X-ray Photoelectron spectroscopy (XPS)

3.2.1 Historical background

XPS is a photon beam technique which has its origins in the investigation of the photoelectric effect during the early part of this century. Innes [16], Rutherford [17] and Auger [18] were all involved in spectroscopy experiments in which the exciting source was X-rays. The most important developments in the technique however were made from the 1940's onwards by Siegbahn and his group at the University of Uppsala. The first well defined XP spectrum was obtained in the mid 1950's and for the next fifteen years, the whole field of XPS was developed here [19]. During the late 60's and early 70's, commercial instruments started to appear and since this time, the use of XPS in industry and academia has grown rapidly. Now it is one of the most popular laboratory techniques used for surface analysis.

3.2.2 General principle

In XPS, soft X-rays incident on a sample cause photoemission of core electrons from atoms from within that sample. This effect is not restricted to the surface layers, however, only photoelectrons emitted from atoms near the surface can avoid collision and escape from the surface. The kinetic energies of the photoelectrons from the surface atoms are analysed and a spectrum of binding energies can be produced. Although the spectrometer measures the kinetic energy E_K of the photoelectron, this is not an intrinsic material property as it is dependent on the X-ray energy $h\nu$. The parent element, the atomic energy level and the chemical state of the element in the surface are identified by the binding energy E_B of the photoelectron which is arrived at through equation 3.1:

$$E_B = h\nu - E_K - \phi \qquad ...(3.1)$$

where ϕ is the work function of the spectrometer. Figure 3.1 shows a schematic of the photoionisation process. The X-ray photon with energy $h\nu$ causes photoemission of a 1s orbital electron with energy E_K. All core electrons are available for photoionisation, with two exceptions: (i) core electrons which take part in bonding, and (ii) core electrons whose binding energy is greater than that of the incoming photon. Usually, only the most intense core levels are detected in an

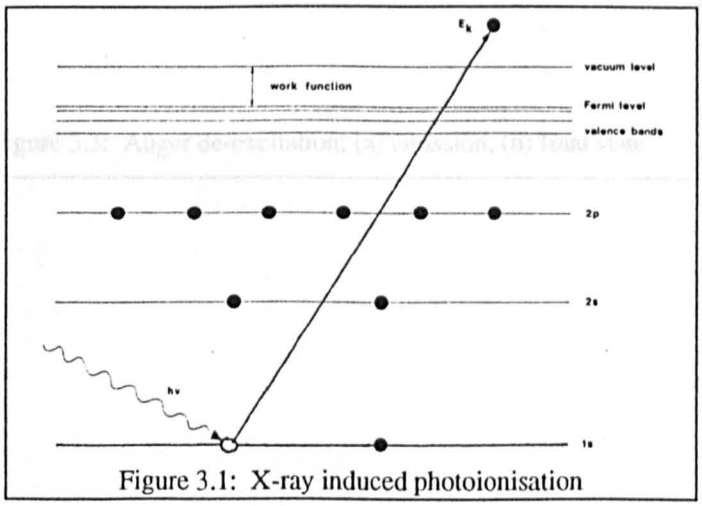

Figure 3.1: X-ray induced photoionisation

XP spectrum; photoelectron peaks resulting from core levels with low photoionisation cross sections will usually be lost in the background.

Once photoionisation takes place, relaxation of the atom must occur. This can happen by either X-ray fluorescence or Auger electron emission. X-ray fluorescence is shown in figure 3.2. The emission process shown in figure 3.2(a) occurs as a result of the "hole" appearing in the 1s core level. An electron from a higher energy level fills the hole and the excess energy is lost in the form of X-ray fluorescent emission. This leaves a singly ionised state as in figure 3.2(b). Alternatively, rather than X-ray fluorescence occurring, the excess energy can be transferred to a higher energy level as in figure 3.3(a) which results in the emission of a second electron. This is an Auger electron and results in a doubly ionised state as shown in figure 3.3(b). The Auger process is the basis of a similar surface technique, Auger electron spectroscopy (AES), in which primary electrons are used as the excitation source. This technique is not suitable for insulating samples such as polymers and polymer blends and therefore need not be described here. Nevertheless the Auger process is of some importance in XPS as features due to Auger electron emission appear on most XP spectra.

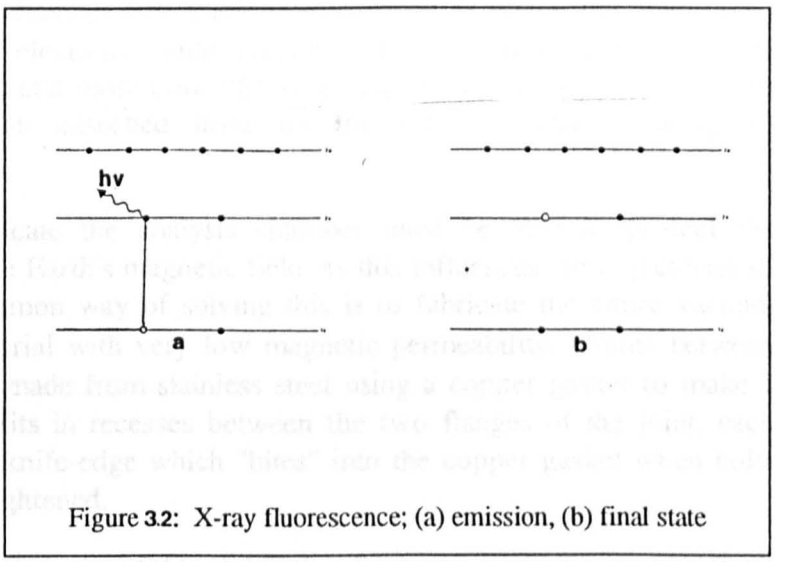

Figure 3.2: X-ray fluorescence; (a) emission, (b) final state

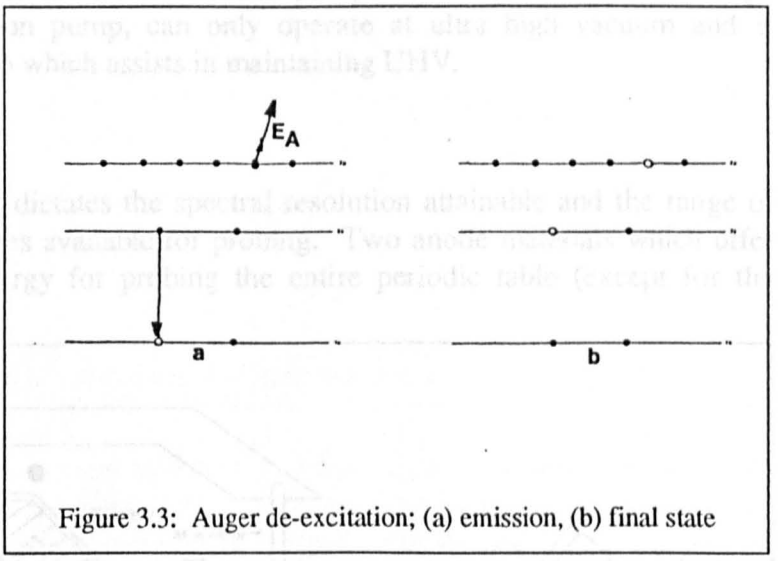

Figure 3.3: Auger de-excitation; (a) emission, (b) final state

3.2.3 Instrumentation and sample handling

3.2.3.1 Vacuum requirements

XPS experiments must be carried out at pressures approaching 10^{-10}mb. There are two reasons for this ultra high vacuum (UHV) requirement. The first is that if gas molecules are present in the analysis chamber (the UHV compartment in which the experiment takes place), photoemitted electrons could collide with these, leading to very low intensity spectra. Secondly, and more critically, when gases are present in the analysis chamber they can form an adsorbed layer on the sample surface, leading to misinterpretation of results.

The material used to fabricate the analysis chamber must be able to protect the experimental region from the Earth's magnetic field, as this influences the trajectories of the photoelectrons. A common way of solving this is to fabricate the entire vacuum vessel from μ-metal, a material with very low magnetic permeability. Joints between vacuum vessels are usually made from stainless steel using a copper gasket to make a vacuum seal. The gasket sits in recesses between the two flanges of the joint, each recess containing a tapered knife-edge which "bites" into the copper gasket when bolts connecting the flanges are tightened.

The method of obtaining UHV is threefold. A low level vacuum pump (e.g. a two stage rotary pump) is used to pump the majority of gases from the system. At between 10^{-2} and 10^{-3}mb, a second pump takes over. This is the main UHV pump and is usually a diffusion pump charged with polyphenylether oil and fitted with a liquid nitrogen cold trap. Other UHV pumps used are turbomolecular pumps and ion pumps. A third stage pump, a titanium sublimation pump, can only operate at ultra high vacuum and is considered an auxiliary pump which assists in maintaining UHV.

3.2.3.2 Sources

The choice of X-ray source dictates the spectral resolution attainable and the range of core electron binding energies available for probing. Two anode materials which offer high enough X-ray line energy for probing the entire periodic table (except for the

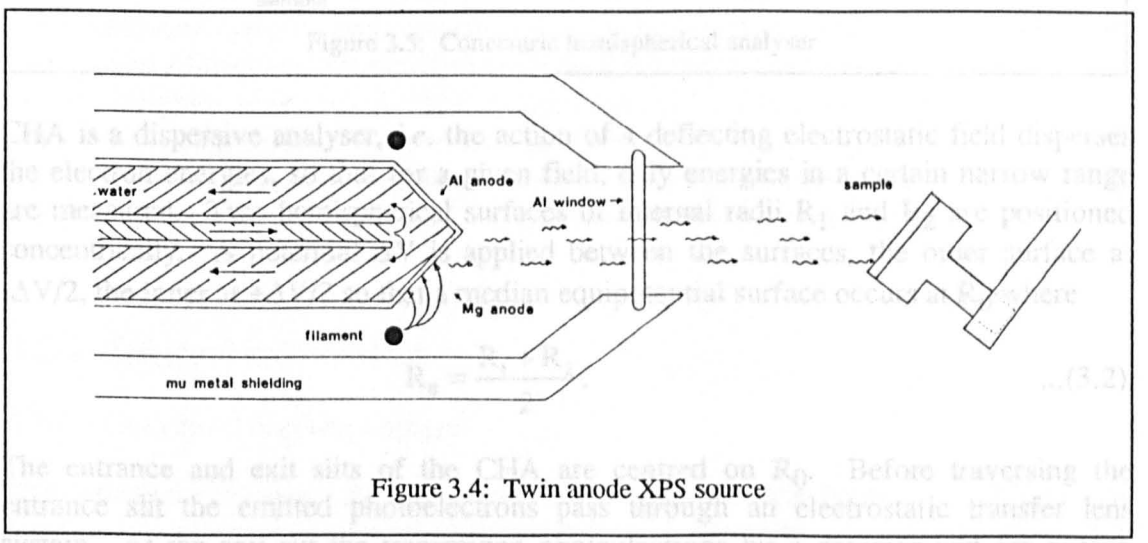

Figure 3.4: Twin anode XPS source

lightest elements) and with reasonable resolution, are magnesium and aluminium. For this reason the most popular type of X-ray source used in XPS is a twin anode arrangement in which Al and Mg are deposited on opposite faces of a water cooled copper mount, as shown in figure 3.4. A dedicated filament is positioned near each anode face and depending on which anode is selected, electrons from the filament are accelerated through a maximum of 15kV towards the anode, creating either Mg$K\alpha$ X-rays of energy 1253.6eV with a linewidth of 0.7eV, or Al$K\alpha$ X-rays of energy 1486.6eV and linewidth 0.85eV.

On more advanced XPS sources a monochromator is used which reduces the X-ray line width and rids the X-ray emission spectrum of Brehmsstrahlung radiation. Such radiation contributes to high background levels in the low binding energy region of the XP spectrum.

3.2.3.3 Analysers

The most popular kind of photoelectron energy analyser is the CHA, the concentric hemispherical analyser. A schematic of such an analyser is shown in figure 3.5. The

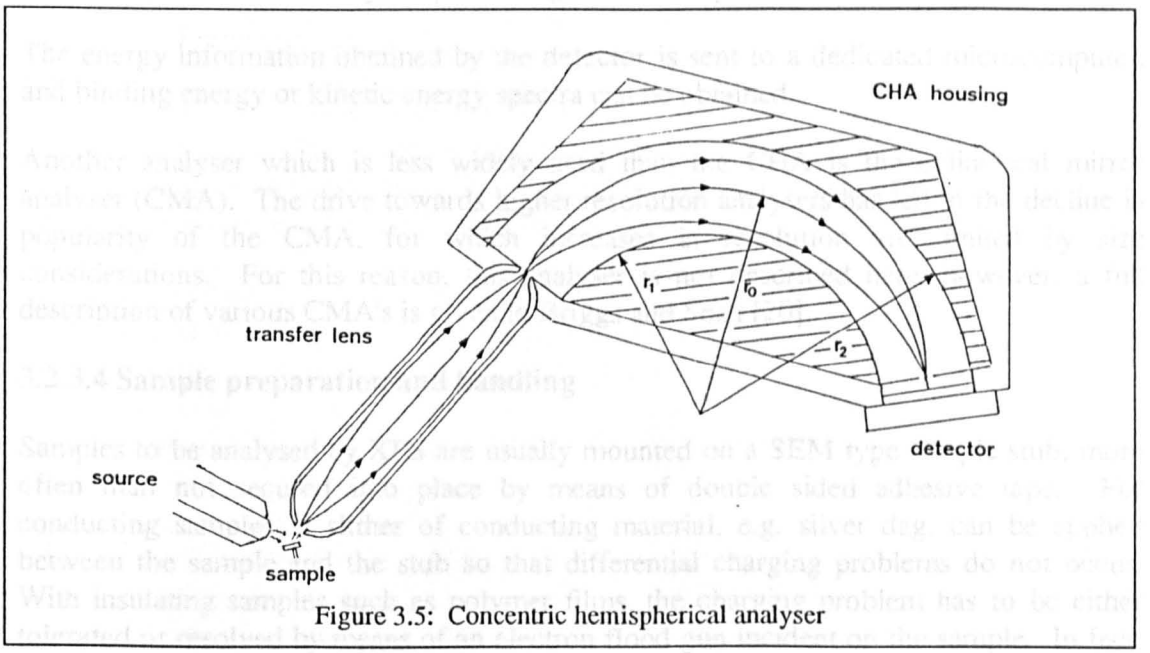

Figure 3.5: Concentric hemispherical analyser

CHA is a dispersive analyser, *i.e.* the action of a deflecting electrostatic field disperses the electron energies, so that for a given field, only energies in a certain narrow range are measured. Two hemispherical surfaces of internal radii R_1 and R_2 are positioned concentrically. A potential ΔV is applied between the surfaces, the outer surface at $-\Delta V/2$, the inner at $+\Delta V/2$ so that a median equipotential surface occurs at R_0 where

$$R_0 = \frac{R_1 + R_2}{2}. \qquad ...(3.2)$$

The entrance and exit slits of the CHA are centred on R_0. Before traversing the entrance slit the emitted photoelectrons pass through an electrostatic transfer lens system. At the exit slit the transmitted photoelectrons hit a detector and are energy

analysed. If an electron has energy E and travels in an orbit through the analyser with radius R_0, then

$$E = \frac{e\Delta V}{\left[R_2/R_1 - R_1/R_2\right]} \qquad ...(3.3)$$

where e is the electron charge. The analyser can be operated in constant analyser energy mode which means that during acquisition ΔV is fixed at a value set by the user. The "pass energy" is defined as the product of the analyser constant (unique to each instrument) and ΔV. When an XPS scan is run in this mode the lens system before the entrance slit is automatically adjusted to allow first of all electrons with the "start" kinetic energy to be transmitted through the CHA, then gradually the voltage across the transfer lens is decreased so that electrons of a lower energy will be transmitted. Eventually, the lens will only allow electrons with the "finish" kinetic energy to be transmitted. The start and finish kinetic energies are set by the user. The energy range ΔE of electrons transmitted at a particular time during acquisition (*i.e.* the absolute resolution) is determined by the pass energy, also set by the user.

The energy information obtained by the detector is sent to a dedicated microcomputer, and binding energy or kinetic energy spectra can be obtained.

Another analyser which is less widely used than the CHA is the cylindrical mirror analyser (CMA). The drive towards higher resolution analysers has led to the decline in popularity of the CMA, for which increases in resolution are limited by size considerations. For this reason, this analyser is not described here, however, a full description of various CMA's is given in Briggs and Seah [20].

3.2.3.4 Sample preparation and handling

Samples to be analysed by XPS are usually mounted on a SEM type sample stub, more often than not secured into place by means of double sided adhesive tape. For conducting samples, a slither of conducting material, e.g. silver dag, can be applied between the sample and the stub so that differential charging problems do not occur. With insulating samples such as polymer films, the charging problem has to be either tolerated or resolved by means of an electron flood gun incident on the sample. In fact, sample charging with non-monochromated sources is a relatively small problem, the main effect being the shift of core level peak envelopes to the high binding energy side by 1 or 2eV. It does not affect the intensity of the peak envelope or the raw peak area, nor does it affect chemical shifts of components within the peak envelope.

3.2.4 Spectral information

3.2.4.1 Core level binding energies

The binding energy spectrum produced is of the form shown in figure 3.6, in which core level peaks are superimposed on a background which gradually increases to high binding

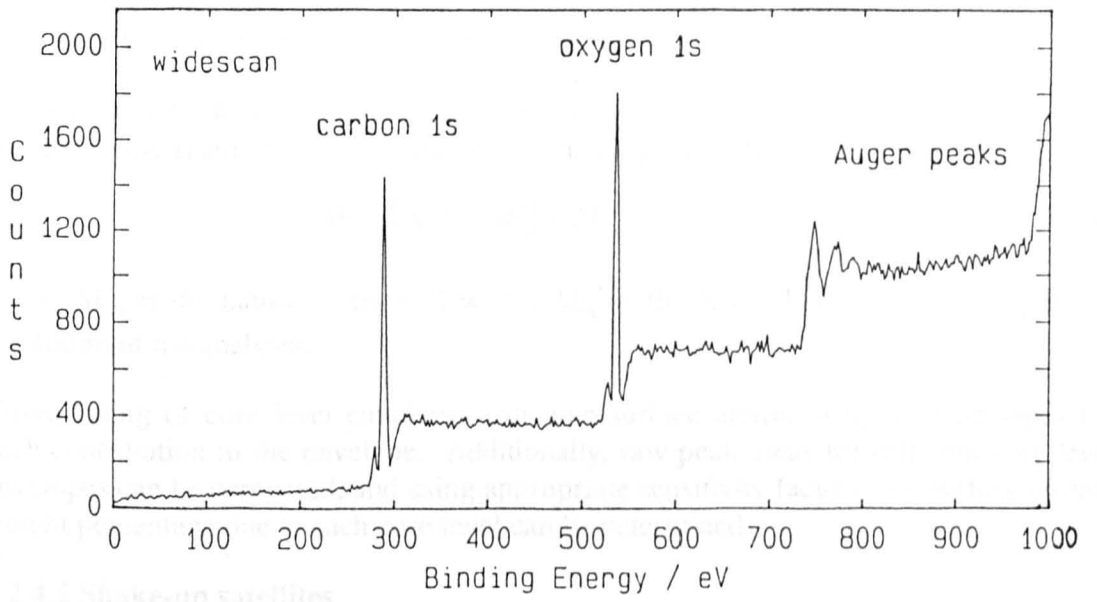

Figure 3.6: XPS widescan spectrum of an oxygen containing organic polymer

energy. A core level peak is always followed on the high binding energy side by an increase in intensity. This is due to photoelectrons from the particular core level which have been inelastically scattered. Such photoelectrons are emitted with a lower kinetic energy and are therefore detected at higher binding energy.

The spectrum shown in figure 3.6 is a widescan or survey spectrum. This gives a general idea of which elements are contained in the sample surface. For quantitative analysis, narrow scan spectra are acquired for the core levels of interest. Figure 3.7 shows the narrow scan spectrum for a thick film sample of PMMA, acquired for the present study. It is seen that the C1s envelope contains a number of contributions. The most intense contribution is due to carbon bound to itself and/or hydrogen only. This gives a binding energy of 285eV, but as this is a thick insulating film, the whole C1s spectrum has been shifted to a slightly higher binding energy, as discussed in the previous section. Chemical

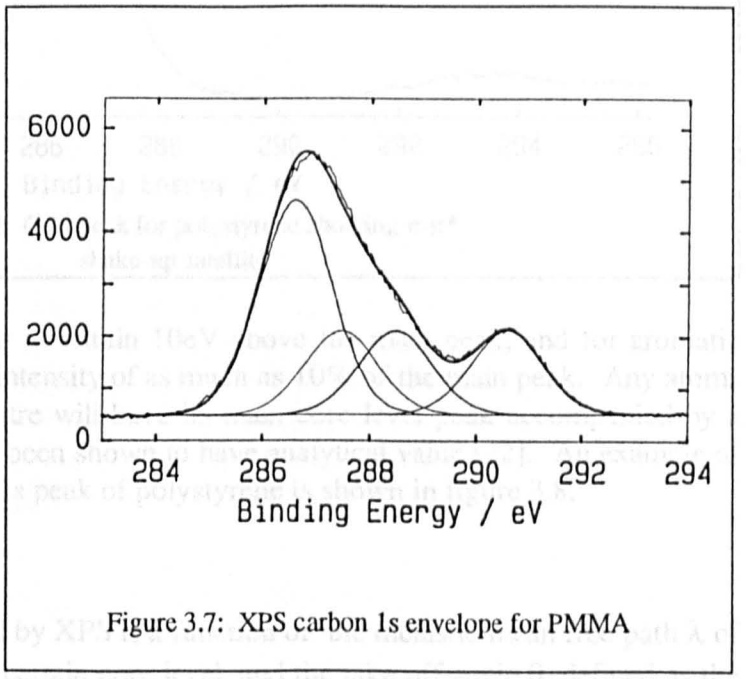

Figure 3.7: XPS carbon 1s envelope for PMMA

shifts within the envelope are induced by the chemical state of the element. For example, for C1s, halogens will induce shifts from 285eV to the high binding energy side (the value of shift depending on the particular halogen) and oxygen will induce shifts from 285eV by between 1.5 to 2eV per C-O bond.

The width of peaks in XP spectra (*i.e.* the width of each contribution to a core level envelope) is defined by the full width at half maximum (FWHM), ΔE, given by [21]

$$\Delta E = \left(\Delta E_n^2 + \Delta E_p^2 + \Delta E_a^2\right)^{1/2} \qquad ...(3.4)$$

where ΔE_n is the natural core level width, ΔE_p is the X-ray line width and ΔE_a is the resolution of the analyser.

Curve fitting of core level envelopes can give surface atomic weight percentages for each contribution to the envelope. Additionally, raw peak areas for different core level envelopes can be compared, and using appropriate sensitivity factors, the surface atomic weight percentage due to each core level can be determined.

3.2.4.2 Shake-up satellites

For analysis of samples which contain unsaturated centres, the detection of photoelectrons arising from the π-π^* transition is common and expected. These so

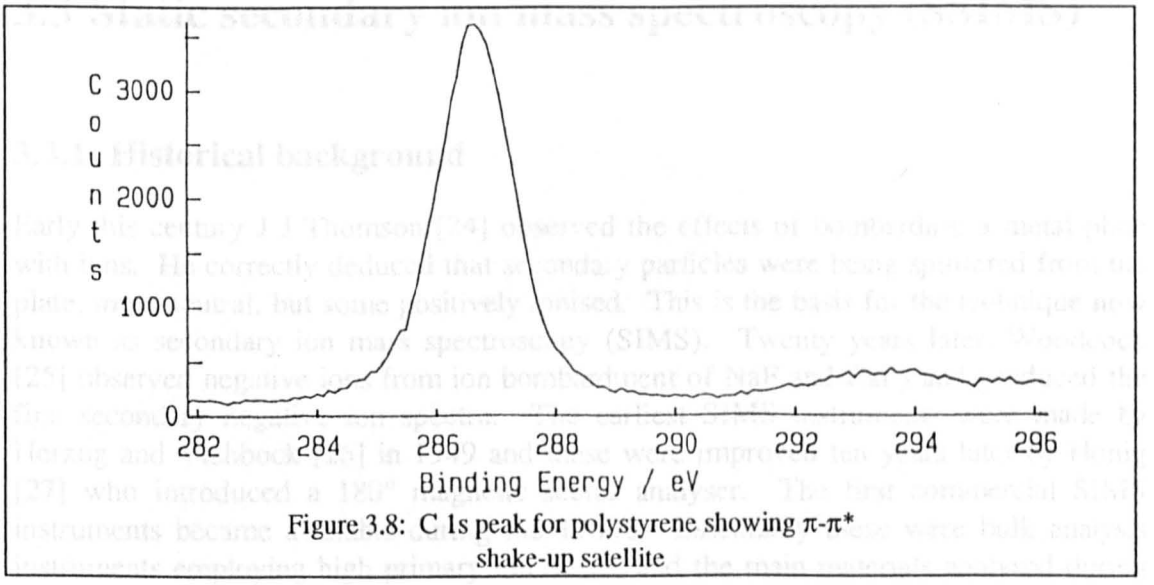

Figure 3.8: C 1s peak for polystyrene showing π-π^* shake-up satellite

called shake-up satellites occur at within 10eV above the main peak, and for aromatic polymer samples, can have an intensity of as much as 10% of the main peak. Any atoms attached to an unsaturated centre will have its main core level peak accompanied by a shake-up satellite. These have been shown to have analytical value [22]. An example of the shake-up satellite for the C1s peak of polystyrene is shown in figure 3.8.

3.2.4.3 Information depth

The depth of features identified by XPS is a function of the inelastic mean free path λ of photoelectrons emitted from a certain core level, and the take off angle θ, defined as the

angle between the plane of the sample surface and the axis of the analyser transfer lens (see figure 3.9). For Mg$K\alpha$ radiation, λ has been found to be 1.2nm for C1s core electrons [23]. It is observed that *ca.* 95% of the signal intensity derives from a distance 3λ within the solid. When the take off angle is taken into account, the information depth d is given by

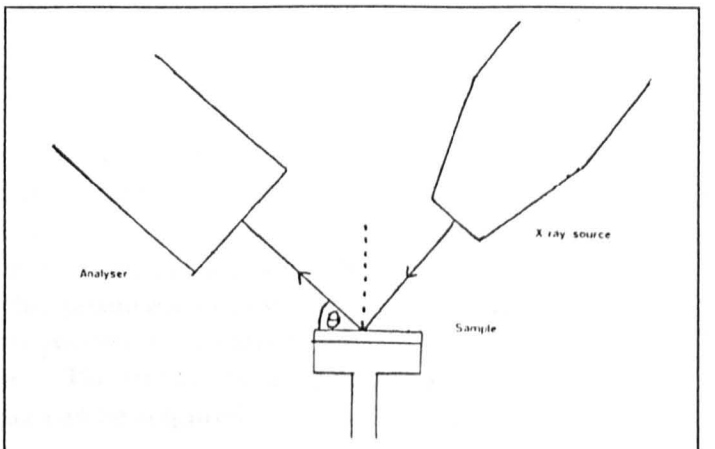

Figure 3.9: Definition of the XPS take-off angle

$$d = 3\lambda \sin \theta. \qquad ...(3.5)$$

By varying the take off angle, depth profiling studies can be made.

3.3 Static secondary ion mass spectroscopy (SSIMS)

3.3.1 Historical background

Early this century J J Thomson [24] observed the effects of bombarding a metal plate with ions. He correctly deduced that secondary particles were being sputtered from the plate, most neutral, but some positively ionised. This is the basis for the technique now known as secondary ion mass spectroscopy (SIMS). Twenty years later, Woodcock [25] observed negative ions from ion bombardment of NaF and CaF_2 and produced the first secondary negative ion spectra. The earliest SIMS instruments were made by Herzog and Viehbock [26] in 1949 and these were improved ten years later by Honig [27] who introduced a 180° magnetic sector analyser. The first commercial SIMS instruments became available during the 1960's. Essentially these were bulk analysis instruments employing high primary ion doses, and the main materials analysed during this time were semiconductors and inorganic thin films. In 1969 Benninghoven [28] introduced the concept of "static" SIMS in which very low primary ion doses were utilised to obtain SIMS experiments in which very little damage was done to the sample. This established SIMS as a highly surface sensitive technique and static SIMS (SSIMS) has now become accepted as an analytical technique for probing the outermost surface structures of metals, ceramics, glasses and polymers.

3.3.2 General principle

3.3.2.1 The SIMS experiment

SIMS analysis consists of three elements; the source, the sample and the mass analyser. Primary ions are created, accelerated through a large potential difference and focused onto the sample. The primary ion bombardment causes a complex collisional sputtering process to occur. Fragments sputtered from the surface will be mainly neutral, but a small proportion, *ca.* 1%, will be either positively or negatively ionised. By applying an appropriate bias to the sample, either positive or negative ions can be repelled from the sample area and towards the analyser. The fragments are then mass analysed and both positive and negative ion mass spectra can be acquired.

3.3.2.2 Sputtering and ionisation

The sputtering/ionisation process is highly complex and is the subject of much debate in the literature. It is generally accepted however that the sputtering process is explained by the collision cascade model in which a primary particle penetrating the surface of the sample will transfer its kinetic energy via a series of billiard ball type collisions with subsurface atoms (see figure 3.10). As a result, atoms and molecules in the surface region may acquire momentum in the surface direction, and if this is strong enough to overcome the surface binding energy, the atom or molecule will be sputtered. Of the many ionisation models that have been proposed, there is no single accepted universal theory. All models accept that electron transfer takes place between the fragment and the surface. A review of sputtering/ionisation models is given by Hearn [29].

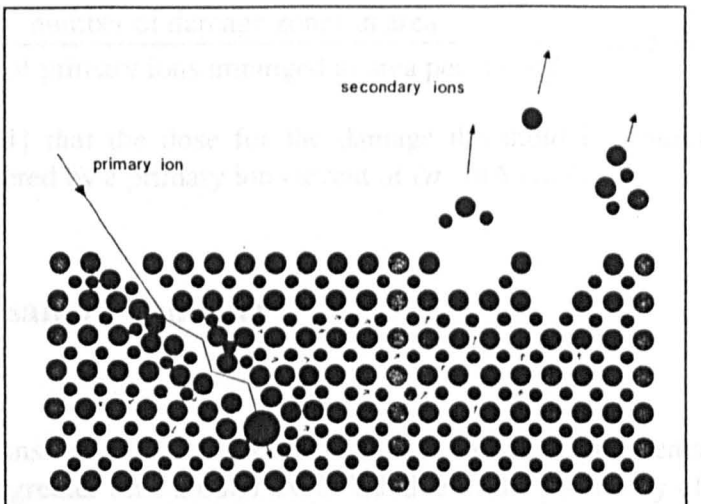

Figure 3.10: Collision cascade sputtering model

3.3.2.3 The basic equation of SIMS

The secondary ion current of a species M undergoing primary ion bombardment is given by [30]

$$I_S^M = I_P \, S \, R^+ \, \theta_M \, \eta. \qquad ...(3.6)$$

Here, I_P is the current density of the primary ion beam. S is the sputter yield of species M which is dependent on the energy and the charge state of the primary particles and on the type of chemical bonds present in the surface of M. R^+ is the ionisation probability for positive secondary ions (R^- for negative ions), dependent on the ionisation potential

and the electron affinity of the particle, as well as the electronic state of the surface. θ_M is the fractional coverage of M and η is the transmission of the analysis system, determined by the ion collection optics of the mass spectrometer system used.

3.3.2.4 The static SIMS condition

Static SIMS is the mode of SIMS operation in which the density of the primary ion beam is of a sufficiently low value so as not to cause excessive damage to the sample surface. The perturbation region caused by a single impact is called the damage cross section σ. If A is the total area of bombardment and $\Sigma\sigma_i$ is the total number of damaged areas, the probability of a primary ion impacting on a previously damaged site is

$$p = \frac{\Sigma\sigma_i}{A}. \qquad ...(3.7)$$

This assumes that σ is very much less than A. From surface lifetime considerations in which

$$\text{Lifetime of surface} = \frac{\text{number of damage zones in area}}{\text{number of primary ions impinged in area per second}} \qquad ...(3.8)$$

it has been shown by Magee [31] that the dose for the damage threshold is around $5\text{x}10^{12}$ ions cm^{-2} and this is delivered by a primary ion current of *ca.* 1nA cm^{-2}.

3.3.3 Instrumentation and sample handling

3.3.3.1 Vacuum requirements

These are the same as for XPS instrumentation (section 3.2.3.1). SIMS experiments cannot be performed at pressures greater than around $2\text{x}10^{-9}$mb due to the possibility of source contamination which can cause ion gun instability.

3.3.3.2 Sources

There are two types of primary ion source which are used in static SIMS. The first is a noble gas source such as xenon or argon in which the primary molecules are ionised by electron bombardment prior to being extracted and accelerated to energies usually no greater than 5keV. The beam is used either in a focused mode (spot diameter *ca.* 10μm) and raster scanned across the sample, or defocused (spot diameter >5mm) and used in a stationary mode. The second type, the liquid metal ion source, has become more common in recent years and is used in microanalysis applications where high lateral resolution is required. A most common source metal is gallium, although indium, caesium and gold have been used. In the case of a gallium metal ion source, a reservoir of gallium is heated to the liquid state which wets and flows over a fine needle. A high positive electrical field is established between the needle tip and an extractor, as shown in figure 3.11, resulting in an intense emission of $^{69}Ga^+$ and $^{71}Ga^+$ ions. A Wein filter is employed to separate the isotopes so that only $^{69}Ga^+$ constitutes the beam. Ion optics can focus this high brightness beam down to a spot as little as 50nm in diameter. For

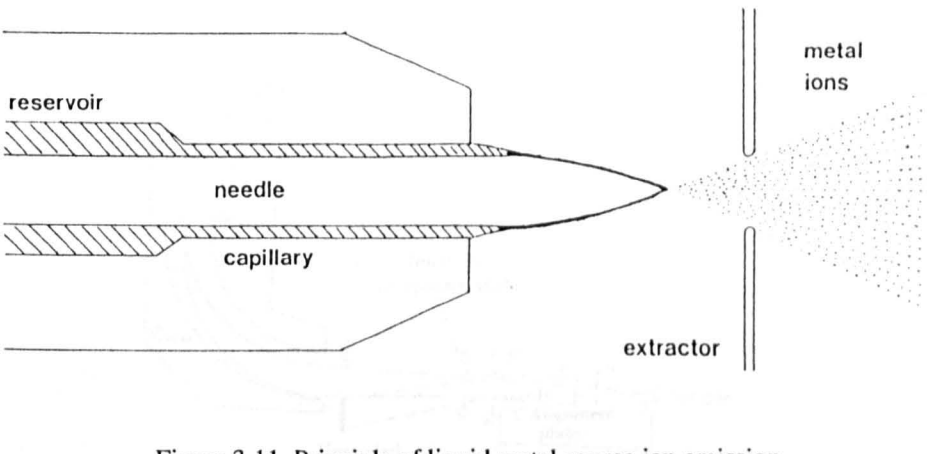

Figure 3.11 Principle of liquid metal source ion emission

static SIMS operation, liquid metal ion probes are usually pulsed, producing packets of ions which are typically 5-50ns in length.

3.3.3.3 Analyser

Three types of mass analyser are commonly used in SIMS: quadrupole, magnetic sector and time of flight. Quadrupole mass analysers (or "quads") consist of four parallel cylindrical rods. A DC voltage and a RF voltage are applied across opposite pairs of poles. Secondary ions are ejected from the sample and into the quad. Only ions in a certain narrow mass range will be transmitted by the quad to a detection system at the base of the poles. This mass range is determined by the ratio of the DC and RF voltages. All other ions hit either the poles or the quad housing. The upper mass analysis limit for quads are a few hundred atomic mass units, with typical ion transmissions of between 0.01 and 1%.

Magnetic sector analysers offer increased transmission (*ca.* 1%) and a much higher mass limit (>10,000 amu) but since these analysers cannot be used in the static regime, they will not be further described here.

To provide high mass sensitivity with minimal surface damage, a time of flight mass analyser is used. A SIMS system utilising such a mass analyser is called a ToFSIMS (time of flight SIMS) instrument. There are two types of ToF design, the Poschenrieder and the reflectron. The Poschenrieder [32] energy compensated mass spectrometer, shown in figure 3.12, uses a toroidal electrostatic field which can focus a pulsed, angularly dispersed beam of ions in both energy and time. The toroidal field is preceded and followed by straight drift tubes. Secondary ions are extracted from the sample by applying a high voltage to the sample holder (positive for positive ion spectra, negative for negative ion spectra) and the ions disperse in time and energy along the first drift tube. In the toroidal electric field, ions of different energies will take trajectories of different lengths. The slower speed of the lower energy ions will be exactly compensated by the shorter flight path taken. In the second drift tube at the end of which is a detector, the ions are once again dispersed in time and energy. The toroidal electric field focuses the ions onto a single point at the detector, which is connected to a

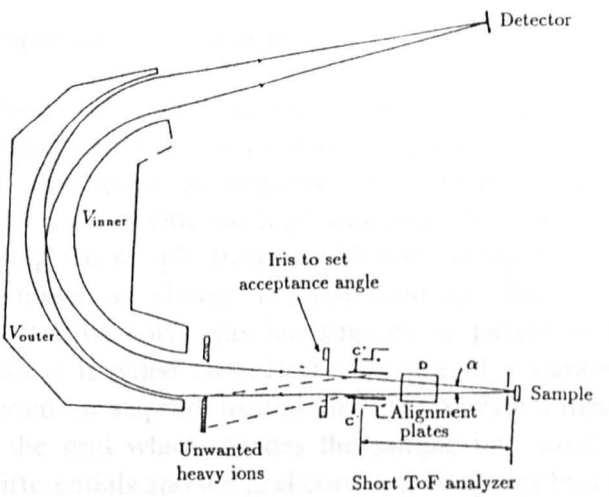

Figure 3.12: Poschenrieder time of flight mass spectrometer

data system. This geometry means that the mass of the ions only depend on the time of the flight taken around the analyser and is independent of the ion's energy.

The reflectron ToF mass spectrometer [33] works on the same principle as the Poschenrieder with one exception: instead of a toroidal electrostatic field, the ions once ejected from the sample, travel through an increasingly decelerating field which directs the ions towards a slightly offset drift tube at the end of which is the detection system. This is shown schematically in figure 3.13.

The great advantages of ToF analysers are in their transmission, up to 30% of all secondary ions, and in their almost simultaneous detection of all ions, regardless of mass. Theoretically such analysers have no upper mass limit, but practically, detection up to around 10,000 amu is expected. ToF analysers have a low secondary ion energy

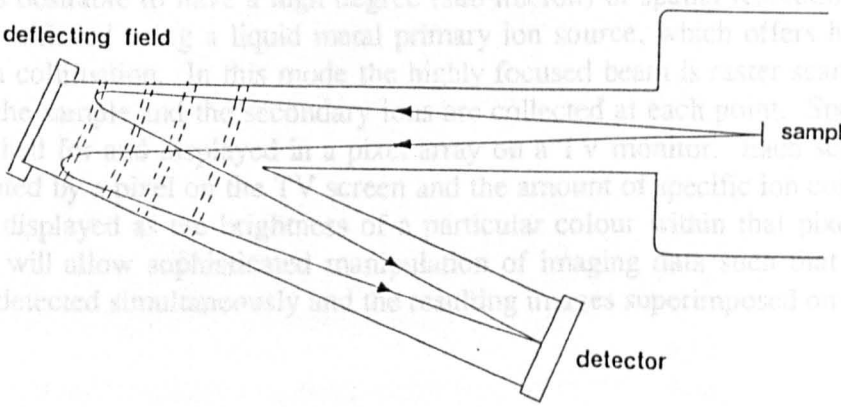

Figure 3.13: Reflectron time of flight mass spectrometer

requirement, therefore dynamic SIMS (SIMS used for depth profiling) cannot be achieved using ToF mass spectrometers.

3.3.3.4 Sample preparation and handling

A problem associated with SIMS analysis of insulating materials such as polymers is surface charging, which arises from positive ion bombardment and secondary electron emission. This is undesirable as negative ions cannot escape from the surface and positive ions will be ejected with too high an energy for analysis. The problem can be overcome by flooding the sample surface with low energy electrons during acquisition. This procedure, known as charge neutralisation or charge compensation, can be continuous in the case of noble gas ion sources or pulsed in the case of metal ion sources. This process is aided considerably by use of a sample mount in which the sample can be inserted on a spring loaded platform beneath a metallic grid. The sample is pushed against the grid which divides the sample into small areas. This localises surface potential differentials and the grid conducts away any build up of charge.

3.3.4 Information available from SSIMS

There are two modes of operation available in SSIMS; spectral acquisition and imaging.

3.3.4.1 Spectral acquisition

The first mode of operation is the acquisition of positive or negative secondary ion spectra. The polarity of spectra is determined by the bias applied to the sample. The great advantage of this analysis technique over XPS is that molecular as well as atomic information is obtained, and for polymers, "fingerprint" spectra can be routinely acquired which involve spectral peaks arising from ionised fragments of multiple polymeric repeat units. The disadvantage of the technique however, is that spectral information is not directly quantifiable.

3.3.4.2 Imaging

The second mode of operation allows a chemical map of the surface to be made. To do this, it is desirable to have a high degree (sub-micron) of spatial resolution and this can only be achieved using a liquid metal primary ion source, which offers high brightness and high collimation. In this mode the highly focused beam is raster scanned across an area of the sample and the secondary ions are collected at each point. Specific ions can be searched for and displayed in a pixel array on a TV monitor. Each scanned point is represented by a pixel on the TV screen and the amount of specific ion collected at each point is displayed as the brightness of a particular colour within that pixel. Most data systems will allow sophisticated manipulation of imaging data such that many species may be detected simultaneously and the resulting images superimposed on each other.

3.4 XPS studies of polymers, copolymers and polymer blends

The original work on the application of XPS to polymers was performed by Clark and his co-workers [34] in the 1970's and early 1980's. A review of this work has been presented by Dilkes [35]. More recently, Beamson and Briggs [36] have utilised the high resolution Scienta ESCA 300 instrument to provide a database of organic polymers. Related studies on the Scienta by this group has provided new spectral interpretations on XP spectra in terms of vibrational asymmetry [37], differences in linewidths, inelastic scattering effects, non-stoichiometry effects due to shake-up and shake-off transitions, surface specific states [38] and primary and secondary oxygen induced C 1s binding energy shifts [39].

A number of surface studies have been performed on polymer-polymer mixtures including blends and copolymers, in which XPS is the most surface sensitive technique employed. Here some of the more important studies are summarised.

3.4.1 Polymer-polymer mixtures which contain PDMS

Poly(dimethyl siloxane) (PDMS) is frequently used in blend and copolymer applications in which low surface energy is a requirement. PDMS has a surface free energy of 19-20 dyn cm^{-1} [40]* which is low compared to most polymers. It is expected that for a polymer-polymer mixture in which PDMS forms one component, surface enrichment of PDMS occurs. The driving force for surface enrichment is the large difference in surface free energies. As a result, an important part of characterisation of such materials is surface analysis.

In 1983 Sha'aban *et al* [41] reported on the surface behaviour of PDMS-urethane copolymers and their blends with segmented polyether-urethanes. Conventional polyether urethanes are prone to hydrolytic attack and blending with small amounts of PDMS-urethane copolymer has been shown to increase surface hydrophobicity. Blends containing between 0.5 and 6.5% by weight of the PDMS-urethane were prepared, and XPS spectra of the C1s, O1s and Si2p core levels were acquired from dip-cast samples of the blends and the "neat" components. Through the use of take off angles which provided analysis depths of between 2.5 and 10nm, it was found that the neat polyether-urethane was covered with mostly poly(tetramethylene oxide) (PTMO) soft segments mixed with very small amounts of urethane hard segments. The neat PDMS-urethane consisted of an overlayer of PDMS segments estimated to be at least 5nm thick. For the blends, the trend towards complete surface enrichments of PDMS began at between 1 and 2% PDMS-urethane content. Additionally, in accordance with surface free energy expectations, immediately below the PDMS layer could be observed PTMO soft segments and finally a layer of hard urethane segments.

This is a common result for systems which contain PDMS. Patel *et al* [42] investigated the surface behaviour of polysulphone-PDMS block copolymer both in its neat form and in blends with homopolysulphone at copolymer concentrations ranging from 0.1 to 50% by weight. The neat copolymer exhibited a surface enrichment of PDMS to an

* see reference 109

estimated depth of 5nm. When blends were examined, even at copolymer bulk concentrations of 0.1% there was a surface coverage of PDMS in excess of 50%. At around 1% copolymer concentration, total surface enrichment by PDMS was observed.

Other surface studies on similar systems include work on polyurethane-PDMS copolymers by Tezuka *et al* [43], Li and Huang's study of high density polyethylene blended with polyethylene-PDMS graft copolymer [44], and work on bisphenol A polycarbonate (BPAPC)-PDMS block copolymer by Schmitt *et al* [45]. The conclusion from all of these studies is this: when PDMS is present in a polymer-polymer mixture, it will migrate to the surface and form an overlayer, even at very small concentrations of PDMS. These observations are of particular importance in the present study, in which PDMS has been observed as a contaminant.

3.4.2 Polystyrene/poly(ethylene oxide) block copolymers

Two studies of significance were performed on PS-PEO copolymers, one on diblock copolymers by Thomas and O'Malley [46] and the other on triblock PEO-PS-PEO copolymers by O'Malley *et al* [47]. Two aspects of this system are of note. Firstly, there is a significant surface free energy difference between the two homopolymers (PS, 36dyn cm^{-1}; PEO, 44dyn cm^{-1} [48]). Secondly, PEO is a partially crystalline polymer.

For the diblock copolymers, three types were synthesised, containing 20%, 40% and 70% by weight polystyrene. The copolymers obtained in powder form were cast from three different solvents onto aluminium substrates: ethylbenzene, a preferential solvent for PS; nitromethane, a preferential solvent for PEO; and chloroform, a mutual solvent. Angle dependant XPS was performed to provide information up to a depth of 5nm. The study found that for each copolymer analysed, the surface was significantly richer in PS than the bulk, regardless of PS content in the copolymer, and that the concentration of PS at the surface was affected by its solubility with the casting solvent, *i.e.* the ethylbenzene cast samples were more surface enriched by PS than the nitromethane cast samples.

The triblock copolymer study confirmed these findings. In addition, both studies observed that lateral inhomogeneities were in evidence and that the PS component was often raised above the PEO component. This was probably as a result of the crystallinity of the PEO phase.

3.4.3 Polystyrene/poly(vinyl methyl ether) blends

The first surface studies on an amorphous binary polymer blend was on the PS/PVME system, first reported by Pan and Prest [49]. This blend system had been shown to be miscible in all proportions at room temperature when cast from toluene, but phase separated when cast from trichloroethylene (TCE) [50,51]. Again a significant difference in the surface free energies existed (PS, 36dyn cm^{-1}; PVME, 29dyn cm^{-1} [48]) this time in favour of the PVME component. Miscible and immiscible blends across the composition range were cast from toluene and TCE respectively and samples

for XPS analysis were dip-coated onto Al stubs. Angular dependant XPS showed that all blends were significantly enriched in PVME, that the degree of surface enrichment increased as the probing depth decreased, and that phase separated blends showed a greater degree of surface enrichment than the miscible blends.

A further study was performed by Bhatia *et al* [52] in which only miscible PS/PVME were examined by XPS across the composition range. This time the surface characteristics were studied as a function of varying the molecular weight of the PS component. Again, PVME was found to substantially enrich the surface of all compositions, even for those with low PVME bulk concentration. Additionally a power law dependence ($M_n^{-2/3}$) of the PS molecular weight on surface composition was observed. Finally, the angle dependant XPS showed that the PVME surface enrichment followed a concentration gradient which could be mathematically fitted to a hyperbolic cotangent profile.

3.4.4 Poly(vinyl chloride)/poly(methyl methacrylate) blends

XPS studies have been performed on PVC/PMMA blends [53,54]. As this is the main blend system to be examined in the present study, past studies on both bulk and surface characteristics are presented in the final section of this chapter, section 3.6.

3.5 SSIMS studies of polymers, copolymers and polymer blends

Prior to the start of the present study in October 1989, no static SIMS studies of polymer blends had been published. Some copolymer work had been reported and an ever-increasing number of homopolymer studies exist in the literature. The most important studies, with respect to the present work, are summarised here.

3.5.1 The Briggs series

The greatest contribution to the field of static SIMS studies of polymers has been by Briggs and co-workers in their remarkable series "Analysis of Polymer Surfaces by SIMS", a series that so far consists of fifteen papers. The first paper [55] addressed four significant problems; (i) the expected high rate of ion beam damage, (ii) the need for charge compensation provided by electron flooding, leading to (iii) the possibility of electron stimulated ion emission (ESIE) and (iv) the uncertainty of the surface potential. The problems were illustrated by performing SSIMS analysis on PS, poly(ethylene terephthalate) (PET) and a paraffin wax film. A 2-4keV Ar^+/Ne^+ source was used with a quadrupole analyser, charge neutralisation being provided by a defocused 1μA, 700eV electron flood gun. The paper referenced earlier work by Gardella and Hercules [56] in which SSIMS had supposedly been performed on a series of acrylic polymers. Their

results however had shown evidence of fragmentation structures which could only occur as a result of extremely high ion doses, hence taking the analysis beyond the static regime. Such fragments were not detected with the relatively low ion doses of the Briggs and Wooton study. What was clear however, was the major complexity involved with the introduction of the electron flood, resulting in the occurrence of ESIE albeit on a small scale. The paper concluded that the control of surface potential is paramount to reproducibility of SSIM spectra and that the contribution of ESIE has to be considered when using such high energy electron floods.

The second paper [57] introduced the concept of obtaining reproducible SSIMS fingerprint spectra from polymer films. A number of simple polymer films were analysed using the same experimental set-up as in the first study. From the positive ion spectra of each polymer it was found that each spectrum contained sufficient unique characteristics to be used in the fingerprint mode. Additionally, the spectral peaks for each polymer could be interpreted in terms of fragmentation mechanisms used in electron impact (EI) mass spectroscopy. ESIE was once again found to be in evidence although only low mass secondary ions were produced. The high mass fingerprint peaks were due to secondary ions desorbed only by primary ion impacts.

In paper three of the series [58], the potential of SIMS for molecular imaging was demonstrated, and the first SSIMS images, showing spots of silicone oils deposited on a low density polyethylene surface was presented. Even at this very early stage it was predicted that much greater spatial resolution would be available for liquid metal ion sources using a time of flight analyser. At the time of publication, such instruments were not available.

Paper four [59] presented detailed fingerprint positive ion spectra for a number of acrylates and methacrylates. A significant aspect of this study was the first indication that poly(butyl methacrylate) which had been analysed in three different isomeric forms, produced three distinct fingerprint spectra.

An article [60] published between parts four and five, but which surprisingly was not considered to be part of the series, introduced a number of new ideas. Firstly, that negative ion spectra could be useful in polymer surface analysis - the first negative ion spectrum of PEO being presented. Secondly, the paper gave rise to optimism that partial quantification might be possible with SSIMS, citing work in which the peak intensity of a fragment unique to one component of a block copolymer had been ratioed to the peak intensity of a fragment which was common to both components, yielding positive results. Thirdly, the delineation of three different dose regimes was proposed: up to 10^{12} ions cm^{-2} - negligible damage; between 10^{12} and 10^{13} ions cm^{-2} - tolerated damage; beyond 10^{13} ions cm^{-2} - severe damage. Finally, the first use of imaging SSIMS with a liquid metal ion source (Ga^+) was demonstrated with a high resolution image of a carbon fibre/thermoplastic composite fracture surface.

The fifth paper [61], stimulated by the use of high energy Ga^+ ion sources, set out to investigate the effect of primary ion mass and energy on secondary ion yields. This was done by comparing the SIM spectra obtained for a number of previously studied polymers, using both noble gas ion sources and a Ga^+ source, at a number of different beam energies. The general trend found was that as the primary ion mass increased, so

did the total secondary ion yield and so did the yield of high mass clusters. This was also the effect shown when the energy of the primary ions increased.

Paper six [62] demonstrated the detection of cyclic trimer on the surface of a poly(ethylene terephthalate) film, while paper seven [63] presented a comprehensive SSIMS study of every nylon in commercial use. In the context of the present study the most important result from this latter paper was the peak intensity ratio study of SSIM spectra of nylon-6/nylon-66 copolymers. Several samples of the copolymer had been studied across the copolymer composition range. It was found that one spectral peak at m/z=213$^+$ did not appear in the spectra of the homopolymers. The maximum intensity of this peak occurred at the middle of the copolymer composition range. The peak was identified as being due to the fragments of material from each of the copolymer components. This result is reproduced in figure 3.14, along with a plot of the m/z=114$^+$ peak. This peak is due to a structure unique to nylon-6. Both results are plotted against the percentage of nylon-6 in the copolymer, and both are ratioed against the intensity of the m/z=55$^+$ peak, a peak common to both homopolymers.

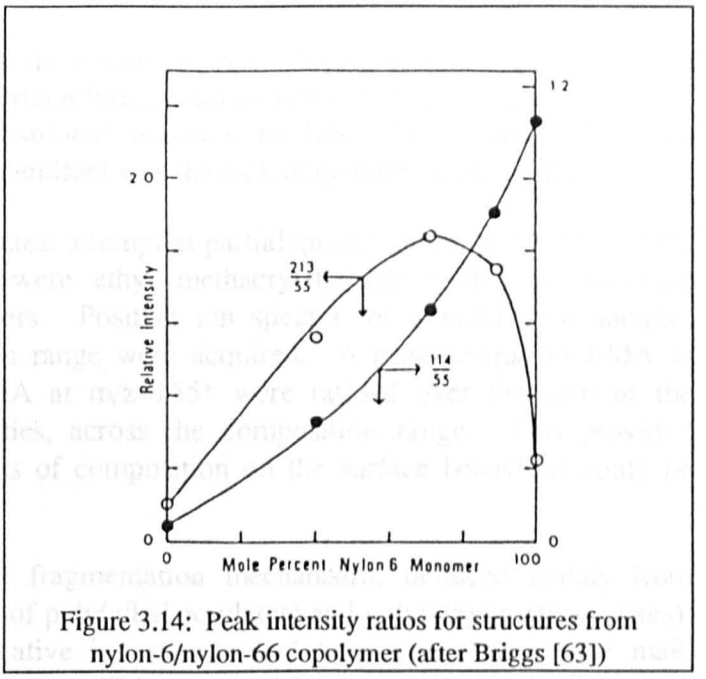

Figure 3.14: Peak intensity ratios for structures from nylon-6/nylon-66 copolymer (after Briggs [63])

Papers eight and nine [64,65] were the first studies to methodically examine the surface of a "real" material application by means of the combination of XPS and SSIMS. In this case it was the study of segmented poly(ether urethanes) (PEU's) which have considerable importance in biomedical applications. Paper 8 gave the results of preliminary studies on model PEU's whilst paper 9 concentrated on PEU's with fluorinated chain extenders. In addition to shedding new light on the soft segment/hard segment surface behaviour of these materials, the studies generated a number of important general results. Firstly, while both XPS and SSIMS have strong and weak points, their combined use provides an enhanced surface characterisation to be performed. For example, SSIMS can distinguish between three types of polyether soft segments (not possible with XPS), while XPS can distinguish between PEU and PEU-urea (not possible with SSIMS). Also, although the surface sensitivity of SSIMS is greater than XPS, the latter method allows *non-destructive* depth profiling up to a depth of 10nm. Finally, quantification of XPS is well understood, but partial quantification by means of the ratioing of peak intensities is available to SSIMS. Perhaps the most important aspect of this work was in its estimation of the sampling depth of SSIMS. This was done by obtaining the intensity ratio of the m/z=19$^-$ peak (F^-) to the m/z=13$^-$ peak (CH^-) from the negative ion SSIM spectra for a number of compositions. The quantified XPS F/C ratios were then obtained for the samples at a number of take off

angles. These were plotted against the SSIMS I_{19}-/I_{13}- data. The best correlation between the two sets of data was for the XPS results using a take off angle of 10° (as defined in figure 3.9, page 39). The estimated XPS sampling depth for this take off angle was estimated as being *ca.* 1nm, and this was the inferred value of the SSIMS sampling depth.

Part ten of the series [66] explored the possibility of employing SSIMS rather than or in addition to XPS for identifying surface functionalities labelled by derivatizing reagents. The study used isotopically substituted reagents to label PVA films. Although successful, one of the drawbacks identified was the lack of quantification ability.

The eleventh paper [67] was the latest attempt at partial quantification of SSIM spectra. This time the samples studied were ethyl methacrylate/hydroxyethyl methacrylate (EMA:HEMA) random copolymers. Positive ion spectra for a number of samples across the copolymer composition range were acquired. A peak unique to EMA at m/z=127$^+$ and one due to HEMA at m/z=155$^+$ were ratioed over the sum of the m/z=127$^+$ and m/z=155$^+$ intensities, across the composition range. This provided smooth trends in which the effects of composition on the surface behaviour could be observed.

Paper twelve [68] gave detailed fragmentation mechanisms, deduced mainly from negative ion spectra, for a number of poly(alkyl acrylates) and poly(alkyl methacrylates). This was the first time that negative ion spectra had been proposed as the main fingerprint spectra for such polymers. This was mainly due to the ability of many negative ion fragments to retain an intact ester side chain, and the negative ion spectra not being congested with hydrocarbon cluster information.

A standard analysis sample was proposed in paper thirteen [69] for the assessment of the performance of SSIM spectrometers. Polytetrafluoroethylene (PTFE) tape was the material proposed for evaluating absolute instrument sensitivities for positive and negative ion spectra, and for the assessment of charge neutralisation ability.

Paper fourteen [70] re-examined a series of aliphatic hydrocarbons previously studied by van Ooij and Brinkhuis [71]. It was found that the latter study had used ion doses in excess of the static regime. New spectral fingerprints were ascribed to each polymer which were free from ion dose damage.

Finally, paper fifteen [72] examined the change in SSIM spectra on aliphatic oxygen containing polymers as a function of systematic variation in structure, with respect to reactive functional groups such as ketone and epoxy moieties.

To conclude, in the space of ten years, thanks mainly to this series, the field of SSIMS studies of polymer surfaces has developed from a fragile, hardly explored analysis route fraught with problems, to a largely routine surface analysis technique.

3.5.2 High mass analysis using ToFSIMS

The advent of time of flight SIMS has enabled very high mass detection for polymer surfaces with negligible damage. Bletsos *et al* [73], Lub *et al* [74] and van Leyen *et al* [75] demonstrated this capability for polystyrene low molecular weight standards. These are monodisperse polymers with highly controlled molecular weights. In each study, a selection of these standards were dissolved in toluene and then deposited onto silver substrates prior to analysis. The studies found three main results: (i) if the deposited film was of the correct thickness (*ca.* one or two monolayers) then intact oligomeric chains could be sputtered from the surface as Ag^+ cationised species. An oligomer distribution was then observed in the mass range between 600 and 10,000amu. (ii) Chain scission of the polymer backbone occurred and these too could be detected as Ag^+ cationised species. The m/z values at which these species were detected gave an exact indication of the fragmentation schemes resulting from the scission. (iii) The SSIM spectrum in the mass range below 200amu was dominated by stable aromatic ions and the two isotopes of silver. These studies have enabled users of ToFSIMS instruments to check high mass sensitivity, to internally calibrate the detection system at high mass and to compare the performance of their instrument with similar instruments at other establishments.

The Ag^+ cationised polystyrene oligomer distribution was employed by O'Toole *et al* [76], who used ToFSIMS to monitor changes in molecular weight which occurred as a result of UV irradiation. It was found that the oligomer distribution was obliterated after 15 days continuous irradiation, and this was attributed to UV-induced chain scissions in the oligomer chains at the surface.

3.5.3 Combined XPS and SSIMS studies

As described in section 3.5.1 the development of SSIMS as applied to polymer surfaces took place from the early 1980's onwards. Although the value of combined XPS and SSIMS studies was recognised, it was not until the studies by Hearn *et al* [64,65] in the late 1980's that a direct correlation between SSIMS and XPS was reported. Since then, a number of combined SSIMS and XPS studies on polymeric materials have appeared, most notably in the area of pharmaceutical polymers by Davies and co-workers. This work has contributed new surface information on poly(butyl methacrylate) colloids [77], bioactive polyesters [78], polyorthoesters [79] and polyanhydrides [80]. Bhatia and Burrell [81] have applied the combination to segmented block copoly(ether-esters), and Waddington and Briggs [82] have used the two techniques to shed new light on the adhesion mechanisms between polymeric coatings and polypropylene.

The only known example in the literature of a combined XPS/SSIMS study on a polymer blend is by Thompson [83] who examined immiscible blends of bisphenol-A polycarbonate (BPAPC) and polystyrene and miscible blends of tetramethyl bisphenol-A polycarbonate (TMPC) and polystyrene, both over the whole composition range. By correlating the results from both techniques, partial quantification for the SSIMS results were displayed in which the peak intensities of ions unique to the polycarbonate were ratioed to peaks due to both polymers in the blend. This ratioing technique was very similar to that first demonstrated by Briggs [63]. The Thompson paper also showed a

SSIMS image of an immiscible blend, in which the spatial distribution of BPAPC was observed by the chemical mapping of O^- ions in a 50/50 BPAPC/PS blend.

These studies have shown that the maximum amount of surface structural information is attained by analysing surfaces using both XPS and SSIMS. It is likely that future surface studies will be deemed incomplete without consideration by both techniques.

3.5.4 Partial quantification of SSIM spectra

The standard approach to partially quantifying SSIM spectra has already been outlined in previous sections, and involves a direct comparison between two or more peaks by a ratioing of peak intensities [63-65, 67, 83]. A novel approach was used by Alexander [84], in which the intensities of spectral peaks of interest were *normalized* over an arbitrary mass range, *i.e.* the sum of counts across peak X was divided by the sum of counts across the mass range Y. If a constant mass range is used, normalized peak intensities for several spectra can be directly compared, negating effects due to slight variations in primary beam current, output voltages of the analyser supply system, and sample position and orientation. This approach has been successfully utilised on SSIMS studies of photo-oxidised polystyrene [85], in which a set of normalized peak intensities acquired from adjacent sampling areas of the same specimen were found to be consistent within $\pm$ 8%.

3.6 Studies on blends of PVC and PMMA

The blend system that was chosen for the present study was that of PVC and PMMA. The reasons for choosing this system were threefold: (i) like PS/PVME, it is a system for which both miscibility and immiscibility has been reported by using different mutual solvents. (ii) The reported values of surface free energy for the two homopolymers are within 1 dyn cm^{-1}. Resulting surface studies have been the subject of disagreement in the literature. (iii) It is a system which has previously been studied by XPS but not by SSIMS, making it an ideal system to fit the objective of this study.

In this section, past studies on bulk miscibility of the system, XPS studies on homopolymers and blends, and SSIMS studies on homopolymers will be summarised.

3.6.1 Bulk miscibility studies

PVC represents one of the most intensively investigated components of polymer blends. It is found to be miscible with a number of polymers, due to its ability to take part in weak specific interactions by means of the α-hydrogen of its repeat unit. This can hydrogen bond, especially with polymers which contain base type components such as carbonyl groups or amides. Because of the presence of a carbonyl group in PMMA (see

figure 3.15(a)), it would be expected that this would interact with the PVC α-hydrogen as in figure 3.15(b). The classification of this type of interaction is the subject of debate in the literature. Coleman *et al* [13] describe it as a relatively weak hydrogen bond between the carbonyl group and the methine proton of PVC. Vorenkamp and Challa [86] describe the interaction as being either a dipole-induced dipole type between the carbonyl group and the C-Cl bond of PVC, or a Lewis acid-base type of interaction.

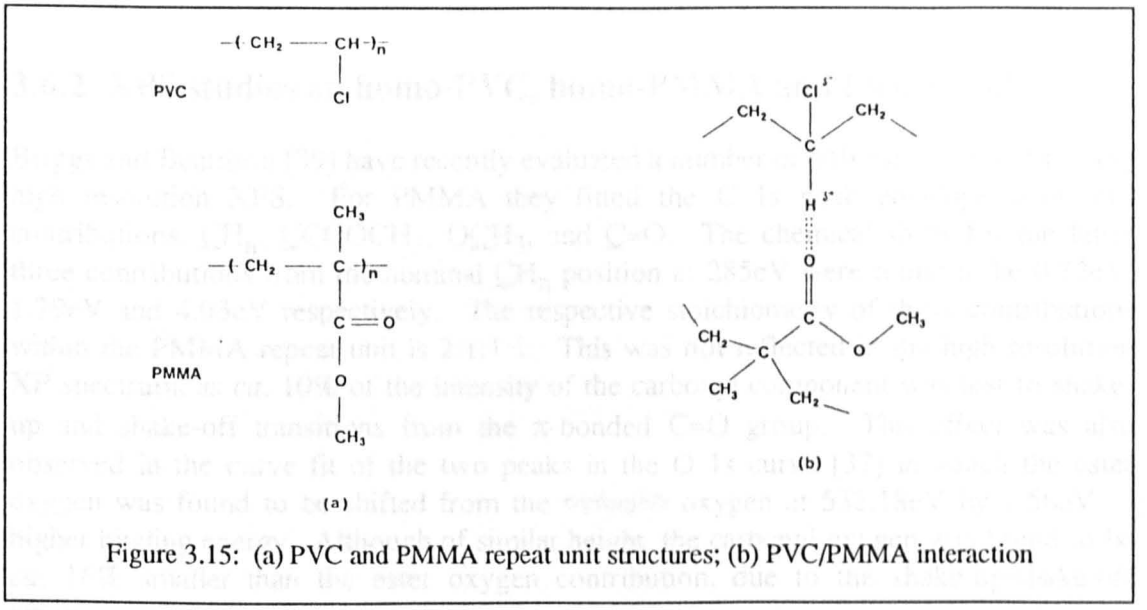

Figure 3.15: (a) PVC and PMMA repeat unit structures; (b) PVC/PMMA interaction

The latter description is preferred by Olabisi *et al* [87], who classify the interaction as a weak acid-base type in which the PVC acts as a proton donor and the PMMA carbonyl is a proton acceptor.

In a review of miscible polymer blends in the late 1970's, Krause [88] could only describe the miscibility of PVC/PMMA blends as "ambiguous" due to the difficulty experienced in obtaining blends with single glass transition temperatures. Razinskaya *et al* [89] examined blends solution cast from tetrahydrofuran (THF) by scanning electron microscopy. Across the composition range it was found that the blend existed as a two phase mixture. For PMMA concentrations up to 70%, PMMA existed as a dispersed domain phase within a continuous PVC phase. At between 75 and 80% PMMA concentration, phase inversion occurred, beyond which PMMA formed the continuous phase and PVC formed a disperse droplet phase. The reason suggested for the phase inversion being displaced in the direction of higher PMMA content was the higher tendency of PVC, relative to PMMA, to form associates in solution resulting in gel formation as the film formed. For PMMA concentrations between 50 and 70%, multiple emulsions were observed, in which PVC solution drops were "captured" by the PMMA dispersed domains. It was estimated that at 60% PMMA concentration, approximately 10% of the PVC was entrapped by the PMMA dispersed phase.

Walsh and McKeown [90] investigated the miscibility of a number of polyacrylates and polymethacrylates blended with PVC, all solution cast from butan-2-one. Dynamic mechanical thermal analysis was performed on each blend. It was found that all the polymethacrylate/PVC films at all compositions were optically clear and had one glass transition temperature. These blends were therefore deemed to be miscible. Later

studies by Jager *et al* [91] and Tremblay and Prud'homme [92] confirmed that PMMA was indeed miscible with PVC in all proportions when cast from butan-2-one. The study by Jager used cloud point curves to assess that the blend was a LCST type and that the LCST was in excess of 150°C, although the exact value could not be confirmed due to the high viscosity of the blends and subsequent low mobility of the polymer chains.

3.6.2 XPS studies on homo-PVC, homo-PMMA and their blends

Briggs and Beamson [39] have recently evaluated a number of polymer XP spectra using high resolution XPS. For PMMA they fitted the C 1s peak envelope with four contributions, $\underline{C}H_n$, $\underline{C}COOCH_3$, $O\underline{C}H_3$, and $\underline{C}$=O. The chemical shifts for the latter three contributions from the nominal $\underline{C}H_n$ position at 285eV were found to be 0.72eV, 1.79eV and 4.03eV respectively. The respective stoichiometry of these contributions within the PMMA repeat unit is 2:1:1:1. This was not reflected in the high resolution XP spectrum, as *ca.* 10% of the intensity of the carboxyl component was lost to shake-up and shake-off transitions from the π-bonded C=O group. This effect was also observed in the curve fit of the two peaks in the O 1s curve [37] in which the ester oxygen was found to be shifted from the carboxylate oxygen at 532.18eV by 1.56eV to higher binding energy. Although of similar height, the carbonyl oxygen was found to be *ca.* 16% smaller than the ester oxygen contribution, due to the shake-up/shake-off effect.

The narrow scan XP spectra for PVC have also been evaluated by high resolution XPS [36], where the two contributions to the C 1s curve are listed as 285.4eV ($\underline{C}H_n$) and 286.5eV ($\underline{C}$-Cl), and the Cl 2p peak (a doublet due to multiplet splitting), has Cl $2p_{3/2}$ listed at 200.5eV and Cl $2p_{1/2}$ at 202.3eV.

There have been two XPS studies on PVC/PMMA blends, by Busscher *et al* [53] and by Schmidt *et al* [54]. Busscher made melt-cast blends prepared on a two roll mill. Contact angle measurements were used to determine the surface free energies of the homopolymers. These values were 44 dyn cm^{-1} for PVC and 56 dyn cm^{-1} for PMMA. From this large surface free energy difference, surface enrichment of the PVC component was expected and observed by XPS.

This was contrary to the observations of Schmidt, who prepared solution cast blends from both THF and butan-2-one to obtain immiscible and miscible blends respectively. The values of surface free energy for the homopolymers were quoted from previous studies as 41.2 dyn cm^{-1} for PMMA [93] and 42 dyn cm^{-1} for PVC [94]. If surface enrichment was to occur it would therefore be more likely to be by the PMMA component. From XPS results, values of the carbon to oxygen ratio for each blend across the composition range were obtained and the surface weight percentage of PMMA, ω, was determined for each blend using the following equation:

$$\frac{2(1-\omega)/62.5}{5\omega/100.15}+1=\frac{(C/O)_{blend}}{(C/O)_{PMMA}}. \qquad ...(3.9)$$

For the miscible blends it was found that there was a slight surface excess of PMMA which was within error limits of the bulk composition. For the immiscible blends a considerable surface excess of PMMA was observed. Depth profiling for both types of blend showed no difference in composition throughout the XPS information depth.

3.6.3 SSIMS studies on homo-PVC and homo-PMMA

Standard PVC and PMMA spectra, obtained using a noble gas ion source and quadrupole analyser can be found in Briggs Brown and Vickerman's handbook [95]. The PVC positive ion spectrum is essentially a series of hydrocarbon clusters similar to that of polyethylene. The negative ion spectrum contains the two isotopes of chlorine at m/z=35$^-$ and 37$^-$ and Cl_2^- at m/z=70$^-$. The PMMA positive ion spectrum also contains mainly polymer "backbone" structure and also two main peaks at m/z=59$^+$ and 69$^+$ due to $CH_3O\text{-}C{\equiv}O^+$ and $CH_2C.CH_3.C{\equiv}O^+$ respectively. There is also a cyclic backbone peak at m/z=121$^+$. Most of the fingerprint information however is contained in the

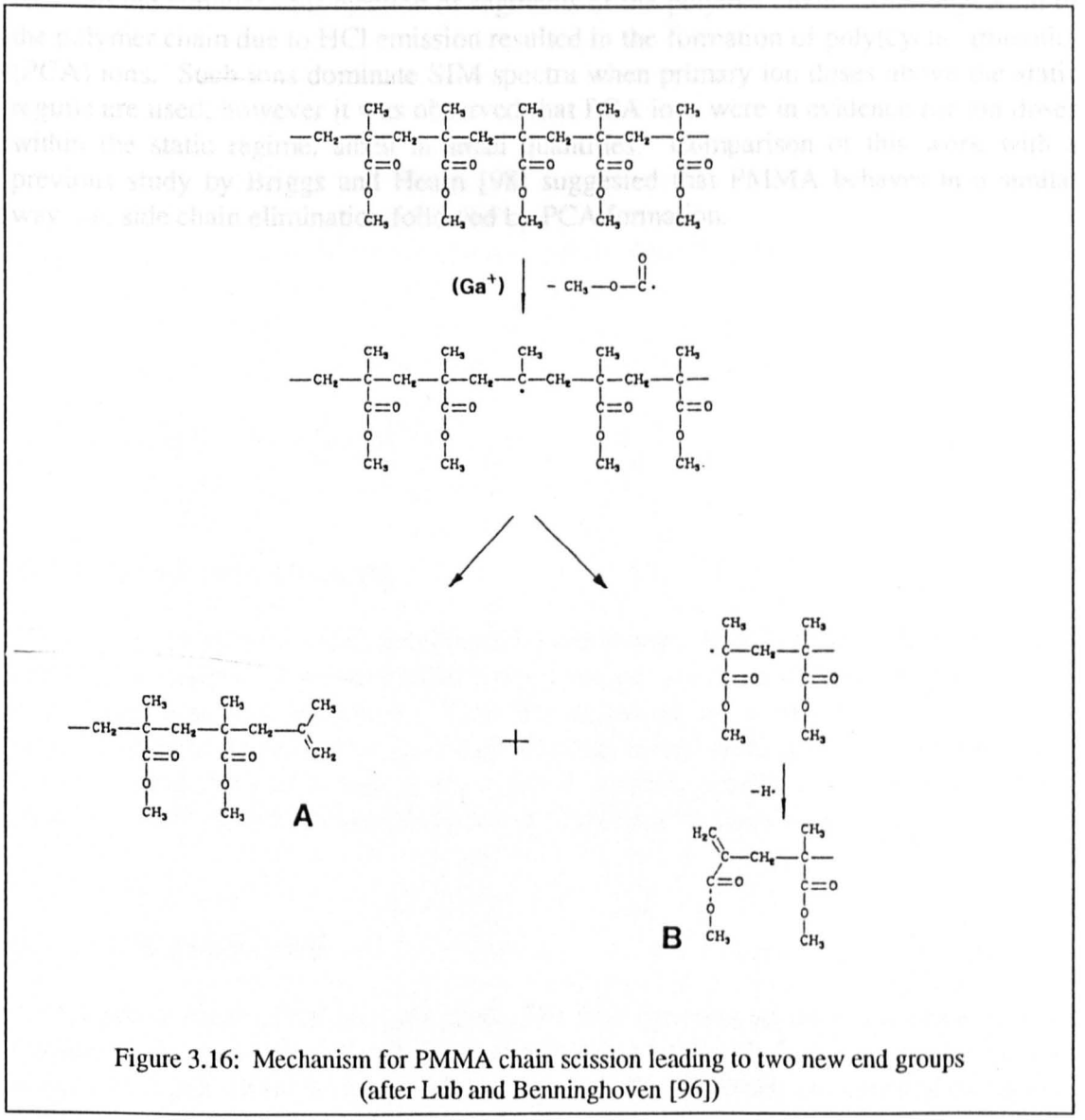

Figure 3.16: Mechanism for PMMA chain scission leading to two new end groups (after Lub and Benninghoven [96])

negative ion spectrum. Significant peaks occur at m/z=16$^-$ (O^-), 17$^-$ (OH^-), 31$^-$ (CH_3O^-), 55$^-$ (CH_2=CH−C≡O^-), 85$^-$ (CH_2=C.CH_3.COO^-), 101$^-$ (M^--H where M is the PMMA repeat unit), 141$^-$ (M^--C.CH2.=CH3) and 185$^-$ (M+85$^-$). The accepted chain scission mechanism for PMMA which leads to these structures is shown in figure 3.16 and was proposed by Lub and Benninghoven [96] based on arguments originally presented by Hearn and Briggs [68]. The mechanism is as follows: an incoming primary ion causes the loss of a carbonyl containing side chain. This leaves a free radical on the β carbon, which causes a chain scission to occur and the formation of two chains, A and B. The free radical transfers to the adjacent repeat unit β carbon (now chain B) while the original β carbon forms a saturated chain end to chain A. A hydrogen radical is then eliminated from chain B to form the chain end shown. Lub and Benninghoven predict that the peak occurring at m/z=141$^-$ originates at chain end A and that the peak at 185$^-$ comes from chain end B. Implicit in these predictions are that the m/z=31$^-$, 55$^-$ and 85$^-$ ions come from chain end B, while m/z=101$^-$ and 41$^-$ are from chain end A.

Recently, Leggett and Vickerman [97] examined the effect of high primary ion doses on PVC. They suggested that degradation of PVC by ion beams involves elimination of HCl and the simultaneous ejection of segments of the polymer chain. Rearrangement of the polymer chain due to HCl emission resulted in the formation of poly(cyclic aromatic) (PCA) ions. Such ions dominate SIM spectra when primary ion doses above the static regime are used, however it was observed that PCA ions were in evidence for ion doses within the static regime, albeit in small quantities. Comparison of this work with a previous study by Briggs and Hearn [98] suggested that PMMA behaves in a similar way, *i.e.* side chain elimination followed by PCA formation.

CHAPTER FOUR - Experimental Methods

4.1 Overview of experiments performed

The aim of the experiments in this study was to provide surface and bulk information on poly(vinyl chloride) (PVC) and poly(methyl methacrylate) (PMMA) blends across the composition range, cast from both tetrahydrofuran (THF) and butan-2-one to obtain immiscible and miscible blends respectively. A small number of films were prepared by spin casting, but the vast majority of films were made by the solution casting technique. In one set of experiments on homopolymers, a polymer film was used as supplied by the manufacturers, but this was the only occasion on which such a sample was used.

Surface information was obtained by XPS and SSIMS. A limited amount of bulk information was performed by means of differential scanning calorimetry, optical microscopy, scanning electron microscopy and Raman infra-red spectroscopy.

4.2 Sample preparation

4.2.1 Glassware cleaning

Prior to use in sample casting and distillation processes, all glassware underwent a strict cleaning procedure. First, a mild abrasive detergent was used to remove any traces of previously deposited materials. This was followed by a two hour soak in 20% concentration nitric acid. The glassware was then rinsed thoroughly with distilled water before a final rinse in a high purity organic solvent, usually Merck "Aristar" grade methanol. The glassware was then dried at 120°C in a vacuum oven.

4.2.2 Materials used

Two types of atactic PMMA were used. The first type was an industrial grade product purchased from BASF through their distributor Merck. It had a quoted molecular weight of $\bar{M}_w$=80,000 with a polydispersity of 2. The polymer was synthesised by bulk

free-radical polymerisation, using azo bisisobutylnitrile as the initiator. The second type was a secondary standard purchased from Polymer Laboratories Ltd. This had a quoted $\bar{M}_w$=61,000 with a polydispersity of 1.6. This PMMA was bulk polymerised by free-radicals, using aromatic caesium as the initiator and methanol as the terminator.

Three types of PVC were used. The first was an industrial grade BASF product with quoted $\bar{M}_w$=100,00 and polydispersity of 2. This was suspension polymerised using methyl cellulose as the suspending agent and lauroyl peroxide as initiator. The second, Fluka Selectophore, was a PVC powder normally used for GPC purposes. This had quoted $\bar{M}_w$=95,000 with a polydispersity of 2. No information was available as to the polymerization route used but it was probably suspension polymerised. Finally, a PVC sheet was used, purchased from Goodfellow. This was a suspension polymerised material with quoted $\bar{M}_w$=110,000 and a polydispersity of 2.

Reagent grade THF and butan-2-one were purchased from Aldrich Chemicals Ltd. Shortly before a quantity of solvent was used it was distilled under a nitrogen atmosphere.

4.2.3 Blend dissolution

Two kinds of polymer blend solution were prepared, one using THF as the mutual solvent, the other using butan-2-one.

Blends of PVC and PMMA across the composition range were poured into conical flasks. Solvent was then poured into the polymers such that the blend comprised 1% by weight of the solution. The flasks were then sealed with ground glass stoppers and the blends were allowed to dissolve.

The PVC dissolved fairly quickly in THF (*ca.* 1 hour at room temperature for 0.2g polymer, a typical sample quantity), but the PMMA did not. This problem could be overcome by one of two methods: (i) by heating the solution up to 60°C - dissolution of 0.2g PMMA at this temperature took *ca.* three hours; or (ii) by allowing the time necessary for the PMMA to dissolve at room temperature, *ca.* three days. The former method involved solvent loss due to evaporation which had to be replenished before the solution could be used. To save on solvent supplies, the latter method was used whenever time constraints allowed.

For the butan-2-one solutions, a similar problem occurred, except that this time it was the PVC that was difficult to dissolve. At room temperature, no matter how long the solution was left, the solvent only swelled the PVC. Dissolution of PVC would not take place below 70°C, so this was the dissolving temperature used for all blends cast from butan-2-one.

In all cases, gentle mixing of the solution with a clean glass rod speeded up the dissolution process. Complete dissolution was established by complete transparency of the solution as observed by the naked eye. Films of each blend were prepared by either spin casting or solution casting.

4.2.4 Spin casting

A widely used method of obtaining thin polymer films is that of spin casting, in which a quantity of polymer in solution is placed on a substrate disc which is then set spinning at high speed. If a small disc is used most of the polymer will be spun off with the solvent. From the small amount of solution that remains on the disc, a thin polymer film will precipitate onto the substrate as the solvent evaporates. When larger diameter substrate discs are used, none of the polymer need be lost, as the solution will spread over a large area of the substrate and a larger diameter polymer film will be precipitated.

Spin casting of PS/PVME onto aluminium substrates had been successfully performed by Bhatia [52] and this method provided the basis for making PVC/PMMA samples in the present study.

An improvised resist spinner was constructed which was capable of spinning a small aluminium stub of 10mm diameter at speeds of 1000 revolutions per minute. Thin films of each blend were prepared as follows: 50ml of solution were drawn into a glass microsyringe and injected onto an aluminium stub substrate. The resist spinner was switched on and the substrate was allowed to spin at 1000rpm for 30 seconds. Spinning had to take place within ten seconds of the solution being injected onto the substrate or else the polymer would begin to precipitate onto the stub which after spinning would result in a non-uniform, cloudy film being deposited. The substrate was then placed in a vacuum desiccator until required for analysis.

Samples cast onto aluminium stubs could only be used for XPS analysis. For ToFSIMS analysis, a small number of blends were spin cast onto clean silver substrates, using the same spin casting method.

4.2.5 Solution casting

A way of producing thicker films of polymer blends was that of solution casting, in which a film was gradually precipitated out of the solution as the solvent evaporated. When complete dissolution of the blends were established, each solution was poured into a petri dish which was placed in a vacuum oven at *ca.* 8×10^{-2} mb for 24 hours, for the purpose of solvent removal. For certain series of samples, films were precipitated directly onto the glass surface. For other series, aluminium or silver substrates were placed at the bottom of the petri dish prior to pouring the solution in, and the films were precipitated onto the substrate. When the petri dishes were removed from the oven, they were covered and placed in a vacuum desiccator until required for analysis.

A selection of films were examined to determine the effects of annealing. A range of annealing temperatures were used, from 30°C to 150°C.

4.3 Surface analysis techniques

4.3.1 Conventional XPS

A VG Scientific (now Fisons Surface Science) X-ray photoelectron spectrometer was used, with a conventional (*i.e.* non-monochromated) Al/Mg dual anode source which could be operated at a maximum power of 300W. The analyser was a CLAM 200 concentric hemispherical analyser (CHA). Energy information obtained by the detector was sent to a Digital/PDP microcomputer for processing, the instrument being controlled by VGS5250 software. The ultra-high vacuum system was based on a double stage rotary backing pump, a UHV diffusion pump charged with polyphenylether oil and fitted with a liquid nitrogen cold trap, and an auxiliary titanium sublimation pump. The XPS system formed part of a unique combined XPS/ToFSIMS instrument, the ToFSIMS part of which will be described in the next section. Introduction of samples to the sample stage (which provided three-dimensional and azimuthal movement) was via an airlock located to the side of the XPS analysis chamber.

XP spectra for the air-facing surfaces of all the spin cast samples were obtained. The typical operating power of the Mg$K\alpha$ X-ray source was 100W (10kV, 10mA). The operating pressure was *ca.* 10^{-9}mb. A take-off angle of 60° relative to the plane of the sample surface was used to give a typical sampling depth for C 1s core level electrons of 3.6nm. Widescan spectra were taken using a pass energy of 50eV. Three narrow scan spectra were also acquired of the C 1s, O 1s and Cl 2p core levels, using a pass energy of 20eV. The Cl 2p peak was always the first to be analysed as PVC is known to dechlorinate when exposed to X-ray radiation.

For the solution cast films, XPS analysis was performed on the air-facing and substrate-facing sides of the films. For blends cast directly onto glass, each film was first removed from the bottom of the petri dish by scoring the circumference of the film with a scalpel and then lifting it out using tweezers. Some films were difficult to peel from the dishes. This was a good sign as it showed that the glassware cleaning procedure was so effective as to cause adhesive bonding between the film and the glass. The removal of such films was facilitated by the injection of distilled water between the film and the glass.

For films cast onto aluminium or silver, the substrate was first removed from the bottom of the petri dish and the film was peeled from it. Again, some films were difficult to remove from the substrates. In these cases it was extremely difficult to remove the film without rupturing both the film and the substrate.

A small portion (*ca.* $1cm^2$) of the film to be analysed was cut out and mounted onto an XPS analysis stub using a 5mm x 5mm square of double sided adhesive tape. XP spectra were obtained using the same operating conditions as for the spin cast films. For each blend both the film/air and film/substrate (wherever possible) interfaces were analysed at take-off angles of 60° and 30° with respect to the plane of the sample surface, to give typical sampling depths for C 1s core level electrons of 3.6nm and 1.8nm respectively. Thus four samples were used from each film for XPS analysis.

Curve fitting of selected narrow scan spectra was performed using VGS5250 software. The parameters involved in the curve fitting procedure are explained in Appendix A.

Direct quantification from raw peak area information was obtained using appropriate sensitivity factors which had been experimentally determined specifically for this instrument. Theoretical sensitivity factors were not employed.

4.3.2 ToFSIMS

A VG Scientific (now Fisons Surface Science) IX23LS time of flight secondary ion mass spectrometer was used, and this formed the second part of the combined XPS/ToFSIMS instrument mentioned in the previous section. The source was a VG Ionex MIG300PB pulsed liquid metal (Ga^+) ion source. The analyser was a Poschenrieder type ToF analyser. To provide a secondary ion extraction field, the sample was normally held at ±5kV, depending on whether a positive or a negative ion spectrum was being acquired. Charge compensation for insulating samples was provided by a low energy (≤15eV) electron flood gun, which irradiated the sample with electrons after every tenth pulse of the primary ion beam. During the electron flood cycle, the sample bias was reduced to zero to prevent sample damage and electron stimulated ion emission (ESIE). The vacuum system was of the same type as described for the XPS system, both sides of the instrument having its own dedicated diffusion pump and sublimation pump. Mass information obtained by the detector was transferred to a Digital/PDP microcomputer via time-to-digital converters, and the system was controlled by VGX7000T software. All samples were transferred onto the three-dimensional, azimuthal sample stage directly from the XPS chamber, which was connected to the ToFSIMS chamber by an UHV gate valve.

4.3.2.1 Static ToFSIM spectra

For solution cast films, the same films which had been removed from the petri dishes for XPS analysis were used, from which a 10 x 5mm sample was cut. This was inserted into a spring loaded sample holder, the base plate of which pushed the surface of the film to be analysed against a molybdenum grid. The grid was necessary as it assisted in the charge neutralisation process discussed in chapter 3. If the grid was not used, the primary ion source, although highly focused, would cause positive charging of the whole sample. The low energy electron flood gun would reduce this charging to an extent but the relatively large area of this sample charging would render this treatment ineffective. The molybdenum grid effectively subdivided the sample area into $1mm^2$ or $4mm^2$ sample sections surrounded by molybdenum. The primary ion beam, when focused onto one of these sections could only positively charge the section under analysis, the conducting grid ensuring that none of the other sections were affected. The low energy electron flood gun could easily neutralise the positive charge accumulated over such a small area.

For the small number of thin films which had been spin cast onto silver coupons, the same sample mounting procedure was followed, using a 5x10mm sample cut from the coupon.

The sample was inserted in the ToFSIMS chamber and positive and negative ion spectrum was obtained for a number of areas on the same sample using the following operating conditions: primary beam energy, 30keV; primary ion current, 1.7nA; pulse width, 20ns; total ion dose at 200x magnification, $5x10^{12}$ ions cm^{-2}. All analyses were performed at operating pressures of between $2\text{-}5x10^{-10}$mb, and the total ion current densities used were well within the static SIMS regime, ensuring that submonolayer detection capability was maintained. The experiments were performed on the film/air and film/substrate interfaces across the composition ranges, except for the spin cast samples, in which case only the film/air interfaces could be analysed.

Spectral information acquired from different samples, and/or from different areas of the same sample, were compared using the partial quantification technique described in section 3.5.4, *i.e.* normalization of peak intensities. The intensities of the spectral peaks of interest were normalized over the total intensity of the mass range 0-100 amu. The normalized peak intensities were then plotted as a function of blend composition.

4.3.2.3 ToFSIMS imaging

A number of films were selected for ToFSIMS image acquisition. The same sample mounting procedure was used as that for spectral acquisition, i.e., a 10 x 5mm sample was cut from the film and mounted in a spring loaded sample holder beneath a molybdenum grid.

The ToFSIMS images were acquired using the following operating conditions: primary beam energy, 30keV; primary ion current, 0.16nA; pulse width, 50ns; number of pixels per image, 256x256; number of pulses per pixel, 750; total ion dose at 200x magnification, $5x10^{11}$ ions cm^{-2}. As with spectral acquisition, these images were obtained at operating pressures of between $2\text{-}5x10^{-10}$mb, the total ion current density lying within static regime limits ensuring submonolayer detection.

4.3.2.2 ToFSIMS ion dose experiments

The effects of increasing the primary ion dose from $2x10^{10}$ to $2x10^{14}$ ions cm^{-2} were investigated for two films: a Polymer Laboratories PMMA film, solution cast from butan-2-one, and a Goodfellow PVC film which was analysed as received. This was the only time an "as received" film was examined in this study. The same sample mounting procedure was used as in the previous section. Two samples of each film were used, one for positive and one for negative ion spectral acquisition.

Four ion dose regimes were delineated; low medium, high and highest dose. ToFSIM spectra were acquired using a primary beam energy of 30keV, primary current 1.5nA and a pulse width of 20ns. Once an area of sample was selected for analysis, 20 low dose spectra were acquired at 200x magnification, each spectrum inflicting a dose of $2x10^{10}$ ions cm^{-2} (12 frames). This gave a cumulative dose of $4x10^{11}$ ions cm^{-2}. Using the same analysis area, 16 medium dose spectra ($1x10^{11}$ ions cm^{-2}, 59 frames) were acquired, to give a cumulative dose of $2x10^{12}$ ions cm^{-2}. The magnification was then increased to 500x, such that the sampling area was within that of the previous dose regimes, and 14 high dose spectra ($2x10^{12}$ ions cm^{-2}, 188 frames) were acquired. This gave a cumulative dose of $3x10^{13}$ ions cm^{-2}. For the final dose regime, the magnification was increased to 1000x so that the analysis area was within that of the

previous dose regime, and 17 highest dose spectra ($1x10^{13}$ ions cm^{-2}, 235 frames) were acquired, giving a final cumulative dose on the sample of $2x10^{14}$ ions cm^{-2}. This information is summarised in table 4.1.

Table 4.1: Summary of ToFSIMS ion dose experiments

Dose regime	Magnification	No of Frames	Dose per scan (ions cm^{-2})	Number of scans	Cumul. dose (ions cm^{-2})
Low	200x	12	$2x10^{10}$	20	$4x10^{11}$
Medium	200x	59	$1x10^{11}$	16	$2x10^{12}$
High	500x	188	$2x10^{12}$	14	$3x10^{13}$
Highest	1000x	235	$1x10^{13}$	17	$2x10^{14}$

PVC and PMMA ions of interest were normalized over the mass range 0-100amu and the normalized peak intensities (NPI) were plotted against the ion dose to obtain NPI-ion dose profiles.

4.3.3 Imaging XPS

Imaging XPS was performed on a VG Scientific (now Fisons Surface Science) ESCASCOPE. A brief description of the instrument can be found in appendix B.

For XPS imaging of PVC/PMMA blends, a sample analysis area of 900μm diameter was chosen, using a 700μm field of view aperture and the instrument "zoom" facility. Al*K*α radiation was used with the X-ray source set to 15kV and 34mA (510W). The X-ray source-sample separation was ~10mm. XPS images were recorded for the Cl 2p and O1s photoelectron lines using an analyser setting of CRR4. Acquisition times were one hour per element, comprising thirty minutes for the peak image and thirty minutes for the background image, acquired in multiplex mode, where one minute was spent alternatively recording the signal from the peak and then from the background energy (~20eV lower binding energy than the peak).

4.3.4 Microanalytical XPS

XPS microanalysis was performed using a Scienta ESCA 300 instrument. A brief overview of its main features is given in appendix C.

For PVC/PMMA blends, linescans were recorded using the following instrument operating conditions: X-ray power, 2.8kW; slit width, 2.8 mm; pass energy, 300eV for narrow scans; charge compensation provided by low energy electron flood gun. Low

resolution linescans were acquired using 100s acquisition times; for high resolution this was increased to 1000s.

Linescans for Cl 2p and O1s core levels were acquired by obtaining peak and background scans, and then subtracting the background from the peak. This was done to distinguish "real" features from noise.

4.4 Bulk analysis techniques

A limited number of samples were examined by bulk analysis techniques. The operating conditions for the instruments used are briefly summarised below.

4.4.1 Differential scanning calorimetry (DSC)

DSC was performed to determine glass transition temperatures of homopolymers and selected blends. Two instruments were used, a Du Pont Instruments 910 Differential Scanning Calorimeter interfaced to a Du Pont Thermal Analyst 2000 computer, and a Mettler DSC 30 cell interfaced to an IBM PS/2 computer. For both instruments, the same experimental conditions were used.

Each sample was encapsulated in an aluminium DSC pan which was hermetically sealed. The thermal history of each sample was removed by an initial heating from ambient temperature to 120°C using a heating rate of 20°C per minute. The sample was then quenched to 0°C and reheated at a rate of 10°C per minute for T_g measurement. The glass transition temperature was taken as the onset of the glass transition region.

4.4.2 Optical microscopy

Optical micrographs were taken on a Polyvar-Met microscope at magnifications from 25x to 1000x.

4.4.3 Scanning electron microscopy (SEM)

A Camscan Series 2 instrument was used to take scanning electron micrographs. Prior to analysis each sample was sputter coated with a gold layer to make them conducting.

4.4.4 Raman infra-red spectroscopy

Raman spectra were produced using a Brooker FRA106 FT-Raman spectrometer with a Brooker IFS88 Optical Bench, a Nd-YAG laser source operating at 1.064μm and a

liquid N_2 cooled germanium detector. 200 scans were run on each sample at a total laser power of 115mW. The resolution of this spectrometer was 7 wavenumbers.

CHAPTER FIVE - Surface Studies on Homopolymers

5.1 Overview

Before the surfaces of polymer blends can be characterised, the surfaces of the homopolymers need to be examined. In this chapter surface analysis results on homo-PMMA and homo-PVC are presented, with particular emphasis on the effect of primary ion dose on the homopolymers.

5.2 XP spectra

5.2.1 XP spectra for PMMA

5.2.1.1 Results

The widescan XP spectrum for a PMMA solution cast film is shown in figure 5.1. It contains two primary peaks, The C 1s peak at *ca.* 285eV and the O 1s at *ca.* 533eV. The narrow scan spectrum of the C 1s peak is shown in figure 5.2(a) and that of the O 1s peak is shown in figure 5.2(b). The narrow scan spectrum of the C 1s curve was fitted with four contributions. The most intense contribution, due to carbon bound to itself and/or to hydrogen only, was centred at 286.6eV. The remaining three peaks in the C 1s envelope, due to $\underline{C}CO_2CH_3$, $O\underline{C}H_3$ and $\underline{C}$=O, were shifted from the

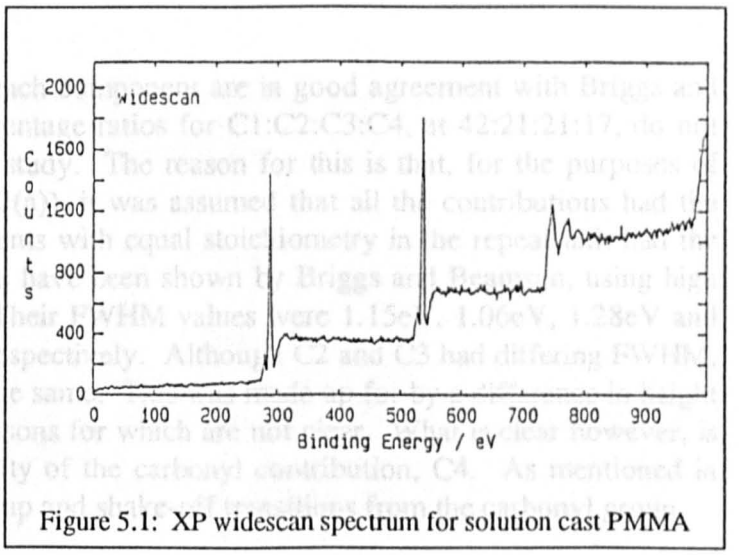

Figure 5.1: XP widescan spectrum for solution cast PMMA

main CH peak by 0.8eV, 1.8eV and 4.0eV respectively. Henceforth, the four peaks, in order of increasing binding energy, will be referenced as C1, C2, C3 and C4. The area percentage ratio of the peaks C1:C2:C3:C4 was exactly 40:20:20:20, whilst the FWHM which gave the best fit was fixed for each contribution at 1.8eV. The heights of the C2, C3 and C4 contributions were fixed to be equal, to reflect the stoichiometry of these components in the PMMA repeat unit.

The O 1s core envelope is shown in figure 5.2(b). It has two contributions, one from oxygen doubly bound to carbon at 533.9eV and the other from oxygen singly bound to carbon at 535.5eV.

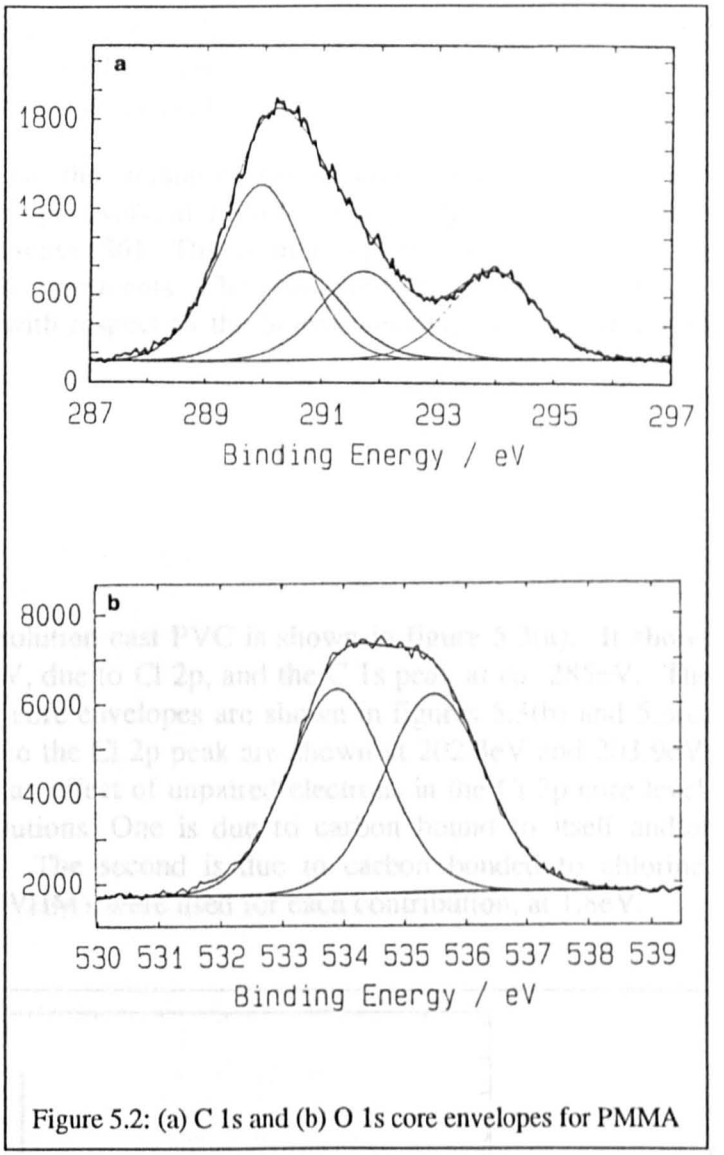

Figure 5.2: (a) C 1s and (b) O 1s core envelopes for PMMA

5.2.1.2 Discussion

The nominal value of the C1 peak position as determined by Briggs and Beamson [39] is 285.0eV. During acquisition, there was a charge build-up on the insulating sample, which had the effect of shifting the entire C 1S envelope to higher binding energy.

Whereas the chemical shifts of each component are in good agreement with Briggs and Beamson's results, the area percentage ratios for C1:C2:C3:C4, at 42:21:21:17, do not agree with those in the present study. The reason for this is that, for the purposes of fitting the C 1s curve (figure 5.2(a)), it was assumed that all the contributions had the same FWHM, and that components with equal stoichiometry in the repeat unit had the same height. These assumptions have been shown by Briggs and Beamson, using high resolution XPS, to be invalid. Their FWHM values were 1.15eV, 1.06eV, 1.28eV and 0.99eV for C1, C2, C3 and C4 respectively. Although C2 and C3 had differing FWHM, their area percentage ratio was the same. This was made up for by a difference in height of the two contributions, the reasons for which are not clear. What is clear however, is the reason for the loss in intensity of the carbonyl contribution, C4. As mentioned in chapter 3, this was due to shake-up and shake-off transitions from the carbonyl group.

Such subtleties could not be detected using the lower resolution of the VG CLAM 200 system. Despite the weaknesses of the curve-fit assumptions used, the curve fit described in figure 5.2(a) is acceptable in the context of this study.

The curve fit for the O 1s curve has the binding energy difference for the carbonyl and ester oxygen peaks, O1 and O2 respectively, at 1.59eV. This is higher by 0.03eV than the value given in the Scienta database [36]. This is an acceptable difference, given the difference in resolution of the two instruments. The peak envelope is also shifted by *ca.* 1.5eV to higher binding energy with respect to the Scienta results, due to charging of the sample surface.

5.2.2 XP spectra for PVC

5.2.2.1 Results

The XP widescan spectrum for solution cast PVC is shown in figure 5.3(a). It shows two main peaks, one at *ca.* 202eV, due to Cl 2p, and the C 1s peak at *ca.* 285eV. The expansion of the Cl 2p and C 1s core envelopes are shown in figures 5.3(b) and 5.3(c) respectively. Two contributions to the Cl 2p peak are shown at 202.3eV and 203.9eV. This is due to multiplet splitting, an effect of unpaired electrons in the Cl 2p core level. The C 1s peak has two contributions. One is due to carbon bound to itself and/or hydrogen, centred on 289.3eV. The second is due to carbon bonded to chlorine, centred at 290.5eV. The same FWHM's were used for each contribution, at 1.8eV.

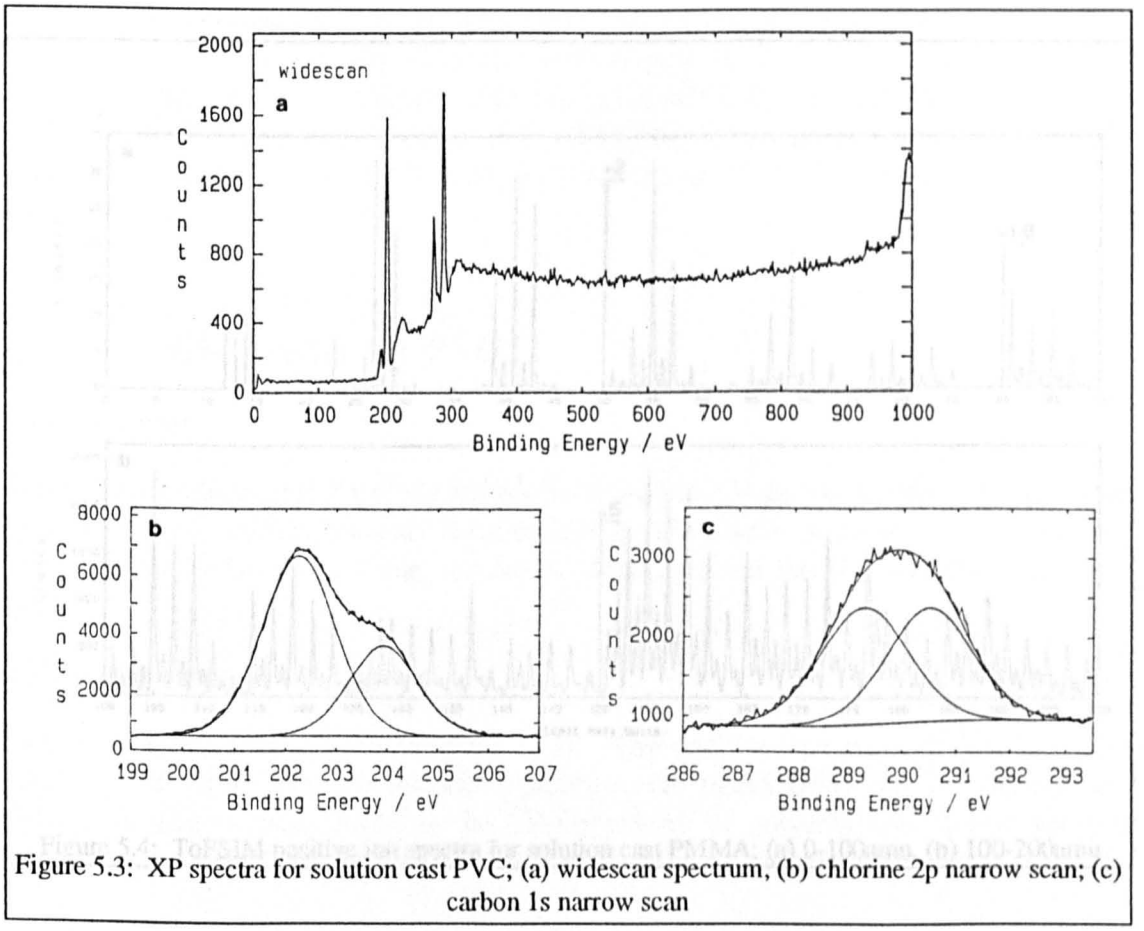

Figure 5.3: XP spectra for solution cast PVC; (a) widescan spectrum, (b) chlorine 2p narrow scan; (c) carbon 1s narrow scan

5.2.2.2 Discussion

Both the Cl 2p and the C 1s peak envelopes were shifted to high binding energy by a few eV with respect to the data given in the Scienta database. As in the case for PMMA, this was due to sample charging. The database lists the separation of the Cl $2p_{3/2}$ and the Cl $2p_{1/2}$ peaks as 1.6eV, and the separation of the two C 1s contributions as 1.1eV. The results presented here are in good agreement with these values, at 1.6eV and 1.18eV respectively.

5.3 ToFSIM spectra

Despite the IX23LS being able to provide mass information up to 10,000amu, in this study, the mass range of particular interest is from 0 to 200amu. All of the relevant spectral fingerprint information is contained within this mass range for both polymers.

5.3.1 ToFSIM spectra for PMMA

5.3.1.1 Results

Figures 5.4 and 5.5 show the positive and negative ion spectra respectively, for PMMA up to a mass of 200amu.

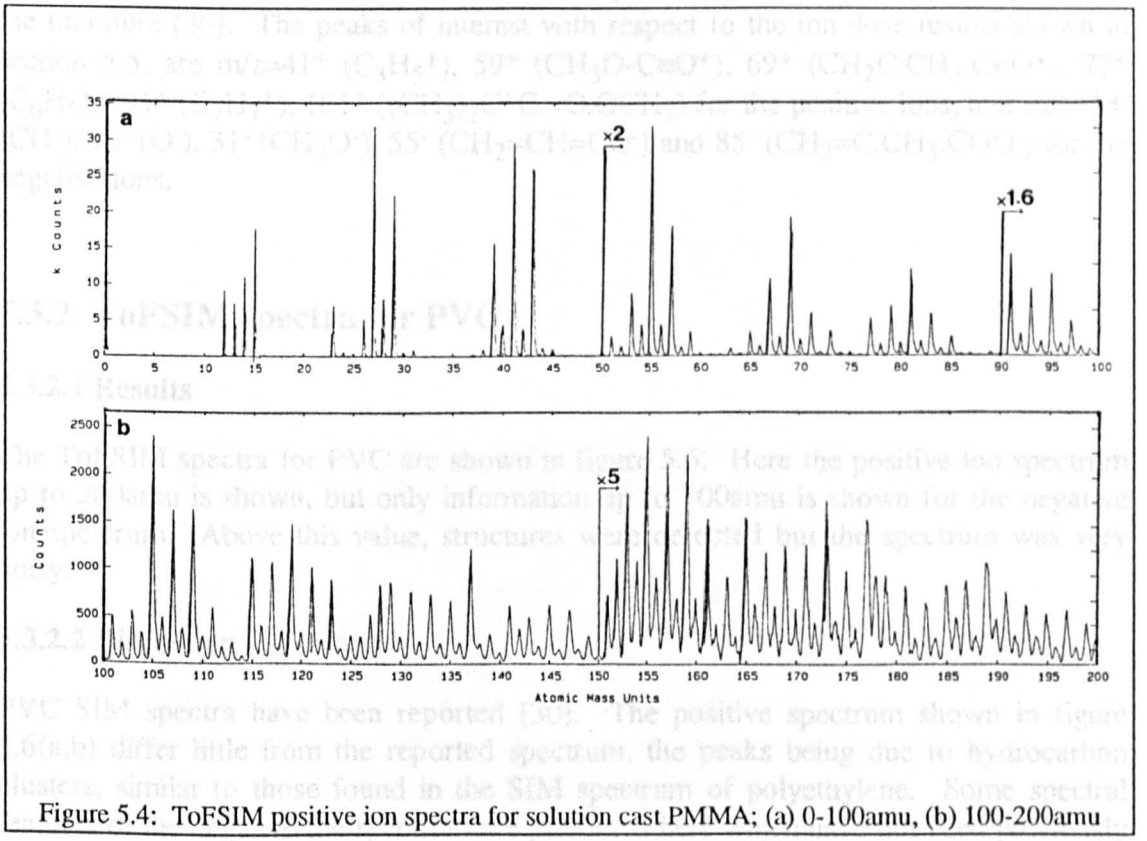

Figure 5.4: ToFSIM positive ion spectra for solution cast PMMA; (a) 0-100amu, (b) 100-200amu

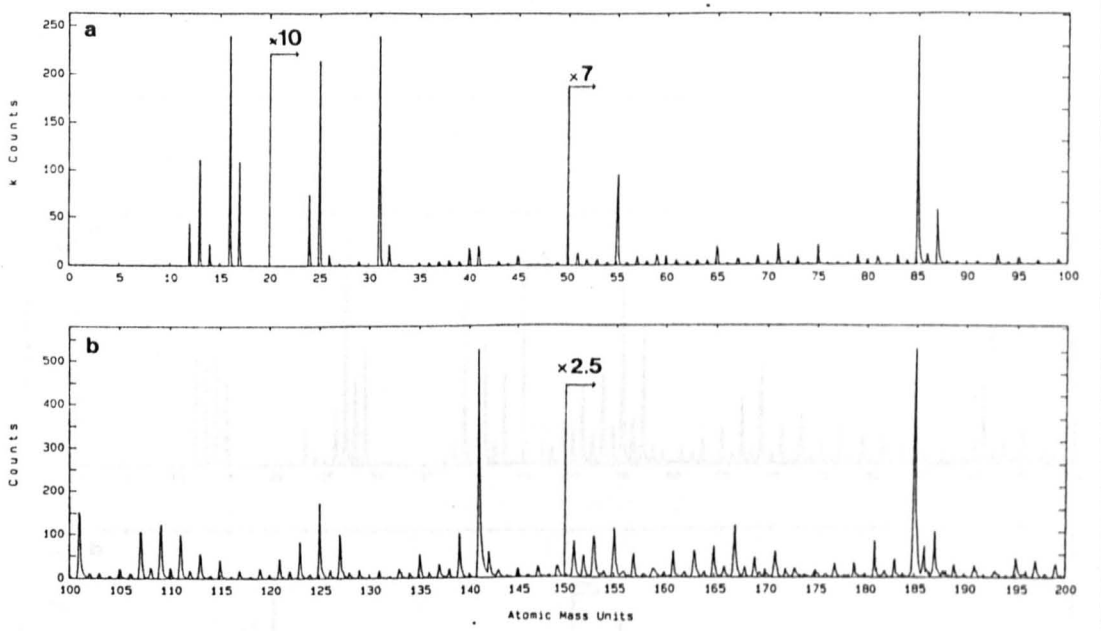

Figure 5.5: ToFSIM negative ion spectra for solution cast PMMA; (a) 0-100amu, (b) 100-200amu

5.3.1.2 Discussion

There are no stark differences between these spectra and those previously reported in the literature [30]. The peaks of interest with respect to the ion dose results shown in section 5.5, are m/z=41$^+$ ($C_3H_5^+$), 59$^+$ (CH_3O-C≡O^+), 69$^+$ ($CH_2C.CH_3.C{\equiv}O^+$), 77$^+$ ($C_6H_5^+$), 91$^+$ ($C_7H_7^+$), 101$^+$ ($(CH_3)_2C^+C.{=}O.OCH_3$) for the positive ions, and m/z=13$^-$ (CH^-), 16$^-$ (O^-), 31$^-$ (CH_3O^-), 55$^-$ ($CH_2{=}CH{=}CO^-$) and 85$^-$ ($CH_2{=}C.CH_3.COO^-$) for the negative ions.

5.3.2 ToFSIM spectra for PVC

5.3.2.1 Results

The ToFSIM spectra for PVC are shown in figure 5.6. Here the positive ion spectrum up to 200amu is shown, but only information up to 100amu is shown for the negative ion spectrum. Above this value, structures were detected but the spectrum was very noisy.

5.3.2.2 Discussion

PVC SIM spectra have been reported [30]. The positive spectrum shown in figure 5.6(a,b) differ little from the reported spectrum, the peaks being due to hydrocarbon clusters, similar to those found in the SIM spectrum of polyethylene. Some spectral features of the negative ion spectrum are presented here which have not been previously

reported. Examples include the peaks at m/z=47⁻ and 49⁻ which are due to carbon bonded to chlorine. The relative intensities of these two peaks are in the same isotopic ratio as that of the two chlorine peaks at m/z=35⁻ and 37⁻. The peaks at m/z=59⁻ and 61⁻ are due to C_2Cl^-.

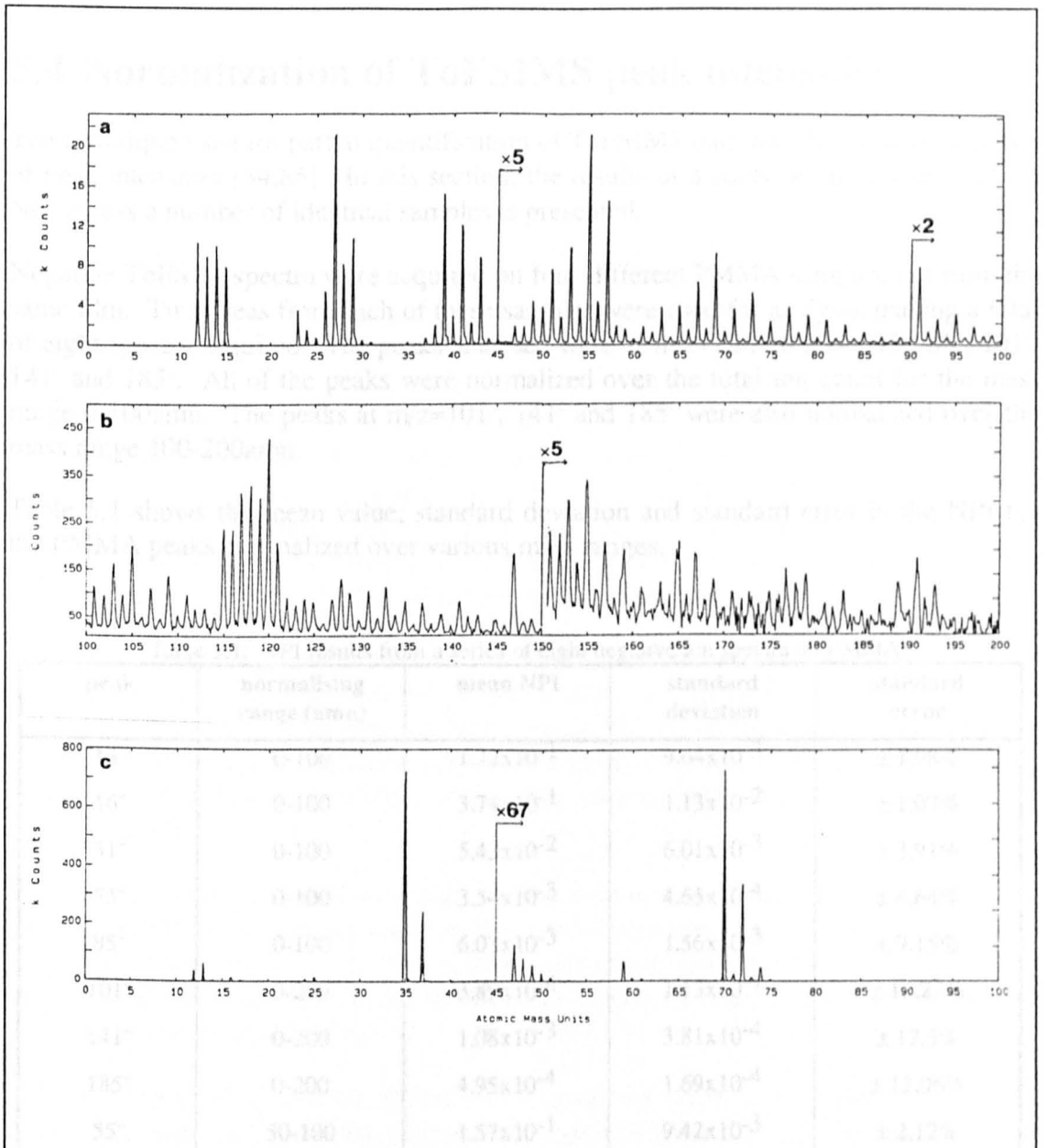

Figure 5.6: ToFSIM spectra for solution cast PVC; (a) positive ion spectrum, 0-100amu, (b) positive ion spectrum, 100-200amu, (c) negative ion spectrum, 0-100amu

The Cl_2^- peak has been previously reported. In this case the spectrum was taken with a quadrupole mass analyser. An indication of the increased resolution available to a ToFSIMS instrument is shown in figure 5.6(c) by the series of previously unreported peaks detected at m/z=70⁻ 72⁻ and 74⁻ which are all due to Cl_2^-. The relative intensities of the three peaks are in the same proportion as the isotopic probabilities of obtaining a ^{35}Cl-^{35}Cl ion, a ^{35}Cl-^{37}Cl ion and a ^{37}Cl-^{37}Cl ion.

The peaks of interest with respect to the ion dose experiment results are, for the positive ions, m/z=41$^+$, 77$^+$ and 91$^+$, and for the negative ions, m/z=13$^-$, 35$^-$ and 70$^-$.

5.4 Normalization of ToFSIMS peak intensities

The technique used for partial quantification of ToFSIMS data was that of normalization of peak intensities [84,85]. In this section, the results of a study on the variance of the NPI across a number of identical samples is presented.

Negative ToFSIM spectra were acquired on four different PMMA samples, cut from the same film. Two areas from each of these samples were used for analysis, making a total of eight spectra acquired. The peaks analysed were at m/z=13$^-$, 16$^-$, 31$^-$, 55$^-$, 85$^-$, 101$^-$, 141$^-$ and 185$^-$. All of the peaks were normalized over the total ion count for the mass range 0-100amu. The peaks at m/z=101$^-$, 141$^-$ and 185$^-$ were also normalized over the mass range 100-200amu.

Table 5.1 shows the mean value, standard deviation and standard error in the NPI for the PMMA peaks, normalized over various mass ranges.

Table 5.1: NPI results from a series of eight negative ion spectra on PMMA

peak	normalising range (amu)	mean NPI	standard deviation	standard error
13$^-$	0-100	1.72×10^{-1}	9.64×10^{-3}	± 1.98%
16$^-$	0-100	3.74×10^{-1}	1.13×10^{-2}	± 1.07%
31$^-$	0-100	5.43×10^{-2}	6.01×10^{-3}	± 3.91%
55$^-$	0-100	3.54×10^{-3}	4.65×10^{-4}	± 4.64%
85$^-$	0-100	6.03×10^{-3}	1.56×10^{-3}	± 9.15%
101$^-$	0-200	3.89×10^{-4}	1.13×10^{-4}	± 10.22%
141$^-$	0-200	1.08×10^{-3}	3.81×10^{-4}	± 12.5%
185$^-$	0-200	4.95×10^{-4}	1.69×10^{-4}	± 12.06%
55$^-$	50-100	1.57×10^{-1}	9.42×10^{-3}	± 2.12%
85$^-$	50-100	2.62×10^{-1}	3.15×10^{-2}	± 4.25%
101$^-$	100-200	4.41×10^{-2}	6.02×10^{-3}	± 4.83%
141$^-$	100-200	1.19×10^{-1}	2.26×10^{-2}	± 6.71%
185$^-$	100-200	5.53×10^{-2}	1.18×10^{-2}	± 7.54%

5.4.2 Discussion

The NPI's for the 13$^-$ and the 16$^-$ peaks (due to a quasi-elemental and an elemental ion respectively) had standard errors of within ±2%. All other normalized peaks were due

to molecular ions. For the 0-100amu normalizing range, the NPI's of molecular ion peaks ranged in standard error from ±3.91% to ±9.15%. These are much larger errors than those found for the elemental and quasi-elemental ions. For the three peaks above m/z=100$^-$, the normalizing range was increased to 0-200amu. As can be seen from table 5.1, the NPI standard errors for these peaks ranged from ±10.22% to ±12.5%. One of the reasons for the disparity in NPI standard errors between elementals and molecular ions is the very large relative intensities of the former. The oxygen ion on average comprised over a third of the total ion count from 0-100amu. Small fluctuations in the intensity of the elemental ion consequently varied the 0-100amu normalising range. When peaks which had much lower intensities were normalised over the mass range which included the elemental ion, the resulting standard error increased, and the greater the difference in mean NPI between the molecular ion and the elemental, the greater the standard error. For this reason, when using this method to partially quantify ToFSIM spectra, it is imperative that an appropriate normalizing range is used in order to minimise standard errors. This will shortly be discussed further. First a comment should be made regarding the standard error in the 85$^-$ peak, normalized over the range 0-100amu. This is ±9.15% as compared to ±4.64% for the 55$^-$ peak. The larger error in the 85$^-$ peak is not ascribed to the difference in NPI between the 85$^-$ and 16$^-$, as the mean NPI for the 85- ion was greater than for the 55$^-$ (which had a smaller error). The reason for the larger error is the susceptibility of the 85$^-$ ion to sample charging. In all ToFSIMS experiments on PMMA, it was found that if the charge neutralisation was not correctly controlled, the 85$^-$ ion had an unpredictable intensity in relation to the 55$^-$ ion.

The normalizing range for studies of this kind is chosen arbitrarily. An *appropriate* normalizing range is now defined as one which: (1) contains the spectral peak of interest, (2) contains a number of other peaks, (3) does not contain peaks due to contaminants (unless of negligible intensity), and (4) does not contain peaks that have normalised peak intensities more than an order of magnitude greater than the spectral peak of interest.

From the 31$^-$ peak data shown in table 5.1 it is seen that, with respect to this definition, the mass range 0-100amu is an appropriate normalizing range, as the most intense peak at 16$^-$ has an NPI less than an order of magnitude greater than that for 31$^-$. For all other peaks, the 0-100amu or 0-200amu normalizing ranges are inappropriate as they lead to large experimental standard errors.

For the 55$^-$ and 85$^-$ peaks, an appropriate normalizing range is 50-100amu. From the table it is seen that this range produced standard errors of ±2.12% and ±4.25% respectively. The appropriate normalizing range for peaks above m/z=100$^-$ was considered to be 100-200amu. This gave errors of between ±4.83% and ±7.54%. This was much larger than expected. A probable reason for this is that at the time the experiments were performed, difficulties were being experienced in controlling the signal to noise ratio at masses above 100amu. It is expected that when signal to noise ratios are reduced to a minimum, the higher mass normalizing range would give reduced standard errors.

Ignoring the results for the peaks above m/z=100$^-$, this study has indicated that for elemental and quasi-elemental ions, standard errors in ToFSIMS NPI's can be less than ±

2%. For molecular ions, standard errors within ±5% can be expected, providing an appropriate normalizing range is chosen.

O'Toole *et al* [85] using the same instrument as in the present study, observed a data error in NPI of ±8% for the positive ion spectra of solution cast polystyrene, using a normalizing range of 0-100amu. Experiments performed in a separate study [99] using the same instrument, showed that for that for poly(ether ether ketone) (PEEK), the NPI error could be as little as ±4%. In both studies, these errors were calculated on the basis of a difference in NPI's for two spectra, *i.e.* two spectra were obtained from one sample, each from different areas, and the NPI's for spectral peaks of interest were compared. The error was determined as the percentage scatter of the two values from the mean. In the present study, because eight spectra from different areas were compared, a higher confidence level is achieved.

Only negative ToFSIM spectra were considered here. This was because the negative ion spectrum was the only type that could be used for direct, unambiguous comparisons of PVC and PMMA features in ToFSIM spectra of PVC/PMMA blends. This point will be discussed further in chapter six. For positive ion spectra it is predicted that the standard errors in NPI would be much less than those in the two studies just described. It is possible that these errors could be as little as for elemental and quasi-elemental ions in the negative ion spectra *i.e.* within ±2%, because positive ion spectra for organic polymers (providing the surface is not contaminated) in general consist mainly of hydrocarbon molecular information rather than the elementals.

From past studies using the Sheffield ToFSIMS instrument, and from results of the present study shown later in this chapter and in chapter 6, the technique of normalization of peak intensities has been shown to be an adequate method for partial quantification of ToFSIM spectra. It does however have at least one limitation. For the comparison of spectra containing elemental information, which have been acquired from *different samples* or *different areas of the same sample*, molecular information can be subject to large experimental errors. In order to reduce these errors as much as possible, an appropriate normalizing range must be used.

In the next section it is shown that for comparison of elemental containing spectra, acquired consecutively from *one area of the same sample*, the experimental errors for molecular NPI's are reduced, when normalized over a mass range which includes elementals.

5.5 ToFSIMS ion dose studies

5.5.1 Normalised peak intensity - ion dose profiles

This section is intended as a guide to the interpretation of the remainder of the results in this chapter. The ToFSIMS ion dose study results are presented in the form of

normalized peak intensities (NPI's) of ions of interest, plotted against the primary ion dose received by the sample, in the range $2x10^{10}$ - $2x10^{14}$ ions cm^{-2}. The resulting plots are called NPI-ion dose profiles. All the ions examined were normalized over the total ion count for the mass range 0-100amu.

The trends observed in these plots should ideally be continuous. However, discontinuities or "steps" were observed. These were of two types: steps due to changes in magnification, and steps due to changes in detector voltage. One of the NPI-ion dose profiles displayed both of these steps quite prominently, and this example is shown in figure 5.7, the NPI-ion dose profile for the PVC $^{35}Cl^-$ ion. This profile will be redisplayed and its features discussed in section 5.5.3. In the present context, only the discontinuities are of interest.

5.5.1.1 Magnification steps

The data in figure 5.7 followed a smooth, continuous trend, from the lowest ion dose up to $3x10^{13}$ ions cm^{-2}. At this point the magnification was increased from 500x to 1000x in order to facilitate the change in ion dose regime. The effect of this magnification increase was to cause a step in the profile to higher NPI. Such steps were not always observed. For ions with mass less than 50amu, if a step occurred it would usually be to higher NPI. For higher mass ions, the step would be to lower NPI. This suggests that the surface potential can change with an increase in magnification such that lower mass ions are favoured in terms of detection sensitivity.

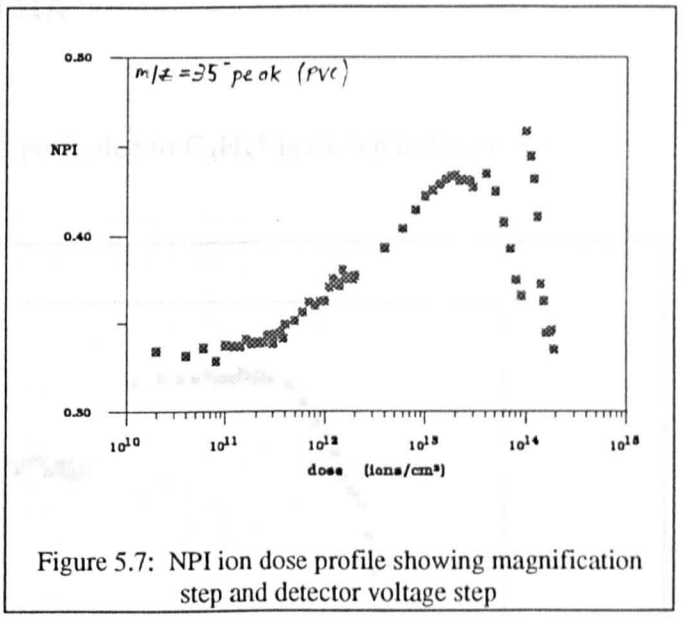

Figure 5.7: NPI ion dose profile showing magnification step and detector voltage step

5.5.1.2 Detector voltage steps

It was observed with the Sheffield ToFSIMS instrument that when a large number of experiments were run continuously, at a certain non-predictable point, the voltage on the detector would "drift" such that the signal intensity dropped dramatically. This was not a gradual process, *i.e.* the intensities of previous spectra did not suffer prior to this event. As soon as the detector voltage drifted, it had to be readjusted to allow spectra to be acquired. The effect of this is shown in figure 5.7 at just beyond 10^{14} ions cm^{-2}. Prior to this point, the profile was continuous (following the magnification step). The change in detector voltage caused a step in the profile to much higher NPI. Again, the steps were not observed for every ion and were not always to higher NPI. A probable reason for such a step is that changing the detector voltage changes the relative detection sensitivity of certain ions.

5.5.1.3 Errors

No error bars have been included in the data points for the NPI-ion dose profiles. This is because error bars in the x and y directions on such a large amount of data points, in addition to the steps, would cause confusion in the observation of trends.

The error in NPI for both positive and negative ion spectra, for elemental and molecular information, does not appear to be as large as suggested in section 5.4. This is probably due to all the spectra in a profile series being acquired continuously on the same sample, resulting in a more consistent charge neutralisation. The NPI error is estimated at being within the ±8% predicted by O'Toole *et al* [85], for all ions in both the negative and positive ion spectra.

The error in logarithm (base 10) of the primary ion dose has been independently determined by Denison [100], to be within ±1.2%.

5.5.2 Ion dose studies on PMMA

5.5.2.1 Results

The NPI-ion dose profile for the 41^+ peak, due to $C_3H_5^+$ is shown in figure 5.8.

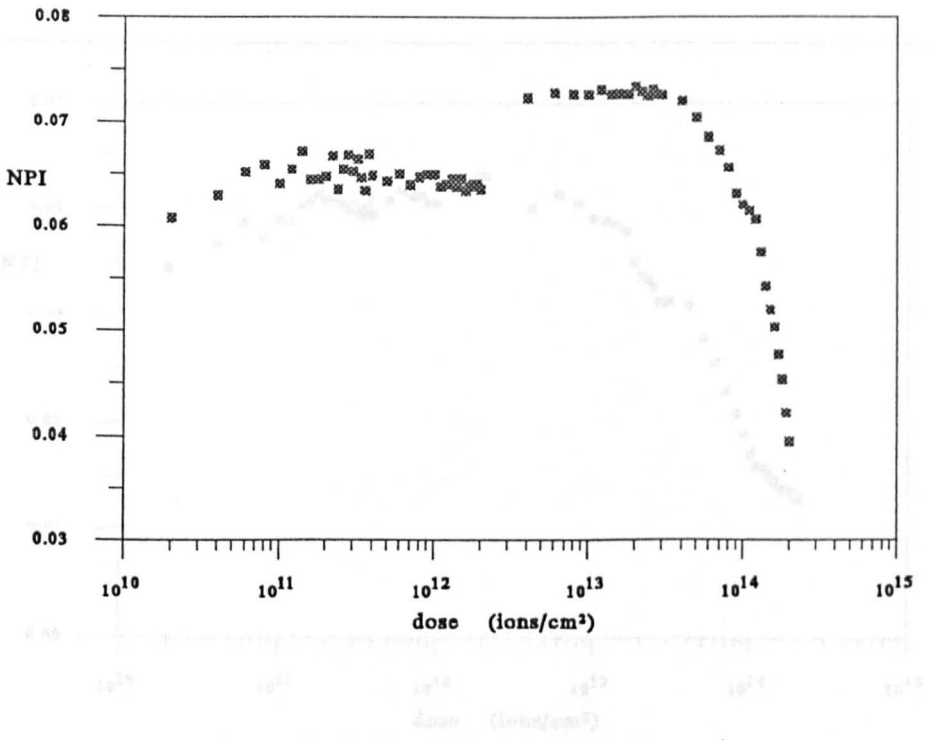

Figure 5.8: NPI-ion dose profile for PMMA 41^+ peak

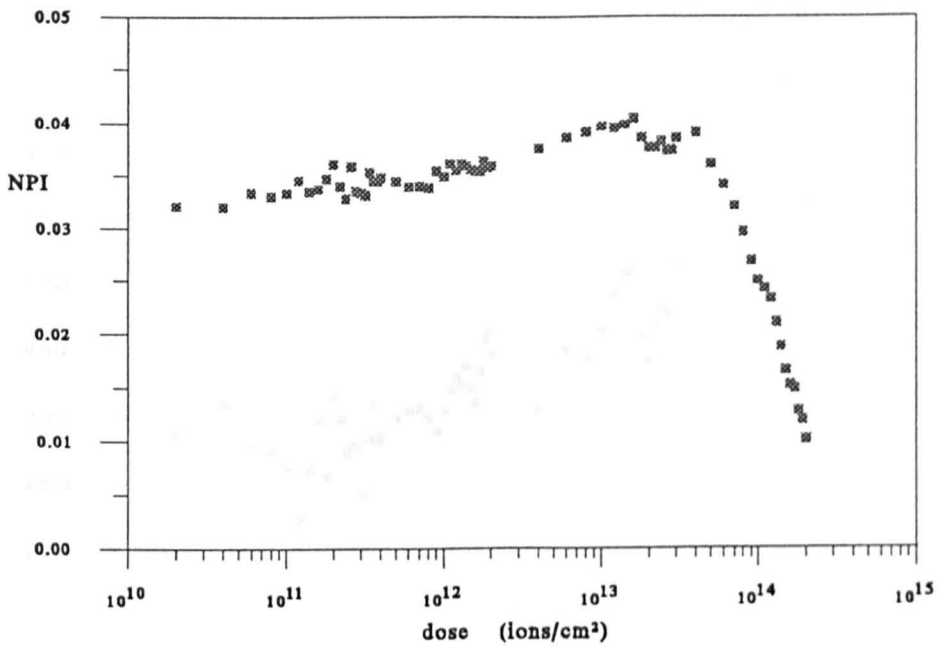

Figure 5.9: NPI-ion dose profile for PMMA 59^+ peak

The NPI-ion dose profiles for the m/z=59^+ peak ($CH_3OC{\equiv}O^+$) and m/z=69^+ ($CH_2C.CH_3.C{\equiv}O^+$) peak are shown in figures 5.9 and 5.10 respectively.

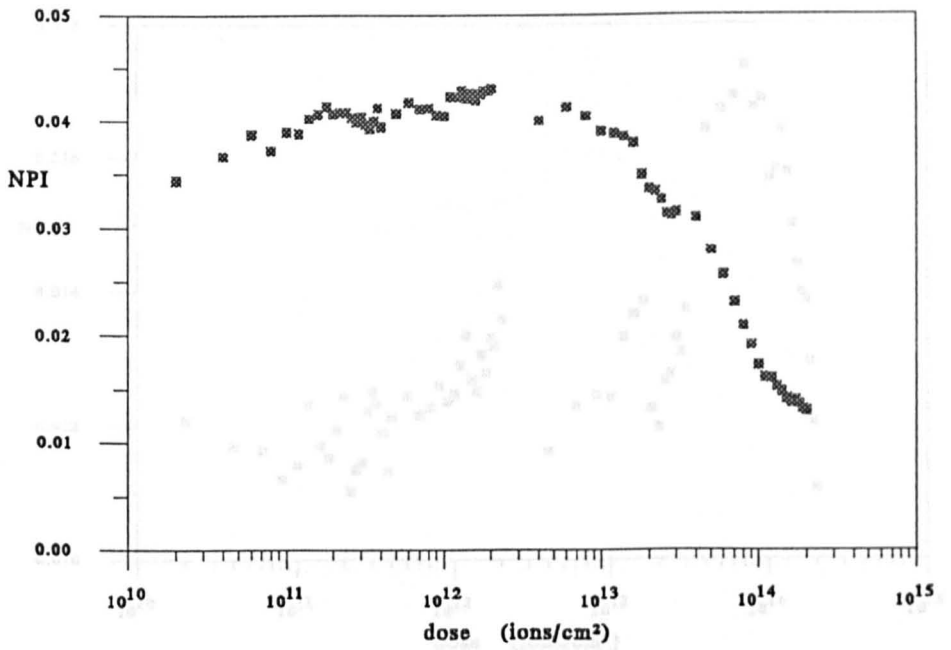

Figure 5.10: NPI-ion dose profile for PMMA 69^+ peak

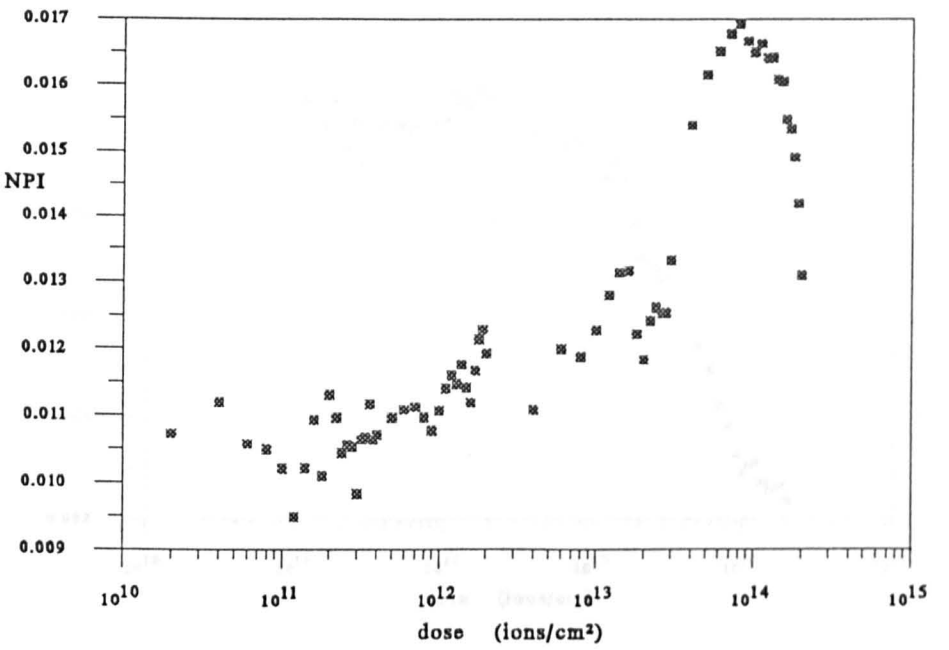

Figure 5.11: NPI-ion dose profile for PMMA 77^+ peak

Figure 5.11 and 5.12 show the NPI ion dose profiles for the m/z=77^+ and m/z=91^+. These peaks are due to $C_6H_5^+$ and $C_7H_7^+$ respectively.

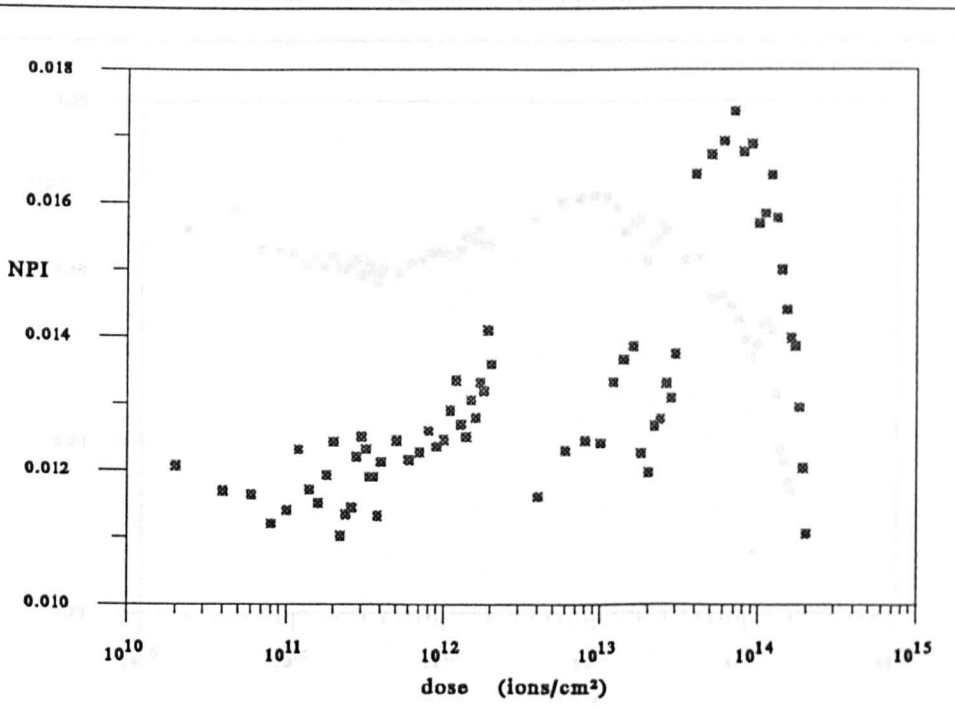

Figure 5.12: NPI-ion dose profile for PMMA 91^+ peak

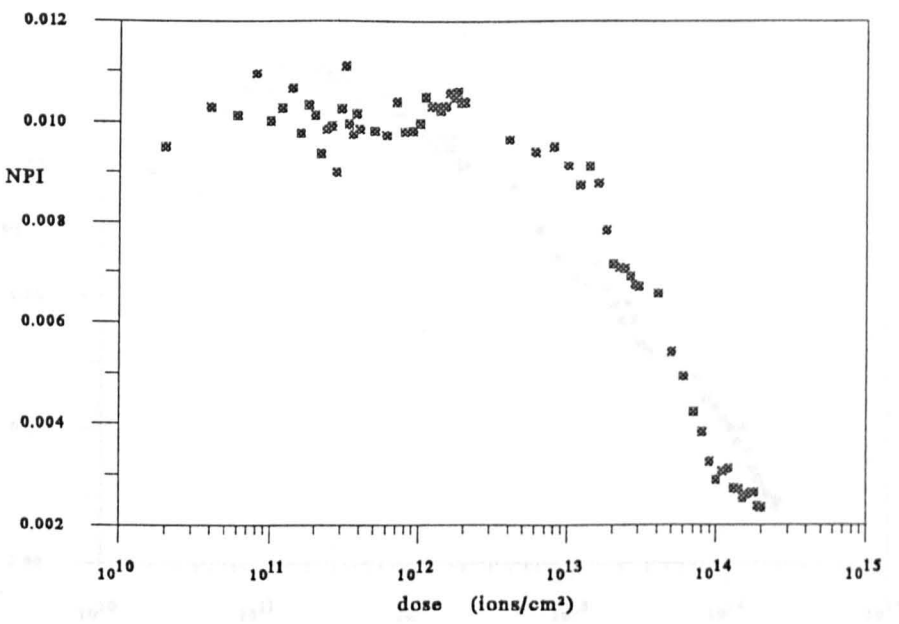

Figure 5.13: NPI-ion dose profile for PMMA 101^+ peak

The NPI-ion dose profiles for the m/z=101+ ($(CH_3)_2C^+C.O.OCH_3$) peak is shown in figure 5.13. This is the last profile from the PMMA positive ion spectrum that is displayed.

The NPI-ion dose profile for the PMMA 16^- (O^-) peak is shown in figure 5.14.

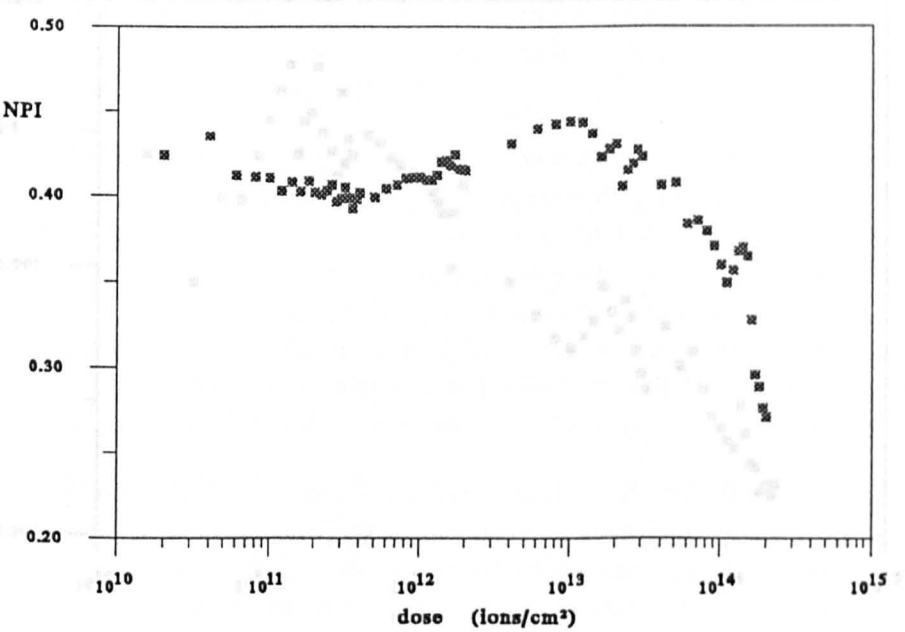

Figure 5.14: NPI-ion dose profile for PMMA 16^- peak

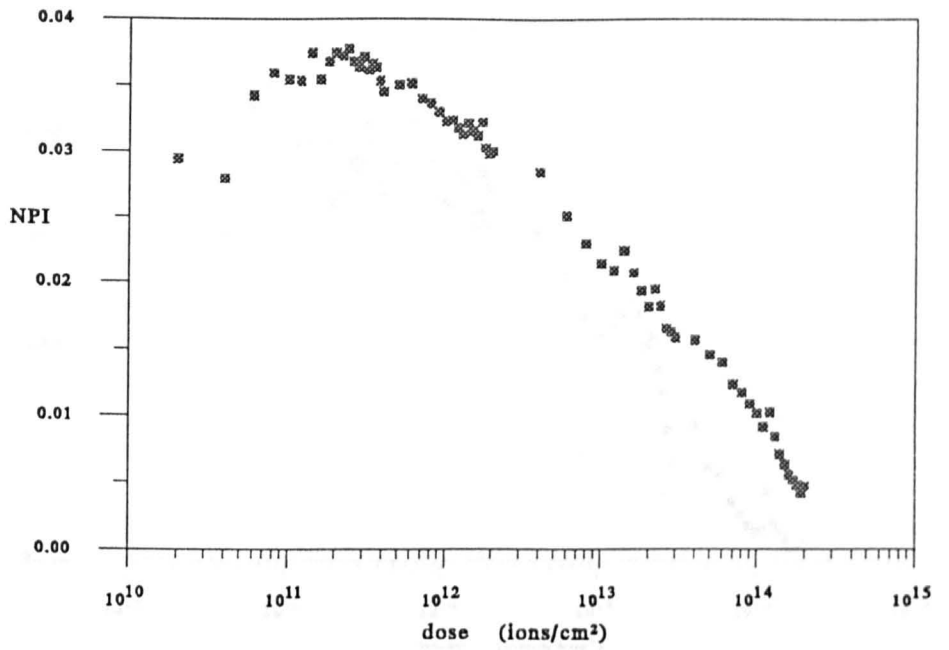

Figure 5.15: NPI-ion dose profile for PMMA 31^- peak

The NPI-ion dose profile for the m/z=31^- (CH_3O^-) peak is shown in figure 5.15. That for the m/z=55^- (CH2=CH-CO^-) peak is shown in figure 5.16.

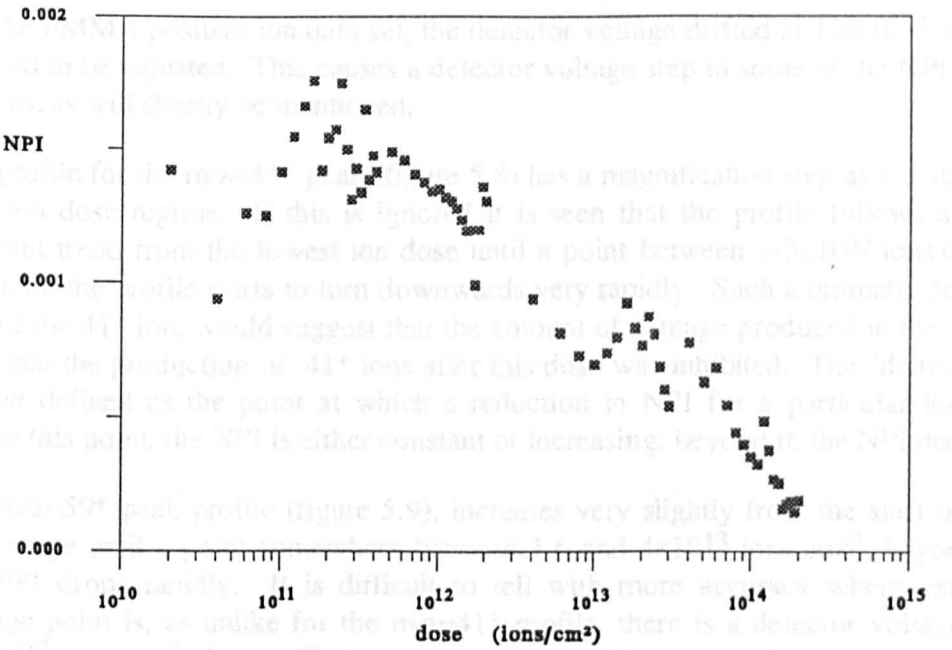

Figure 5.16: NPI-ion dose profile of PMMA 55^- peak

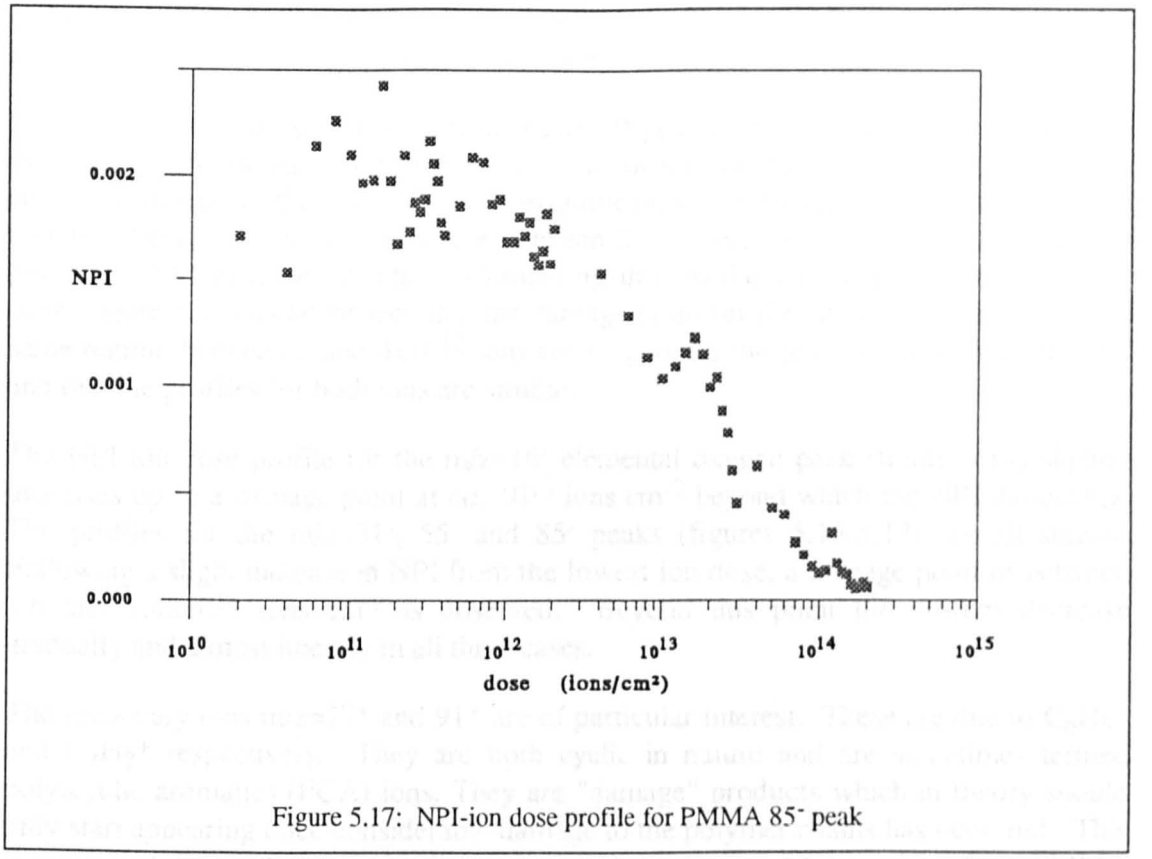

Figure 5.17: NPI-ion dose profile for PMMA 85⁻ peak

Finally, the NPI-ion dose profile for the m/z=85⁻ (CH_2=C.CH_3.COO^-) peak is shown in figure 5.17.

5.5.2.2 Discussion

For the PMMA positive ion data set, the detector voltage drifted at $1.6x10^{13}$ ions cm^{-2}, and had to be adjusted. This causes a detector voltage step in some of the NPI-ion dose profiles, as will shortly be mentioned.

The profile for the m/z=41^+ peak (figure 5.8) has a magnification step at the start of the high ion dose regime. If this is ignored it is seen that the profile follows a smooth, constant trend from the lowest ion dose until a point between $2\text{-}3x10^{13}$ ions cm^{-2}. At this point the profile starts to turn downwards very rapidly. Such a dramatic drop in the NPI of the 41^+ ion, would suggest that the amount of damage produced in the surface is such that the production of 41^+ ions after this dose was inhibited. The "damage point" is now defined as the point at which a reduction in NPI for a particular ion begins. Below this point, the NPI is either constant or increasing; beyond it, the NPI decreases.

The m/z=59^+ peak profile (figure 5.9), increases very slightly from the start of the ion dose range until a point somewhere between 1.6 and $4x10^{13}$ ions cm^{-2}, beyond which the NPI drops rapidly. It is difficult to tell with more accuracy where exactly the damage point is, as unlike for the m/z=41^+ profile, there is a detector voltage step at $1.6x10^{13}$ ions cm^{-2} (this profile however does not suffer a magnification step at the start of the high dose regime). Despite the uncertainty in determining this point, the corresponding point for the 41^+ profile falls within the damage point range of the 59+ peak. The NPI-dose profiles for these two ions are therefore quite similar. The 59+ ion

is the most likely indicator of PMMA side chains. Therefore the damage point in this case indicates that most of the side chains at this point had been sputtered.

Dissimilar behaviour is observed for the m/z=69$^+$ peak profile (figure 5.10). For this ion there is a slight increase in NPI from the start of the ion dose range until 2x10^{12} ions cm^{-2}. At this point there is possibly a magnification step to lower NPI, but it appears that the damage point is somewhere between 2 and 4x10^{12} ions cm^{-2} as beyond this point, the NPI deceases steadily. Comparing this profile with that for the m/z=101$^+$ peak (figure 5.13) it can be seen that the damage point for the latter profile occurs in the same region, between 2 and 4x10^{12} ions cm^{-2}, ignoring the possible magnification step, and that the profiles for both ions are similar.

The NPI-ion dose profile for the m/z=16$^-$ elemental oxygen peak (figure 5.14) slightly increases up to a damage point at *ca.* 10^{13} ions cm^{-2} beyond which the NPI diminishes. The profiles for the m/z=31$^-$, 55$^-$ and 85$^-$ peaks (figures 5.15-5.17) are all similar. Following a slight increase in NPI from the lowest ion dose, a damage point of between 1.6 and 2.4x10^{11} ions cm^{-2} is observed. Beyond this point the profiles decrease gradually and almost linearly in all three cases.

The secondary ions m/z=77$^+$ and 91$^+$ are of particular interest. These are due to $C_6H_5^+$ and $C_7H_7^+$ respectively. They are both cyclic in nature and are sometimes termed poly(cyclic aromatic) (PCA) ions. They are "damage" products which in theory should only start appearing once considerable damage to the polymer chains has occurred. This is apparent by considering that neither ion contains oxygen, and a structure from PMMA that contains at least 6 carbon atoms could only be formed after the loss of at least two oxygen containing side groups.

Figures 5.11 and 5.12 show that the production of these ions are in evidence from a very early stage. This is in agreement with observations made by Leggett and Vickerman [97] from ion dose studies on PVC. At the lowest dose used in these experiments, 2x10^{10} ions cm^{-2}, both ions are present albeit in small concentrations. The two ions have a very similar NPI-ion dose profile, both of which are affected by magnification and detector voltage steps in the ion dose region between 2x10^{12} and 3x10^{13} ions cm^{-2}. If these are smoothed out, both ions have a profile of the shape shown in figure 5.18. Both ions start off at fairly constant normalised peak intensities, but start to increase at *ca.* 5x10^{11} ions cm-2. This increase in NPI continues until a maximum is reached at *ca.* 7x10^{13} ions cm^{-2}. Beyond this point, the NPI decreases rapidly. This information suggests, as expected, that as the ion dose increases, the intensity of the 91$^+$ and 77$^+$ ions increase because the

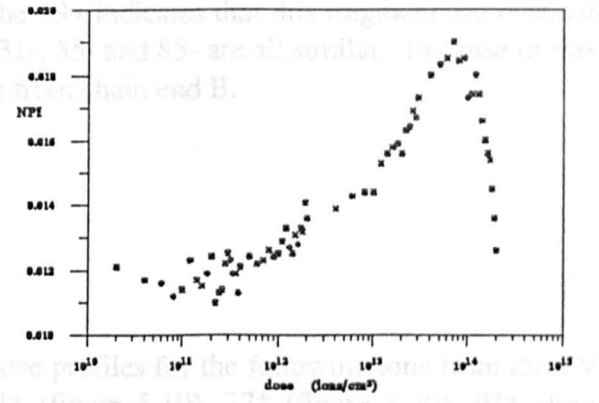

Figure 5.18: Smoothed NPI-ion dose profile for PCA ion

polymer surface is becoming increasingly damaged. This increase in intensity, which becomes gradually more pronounced as the intensities of PMMA ions decrease beyond their damage point, continues until at a certain maximum point, the surface becomes damaged to such an extent that formation of the PCA ions becomes more difficult. Beyond the damage point at $7x10^{13}$ ions cm^{-2}, there is a sharp decrease in the number of PCA ions generated, suggesting that there is not enough hydrogenated carbon to form PCA ions with the same intensity. As the drop in NPI of these ions is so sharp, it is proposed that beyond the PCA ion damage point, the surface starts to graphitize, *i.e.* beyond an ion dose of $2x10^{14}$ ions cm^{-2}, the surface structure of PMMA resembles that of graphite. One difficulty with this interpretation is that figure 5.14 shows that at $2x10^{14}$ ions cm^{-2}, the oxygen ion at $m/z=16^-$ still comprises more than a quarter of the total ion count of the negative spectrum between 0-100amu. Although ToFSIMS is a technique which probes the outermost surface monolayer, a possible reason for the large amount of oxygen at the highest ion dose, given the apparent graphitization of the surface, is that ToFSIMS might also detect elemental ions which originate from *below* the outer surface monolayer. This possibility is further examined in chapter six.

From these results, it is proposed that the damage point is the limit of the static SIMS regime, *i.e.* the primary ion dose point for a particular secondary ion at which damage to the surface inhibits its generation. From the results presented thus far, an implication of this proposal is that the limit of the static regime is not at a fixed point. Instead, the limit is dependent on the specific ion being observed, and varies for different secondary ions.

It is further proposed that the fragmentation route of secondary ions with similar NPI-ion dose profiles can be related. The similarity in profiles between the 77^+ and 91^+ have already been discussed. There is also a similarity between the 41^+, 59^+ and the 16^- profiles, *i.e.* they all reach their damage points at approximately the same time. Lub and Benninghoven's PMMA fragmentation scheme [96] shown in figure 3.16 (page 55), proposed loss of the side group (the most likely source of 59^+) followed by chain scission and the formation of two new end groups A and B. It is not surprising that the 16^- and the 59^+ profiles are similar, because a loss of oxygen would be expected when oxygen containing side chains are being lost. The similarity of the 41^+ to the 59^+, however, indicates that the most likely event after chain scission for chain end A is loss of the 41^+ fragment. The 101+ ion is also likely to be sputtered from chain end A. The similarity of this ions profile to that of the 69+ indicates that this fragment too originates from chain end A. The profiles for the 31-, 55- and 85- are all similar. Because of this it is very likely that all three ions originate from chain end B.

5.5.3 Ion dose studies on PVC

5.5.3.1 Results

Over the next few pages, the NPI-ion dose profiles for the following ions from the PVC ion dose study are presented: $m/z=41^+$ (figure 5.19), 77^+ (figure 5.20), 91^+ (figure 5.21), 35^- (figure 5.22) and 70^- (figure 5.23).

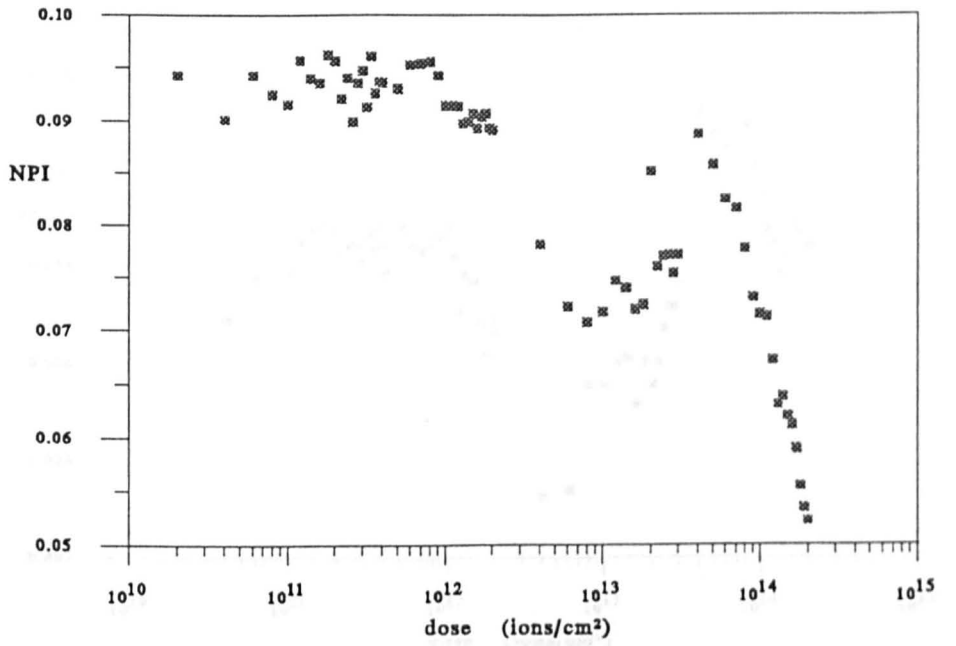

Figure 5.19: NPI-ion dose profile for PVC 41^{+} peak

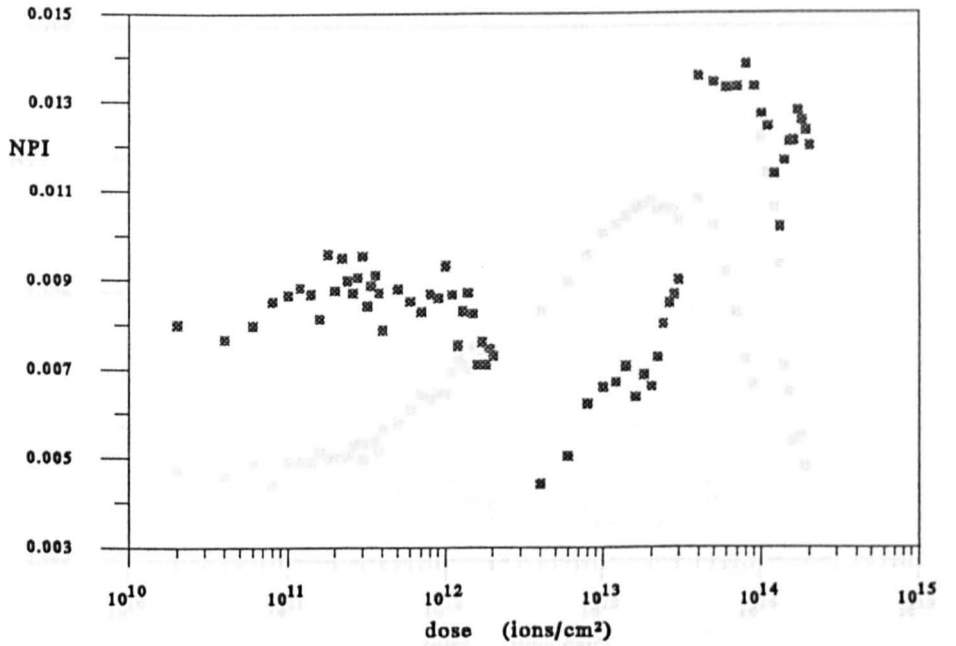

Figure 5.20: NPI-ion dose profile for PVC 77^{+} peak

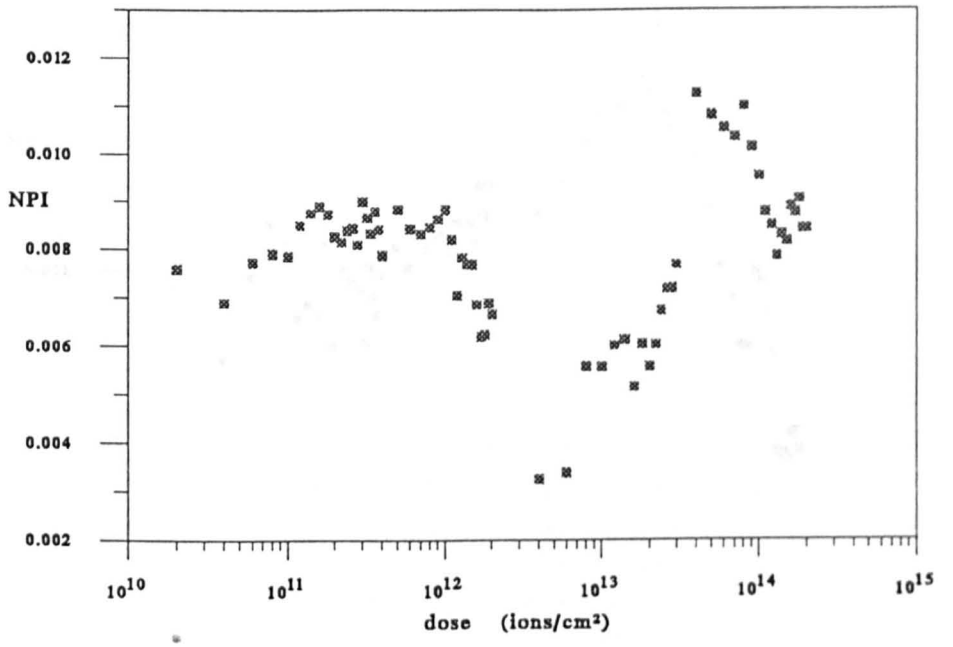

Figure 5.21: NPI-ion dose profile for PVC 91^{+} peak

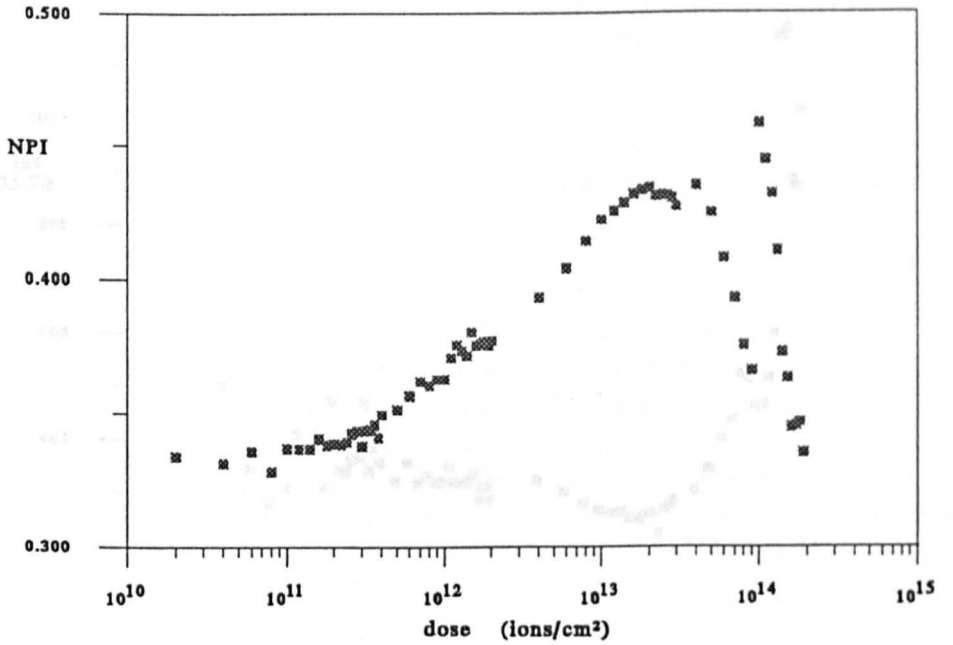

Figure 5.22: NPI-ion dose profile for PVC 35^{-} peak

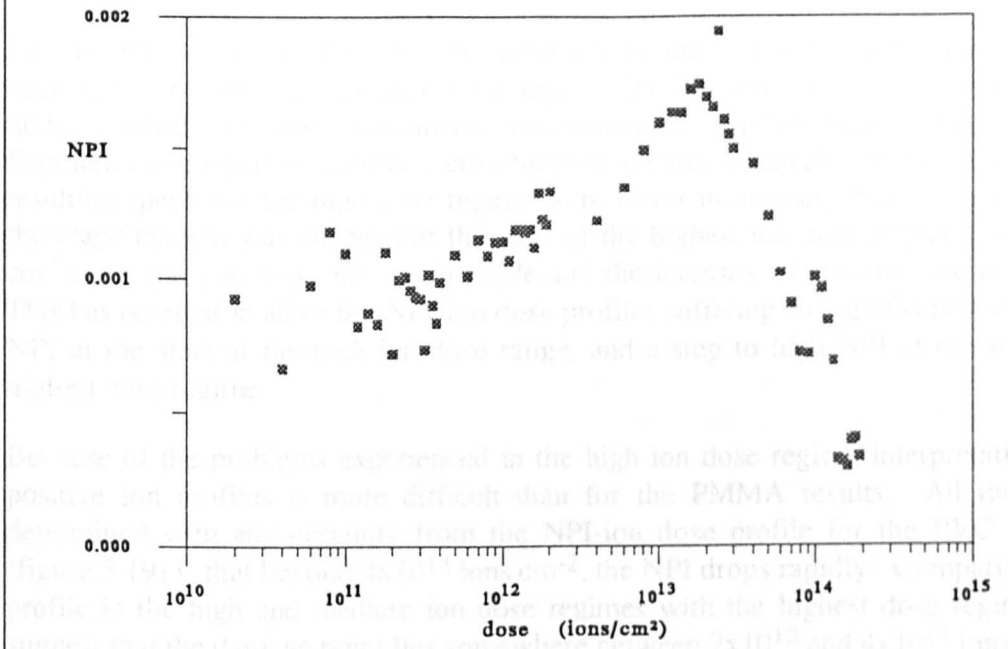

Figure 5.23: NPI-ion dose profile for PVC 70^- peak

Finally, in figure 5.24, the relative intensity of the 35^- to the 70^- ion is plotted as a function of ion dose.

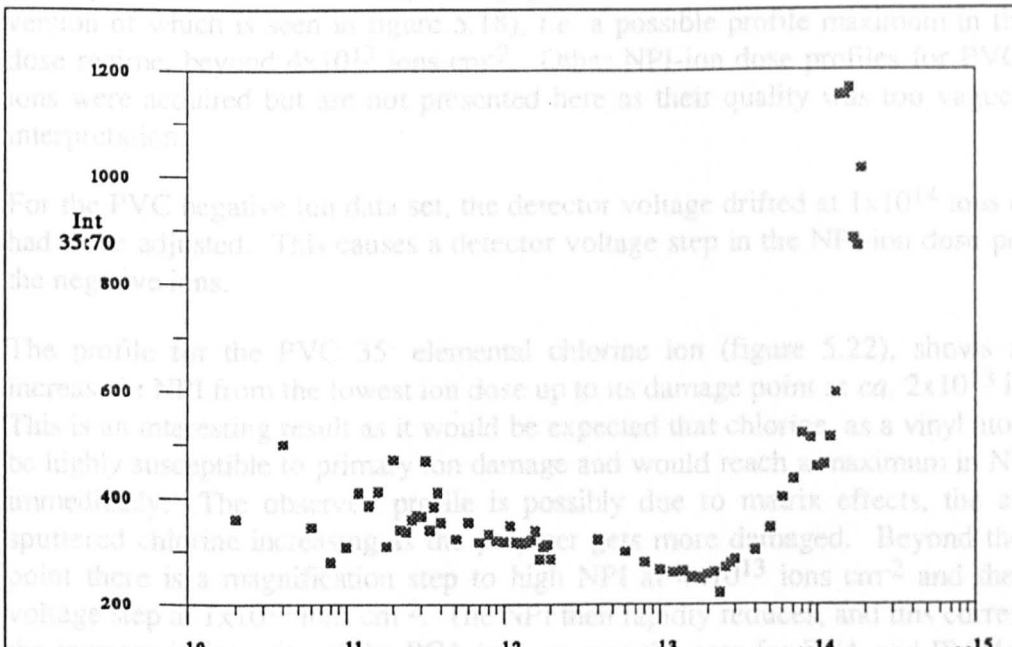

Figure 5.24: Effect of primary ion dose on the relative intensity of the 35^-:70^- ions

5.5.3.2 Discussion

For the PVC positive ion data set, instability in the ToFSIMS liquid metal ion gun occurred at the start of the high dose regime ($2x10^{12}$ ions cm^{-2}). This was brought under control and the experiments recommenced (though very slight, occasional fluctuations in ion gun stability were observed for the remainder of this regime). The resulting spectra in the high dose regime were lower in intensity than expected. When the magnification was changed at the start of the highest ion dose regime ($3x10^{13}$ ions cm^{-2}), the ion gun was once again stable and the intensity of spectra was as expected. This has resulted in all of the NPI-ion dose profiles suffering a magnification step to low NPI at the start of the high ion dose range, and a step to high NPI at the start of the highest dose regime.

Because of the problems experienced in the high ion dose region, interpretation of the positive ion profiles is more difficult than for the PMMA results. All that can be determined with any certainty from the NPI-ion dose profile for the PVC 41^+ peak (figure 5.19) is that beyond $4x10^{13}$ ions cm^{-2}, the NPI drops rapidly. Comparison of the profile in the high and medium ion dose regimes with the highest dose regime would suggest that the damage point lies somewhere between $2x10^{12}$ and $4x10^{13}$ ions cm^{-2}.

For the PVC PCA ions at m/z=77^+ (figure 5.20) and 91^+ (figure 5.21) the same interpretation problems are experienced because of the difficulties in the high ion dose regime. An additional problem for these ions is that, although present at very low ion doses, their intensity was much lower for PVC than for PMMA. It is not thought that this trend applies generally, rather it is a consequence of instrument problems during acquisition of this data set. What can be observed however is a broad similarity for these profiles with the corresponding profile for PMMA PCA ions (the smoothed version of which is seen in figure 5.18), *i.e.* a possible profile maximum in the highest dose regime, beyond $4x10^{13}$ ions cm^{-2}. Other NPI-ion dose profiles for PVC positive ions were acquired but are not presented here as their quality was too vague for valid interpretation.

For the PVC negative ion data set, the detector voltage drifted at $1x10^{14}$ ions cm^{-2}, and had to be adjusted. This causes a detector voltage step in the NPI-ion dose profiles for the negative ions.

The profile for the PVC 35^- elemental chlorine ion (figure 5.22), shows a gradual increase in NPI from the lowest ion dose up to its damage point at *ca.* $2x10^{13}$ ions cm^{-2}. This is an interesting result as it would be expected that chlorine, as a vinyl atom, would be highly susceptible to primary ion damage and would reach a maximum in NPI almost immediately. The observed profile is possibly due to matrix effects, the amount of sputtered chlorine increasing as the polymer gets more damaged. Beyond the damage point there is a magnification step to high NPI at $4x10^{13}$ ions cm^{-2} and the detector voltage step at $1x10^{14}$ ions cm^{-2}. The NPI then rapidly reduces, and this corresponds to the increase in intensity of the PCA ions, as was the case for PCA and PMMA-specific ions shown in the previous section.

The PVC m/z=70^- ion profile (figure 5.23) as expected shows approximately the same profile as that of the 35^- ion, although because of the low intensity of the 70^- ion, the profile is not as well resolved. The effect of primary ion dose on the intensity ratio of

35^-:70^- ions, displayed in figure 5.24, shows that beyond the chlorine damage point, the intensity of the 70^- ions drops with respect to that of the 35^- ions. To form Cl_2^-, the chlorine atoms in the surface must be in close proximity. Beyond the damage point, Cl_2^- ions cannot form with the same efficiency because damage to the surface results in the remaining chlorine atoms being too far apart to combine effectively. This is clearly reflected in figure 6.24.

5.5.4 A final comment on the NPI-ion dose profiles

It is recognised that the quality of some of the data presented in the NPI-ion dose profiles has been of a variable nature. It would have been desirable to repeat the 270 ToFSIMS experiments and subsequent data analysis that these results represent, however, these experiments were performed towards the end of the study and occupied a large proportion of instrument time. Time limitations precluded any repeat experiments. Despite this, the NPI-ion dose profile method has shown some very interesting trends, and will be of analytical value in future studies.

Having obtained a number of relevant results on homo-PVC and homo-PMMA, it is now possible to present results on surface studies of PVC/PMMA blends.

CHAPTER SIX - Surface Studies on Miscible Polymer Blends

6.1 Overview

In this chapter, the blends examined are all miscible across the composition range. They were produced by solution casting from butan-2-one. In all cases, the PVC used was Fluka Selectaphore and the PMMA was Polymer Laboratories secondary standard. Following a brief look at some bulk studies which confirm the miscibility of the blends, XPS and ToFSIMS data from these blends are presented and discussed.

6.2 Bulk studies

DSC thermographs and Raman spectra were acquired for both homopolymers and three intermediate blend compositions, at PVC:PMMA ratios of 70:30, 50:50 and 30:70. Henceforth, similar series of blends will be described as "PVC/PMMA blend compositions of 100/0, 70/30, 50/50, 30/70 and 0/100" where 100/0 indicates homo-PVC and 0/100 is homo-PMMA.

6.2.1 Results

Figure 6.1 shows the DSC thermographs for homo-PVC (a) and homo-PMMA (b). The direction of exotherm is upwards and the glass transition temperature is defined as the onset point of the transition region in the endothermic direction. For PMMA the T_g was determined to be 78°C, reproducible over several runs, and for PVC the reproducible T_g value was 61°C.

Figure 6.1(c) shows the Tg dependence for PVC/PMMA blends on the bulk composition.

The C=O stretching band for each composition as determined by Raman spectroscopy is shown in figure 6.2.

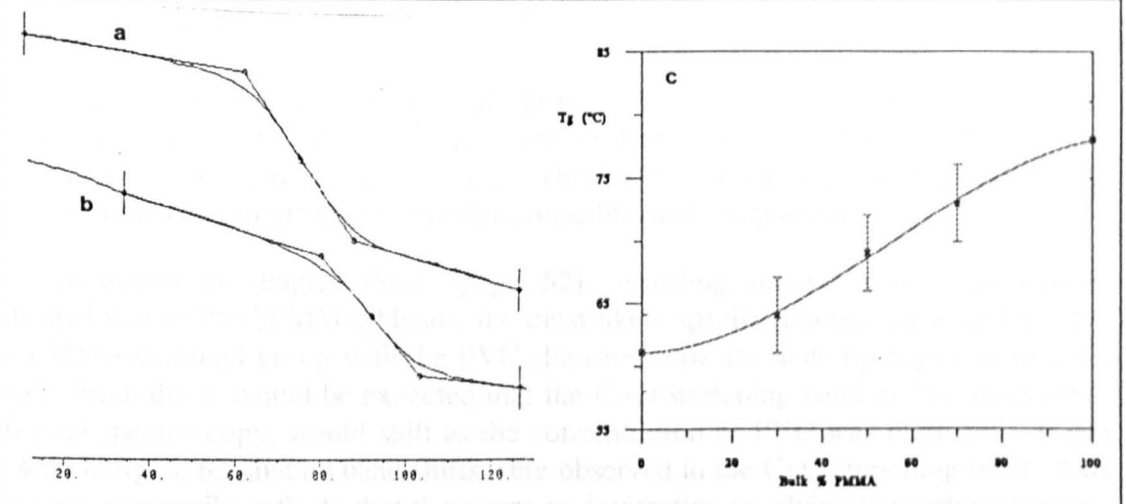

Figure 6.1: DSC studies on PVC/PMMA blends cast from butan-2-one; (a) thermogram of homo-PVC, (b) thermogram of homo-PMMA, and (c) Tg dependence on PVC/PMMA bulk composition

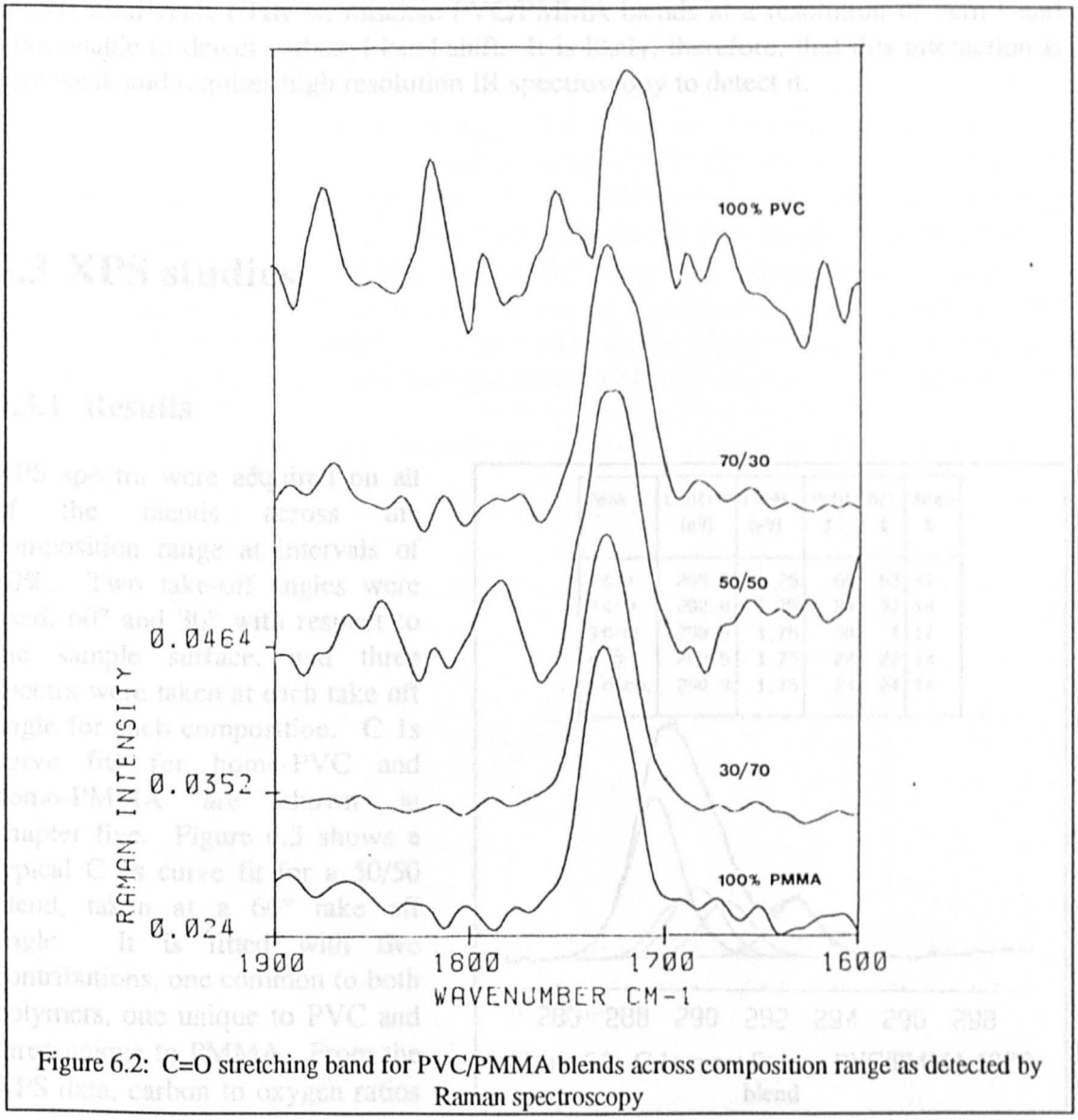

Figure 6.2: C=O stretching band for PVC/PMMA blends across composition range as detected by Raman spectroscopy

6.2.2 Discussion

All of the blends analysed had optical clarity. A single Tg was observed for each composition, and for the blends this lay in between the values of Tg for the homopolymers, as seen in figure 6.1(c). These observations indicate that the blends were homogeneous single phase materials, miscible in all proportions.

The discussion in chapter three (page 52) regarding intermolecular interactions, indicated that in PVC/PMMA blends, the most likely specific interaction would involve the PMMA carbonyl group with the PVC chlorine atom, its labile hydrogen or its C-Cl bond. From this it would be expected that the C=O stretching band in Raman or other infra-red spectroscopy, would shift as the concentration of PVC was increased. It can be seen in figure 6.2 that no band shifts were observed in the C=O stretching band. This does not necessarily indicate that there was no interaction involving the carbonyl group. Rather, if there was the expected interaction between the PMMA carbonyl and the PVC, the resolution of the instrument used ($7cm^{-1}$), was too low to detect it. Coleman and Painter [13] found that the IR frequency shift in the carbonyl band of miscible blends of polyesters, polyacetates and polyacrylates with PVC to be less than $6cm^{-1}$. Schmidt *et al* [54] used ATR-FTIR on miscible PVC/PMMA blends at a resolution of $4cm^{-1}$ and were unable to detect carbonyl band shift. It is likely, therefore, that this interaction is very weak and requires high resolution IR spectroscopy to detect it.

6.3 XPS studies

6.3.1 Results

XPS spectra were acquired on all of the blends across the composition range at intervals of 10%. Two take-off angles were used, 60° and 30° with respect to the sample surface, and three spectra were taken at each take off angle for each composition. C 1s curve fits for homo-PVC and homo-PMMA are shown in chapter five. Figure 6.3 shows a typical C 1s curve fit for a 50/50 blend, taken at a 60° take off angle. It is fitted with five contributions, one common to both polymers, one unique to PVC and three unique to PMMA. From the XPS data, carbon to oxygen ratios

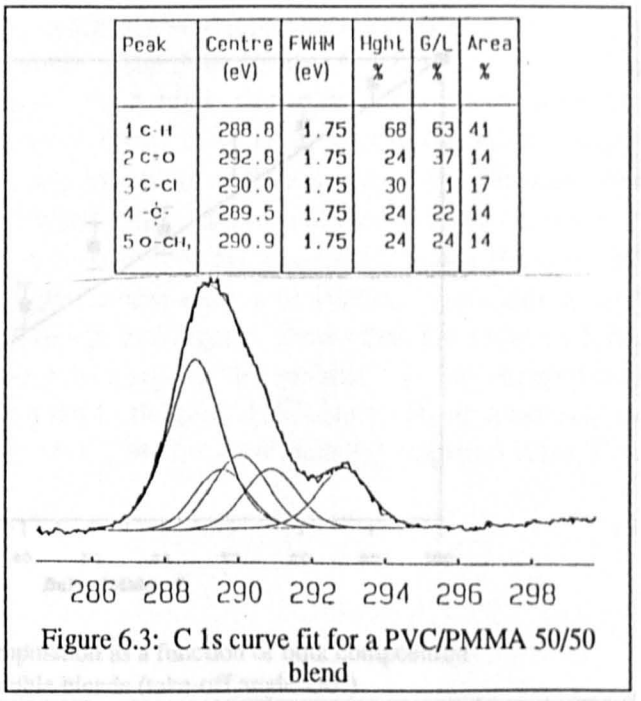

Figure 6.3: C 1s curve fit for a PVC/PMMA 50/50 blend

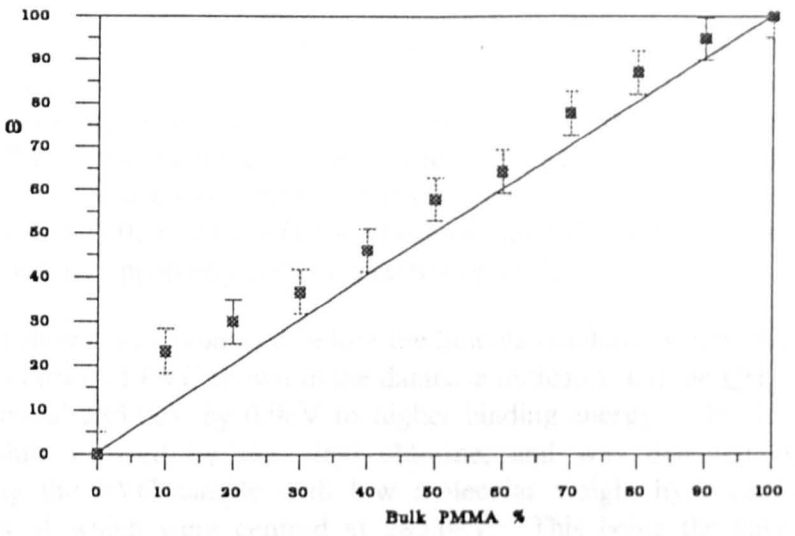

Figure 6.4: Surface weight composition as a function of bulk composition in PVC/PMMA miscible blends (take-off angle=60°)

for each composition at both take-off angles were obtained from the C 1s and O 1s raw peak data, using appropriate sensitivity factors. The surface weight percentage ω was then obtained for each blend by inserting values of the C:O ratio in equation 3.9 (page 54). The empirical value of the C:O ratio for PMMA was kept constant (at the mean value) throughout the range of calculations. Figure 6.4 shows a plot of ω as a function of blend composition, at a take-off angle of 60°. The diagonal line indicates values of ω which are equivalent to the bulk composition, *i.e.* a surface composition reflecting that of the bulk. The error bars represent the widest scatter of any of the three values about the mean. Figure 6.5 shows the corresponding plot found using a take-off angle of 30°.

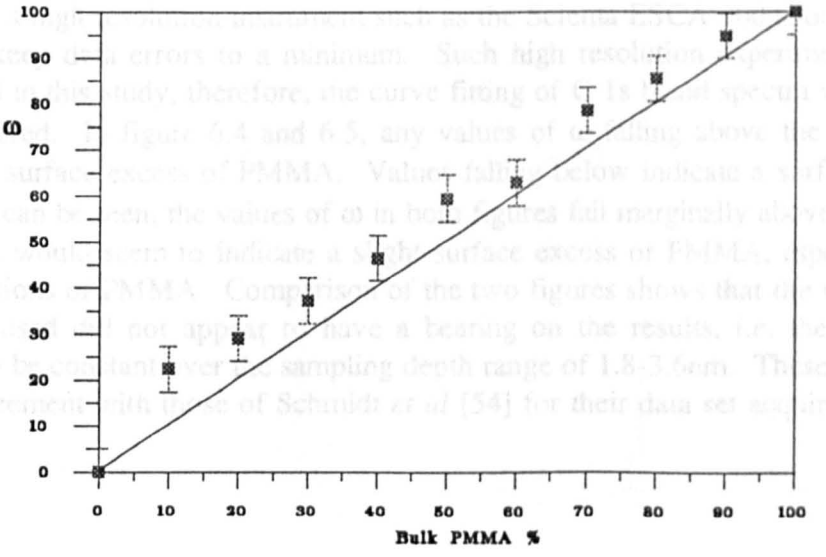

Figure 6.5: Surface weight composition as a function of bulk composition in PVC/PMMA miscible blends (take-off angle=30°)

6.3.2 Discussion

In chapter three spectral information from the high resolution Scienta database [36] was quoted regarding the peak positions of deconvoluted C 1s spectra for PMMA and PVC. If the $\underline{C}H_n$ contribution for both polymers was centred at the same point, the fitting of the PVC/PMMA 50/50 blend with five contributions, as is the case in figure 6.3, would be valid. In the event curve fitting of the C 1s envelope with so many contributions, using the CLAM 100, is unsatisfactory because several conflicting curve fits can be produced which are apparently correct spectroscopically.

The curve fit shown was produced before the Scienta database was published. The high resolution spectrum of PVC shown in the database indicates that the $\underline{C}H_n$ peak is shifted from the nominal 285.0eV by 0.9eV to higher binding energy. This is the result of a secondary shift induced by the vinyl chlorine, and was detected by deliberately contaminating the PVC sample with low molecular weight hydrocarbons, the C 1s contributions of which were centred at 285.0eV. This being the case, in order for spectroscopic validity, the C 1s curve of a PVC/PMMA 50/50 blend should be fitted with *six* contributions centred at separate positions, four due to PMMA and two due to PVC. This has been tried on the C 1s spectra acquired using the CLAM 100. Due to the relatively poor energy resolution, this was found to be a meaningless exercise, as the amount of conflicting curve fits obtainable greatly increased.

Schmidt *et al* [54] in their XPS studies on PVC/PMMA miscible blends, used three components to fit the C 1s curve of PMMA (hydrocarbon, carbonyl and methyl ester) and four to fit those of the blends (the three PMMA components plus the PVC $\underline{C}$-Cl, $\underline{C}H_n$ common to both polymers). The surface data found was then used to produce surface versus bulk composition plots of the type shown in figure 6.4 and 6.5. The instruments they used were the PHI 5100 and PHI 5400, neither of which used a monochromated source. From what is now known about the high resolution C 1s fits of both polymers, it is clear that the error bars in Schmidt's composition plots *must* be considerably larger than those shown. In order to obtain valid surface versus bulk composition plots for polymer blends, using surface information obtained from C 1s curve fits, a high resolution instrument such as the Scienta ESCA 300 should be used in order to keep data errors to a minimum. Such high resolution experiments were not performed in this study, therefore, the curve fitting of C 1s blend spectra will no longer be considered. In figure 6.4 and 6.5, any values of ω falling above the diagonal line indicate a surface excess of PMMA. Values falling below indicate a surface excess of PVC. As can be seen, the values of ω in both figures fall marginally above the diagonal line which would seem to indicate a slight surface excess of PMMA, especially at low concentrations of PMMA. Comparison of the two figures shows that the value of take-off angle used did not appear to have a bearing on the results, *i.e.* the composition appears to be constant over the sampling depth range of 1.8-3.6nm. These observations are in agreement with those of Schmidt *et al* [54] for their data set acquired using C:O ratios.

6.4 ToFSIMS studies

6.4.1 Results

The negative ion spectra in the range 0-100amu are shown in figure 6.6 for homo-PMMA, homo-PVC and a 50/50 PVC/PMMA blend.

Normalized peak intensities from the negative ion spectrum were determined for peaks of interest, across the PVC/PMMA composition range at intervals of 10%. These peaks of interest were m/z=16$^-$ (O^-), 31$^-$ (CH_3O^-), 35$^-$ (Cl^-), 55$^-$ (CH_2CHCO^-), 70$^-$ (Cl_2^-)and 85$^-$ ($CH_2C.CH_3.COO^-$). The NPI-bulk composition plots for these peaks are shown in figures 6.7, 6.8, 6.9, 6.10, 6.11 and 6.12 respectively. Peaks in the m/z=0-50 range were normalized over the total ion count from 0-100amu. Peaks with m/z>50 were normalized over the ion count from 50-100amu. The objective of making these plots was to try to assess whether they could be used to detect preferential surface adsorption of one of the components.

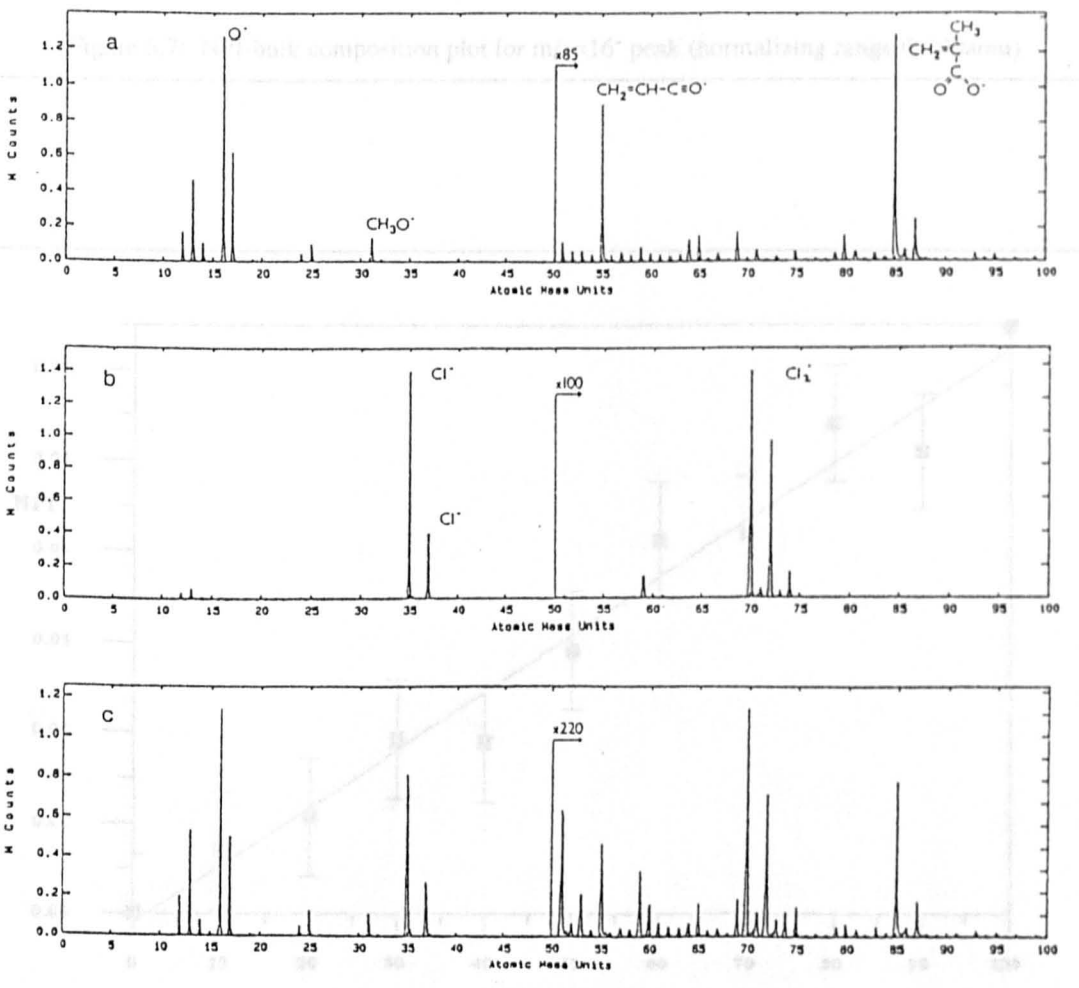

Figure 6.6: ToFSIM negative ion spectra for (a) PMMA homopolymer, (b) PVC homopolymer and (c) PVC/PMMA 50/50 blend

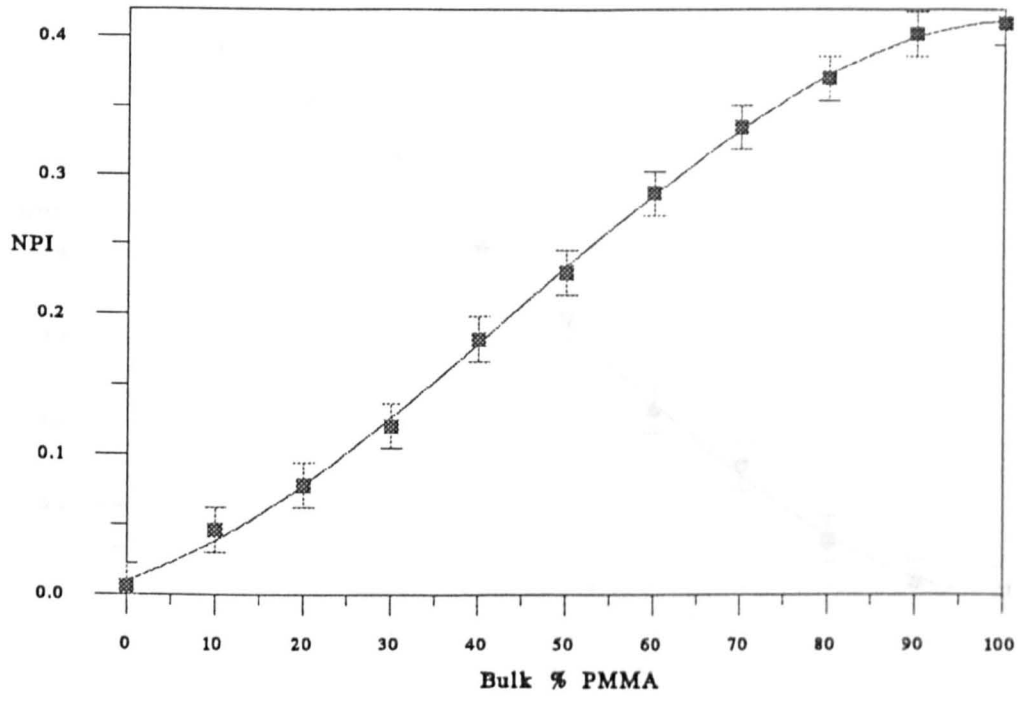

Figure 6.7: NPI-bulk composition plot for m/z=16⁻ peak (normalizing range 0-100amu)

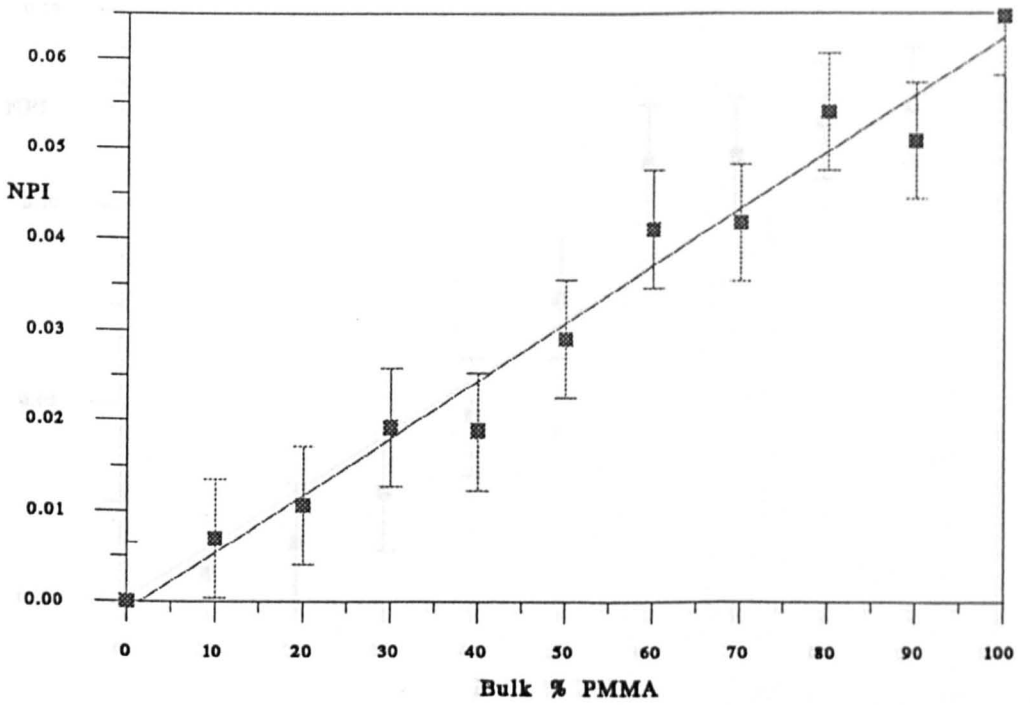

Figure 6.8: NPI-bulk composition plot for m/z=31⁻ peak (normalizing range 0-100amu)

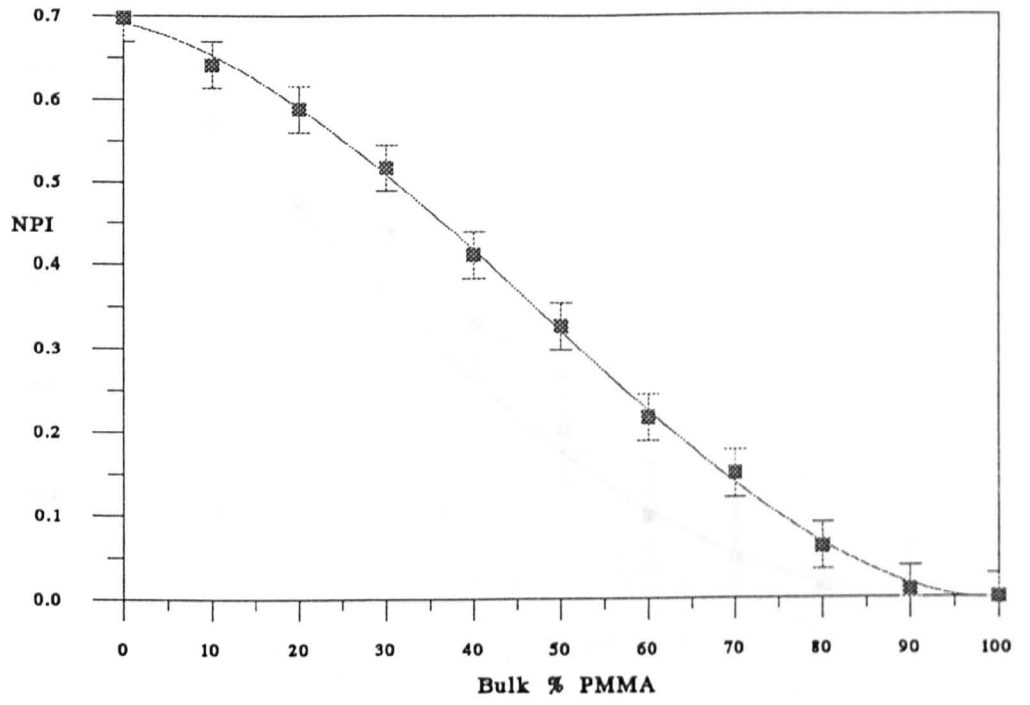

Figure 6.9: NPI-bulk composition plot for m/z=35$^-$ peak (normalizing range 0-100amu)

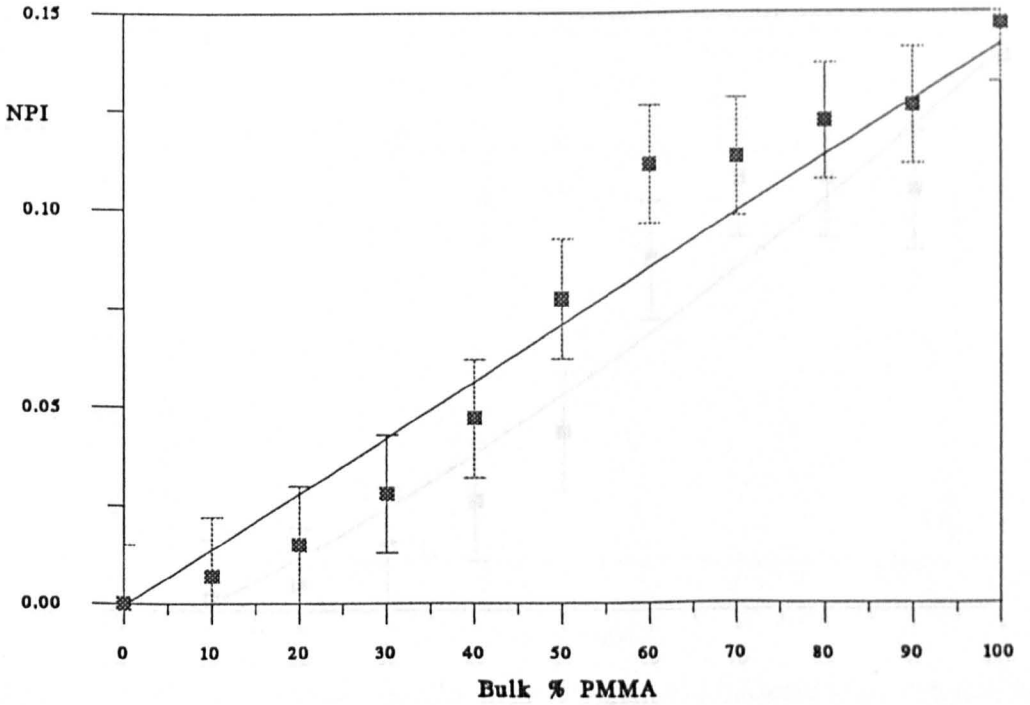

Figure 6.10: NPI-bulk composition plot for m/z=55$^-$ peak (normalizing range 50-100amu)

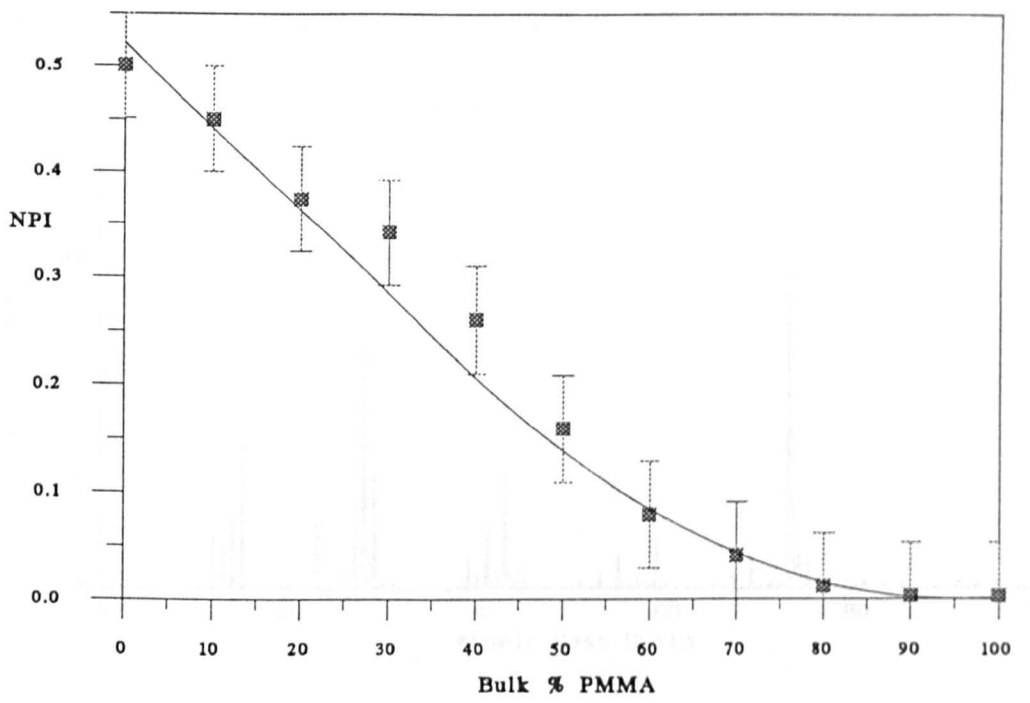

Figure 6.11: NPI-bulk composition plot for m/z=70^{-} peak (normalizing range 50-100amu)

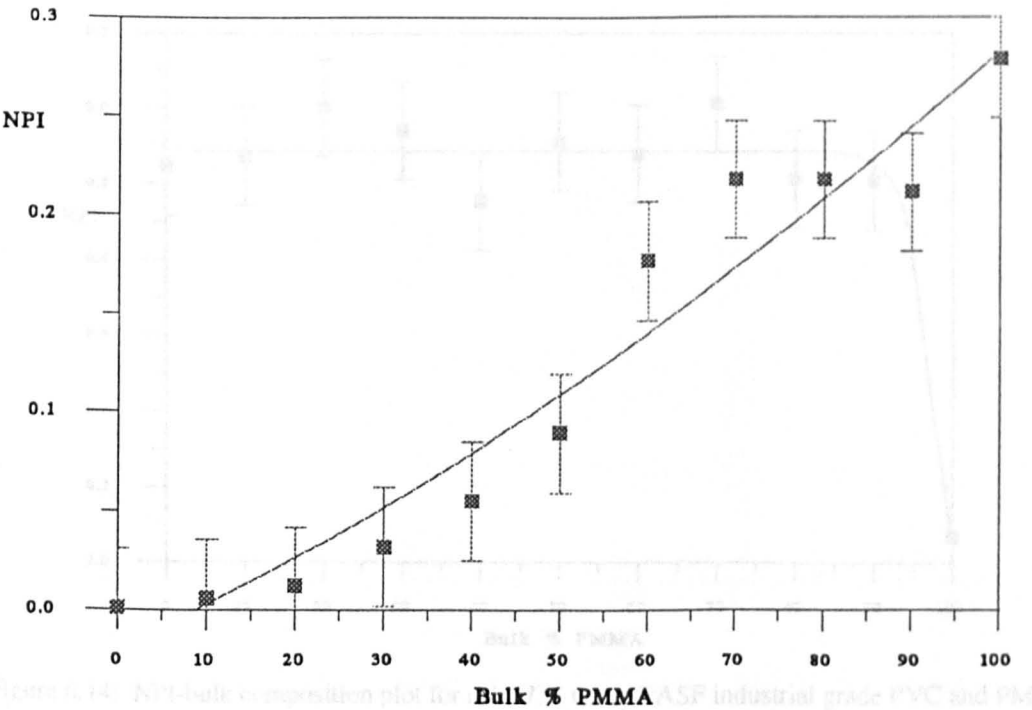

Figure 6.12: NPI-bulk composition plot for m/z=85^{-} peak (normalizing range 50-100amu)

A positive ion spectrum relevant to the following discussion section is shown in figure 6.13. It was acquired from a PVC/PMMA 50/50 blend which had been contaminated with poly(dimethyl siloxane). The polymers in this case had not been the Fluka

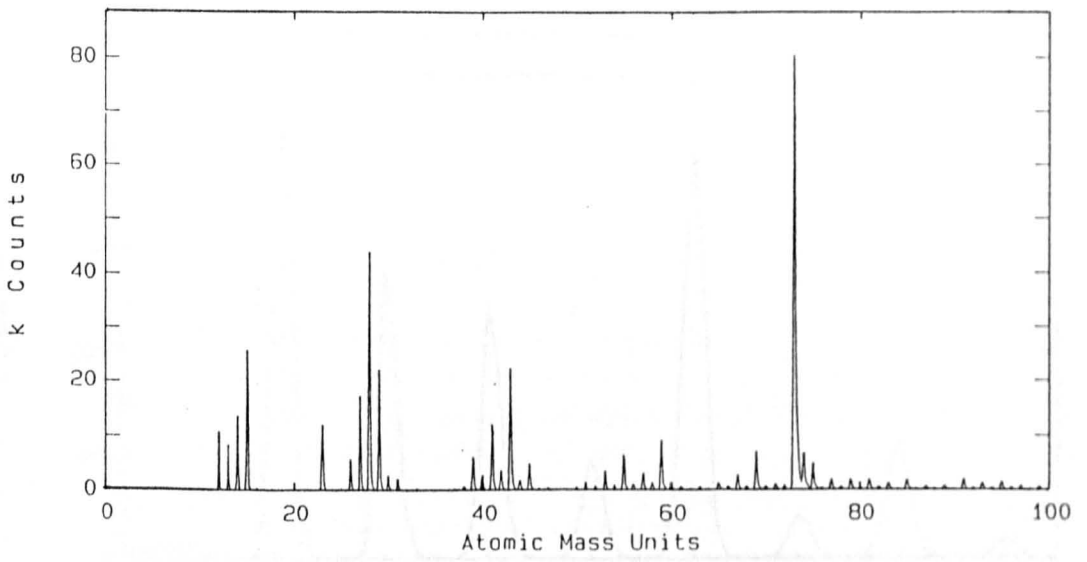

Figure 6.13: Positive ToFSIM spectra of a 50/50 blend using BASF industrial grade PVC and PMMA

Selectaphore PVC and Polymer Laboratories PMMA, as had been used in all other cases for results in this chapter. Instead BASF industrial grade PVC and PMMA had been used. The distinguishing ion for PDMS is at m/z=73^+, the trimethyl silyl ion. The NPI of this ion plotted across the composition range is shown in figure 6.14.

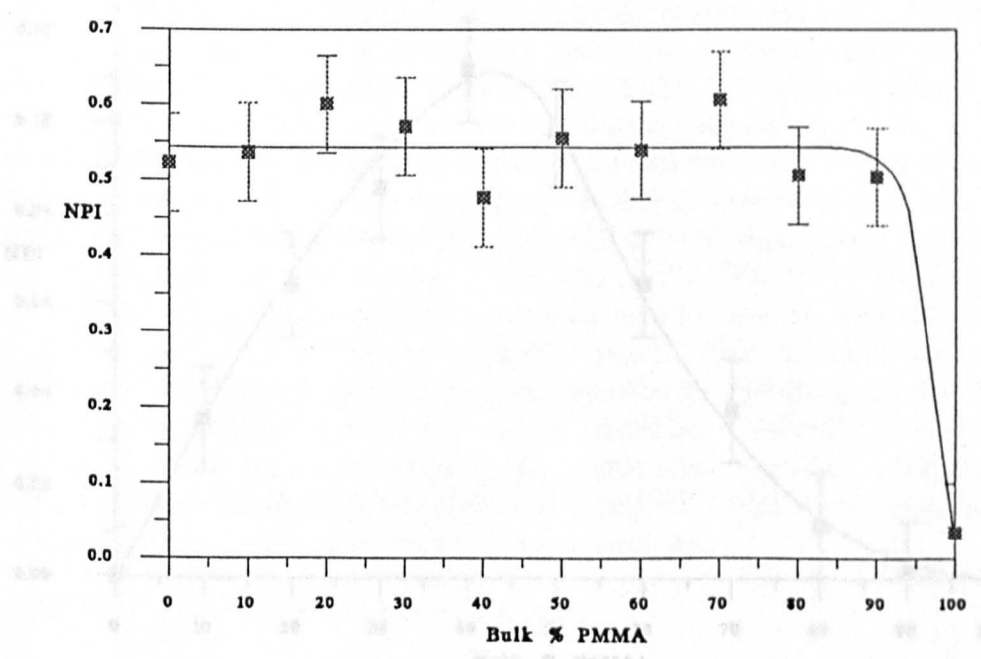

Figure 6.14: NPI-bulk composition plot for m/z=73^+ using BASF industrial grade PVC and PMMA (normalising range 50-100amu)

The negative ion spectrum shown in figure 6.15 was acquired from a PVC/PMMA 50/50 blend. These peaks have not been previously reported in the literature, and tentative assignments are given in the discussion. The NPI-bulk composition plot for the m/z=51$^-$ peak is given in figure 6.16.

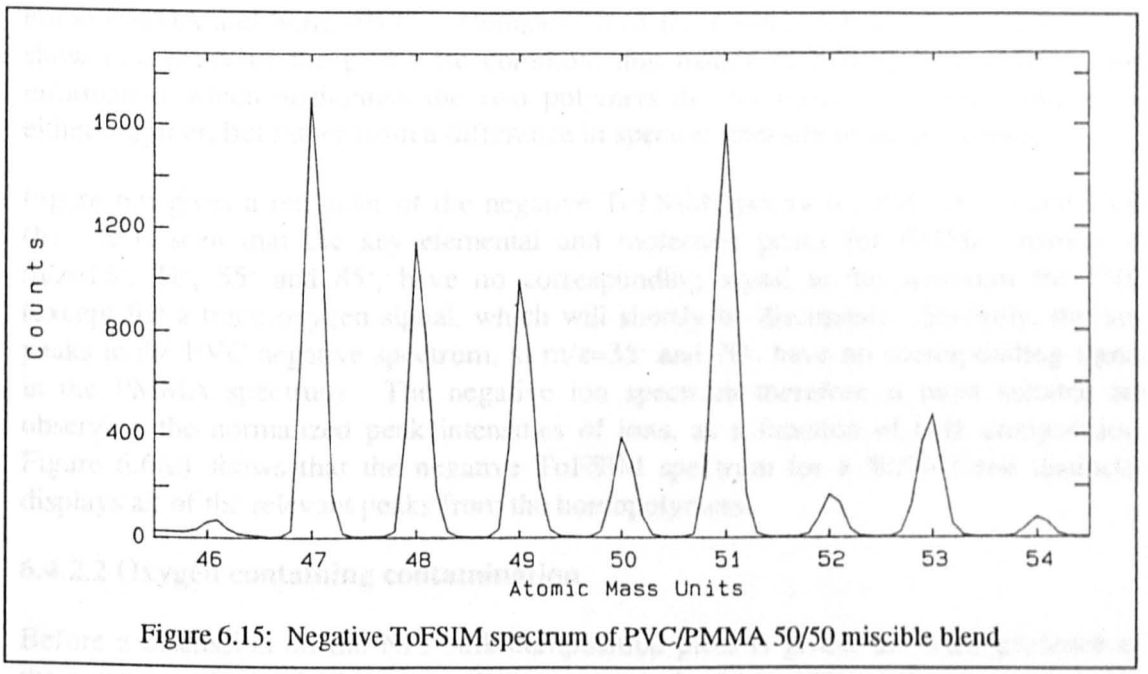

Figure 6.15: Negative ToFSIM spectrum of PVC/PMMA 50/50 miscible blend

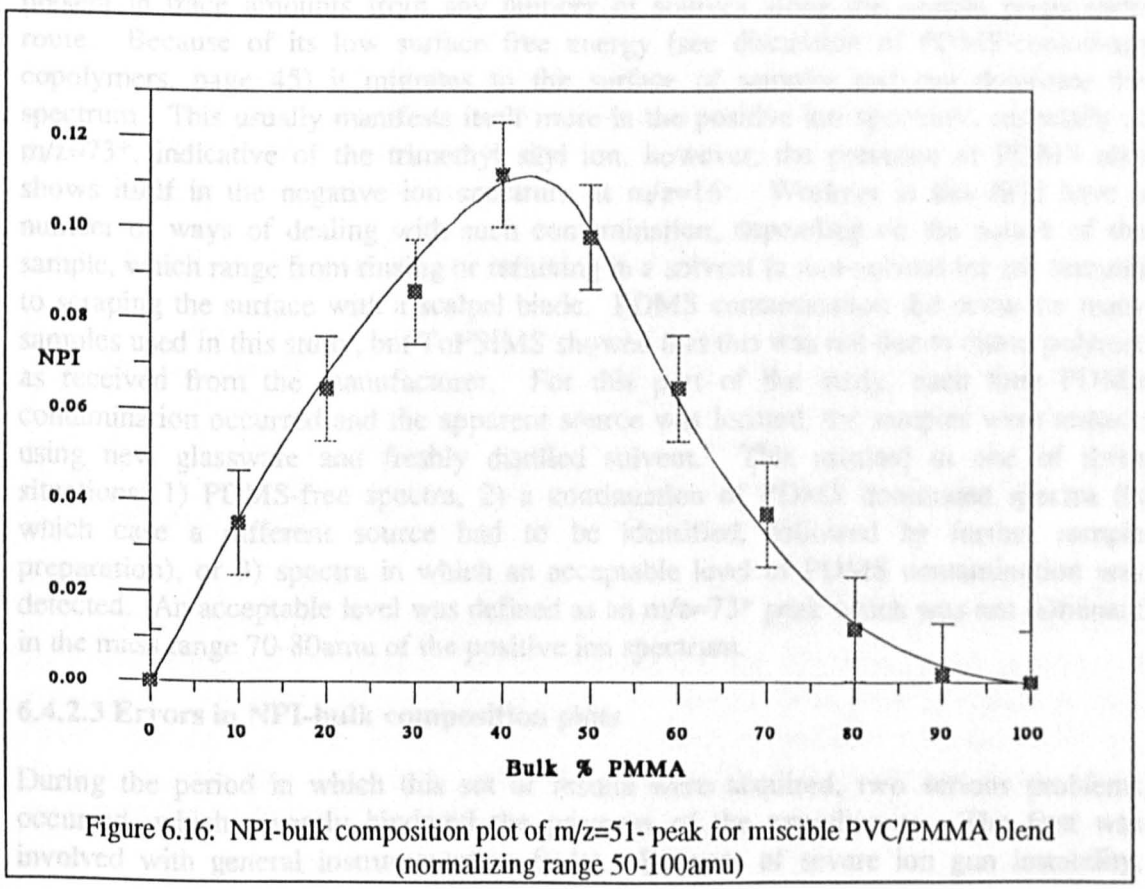

Figure 6.16: NPI-bulk composition plot of m/z=51- peak for miscible PVC/PMMA blend (normalizing range 50-100amu)

6.4.2 Discussion

6.4.2.1 The advantage of using negative ion spectra for PVC/PMMA blends

In chapter five, both the positive and negative ToFSIM spectra were presented for homo-PMMA and homo-PVC. Comparison of the positive ion spectra (pages 69-71) show that many of the peaks are common, due mainly to hydrocarbon clusters, and information which distinguish the two polymers do not result from peaks unique to either polymer, but rather from a difference in spectral intensity of certain peaks.

Figure 6.6 gives a reminder of the negative ToFSIM spectra for PMMA (a) and PVC (b). It is seen that the key elemental and molecular peaks for PMMA, namely at $m/z=16^-$, 31^-, 55^- and 85^-, have no corresponding signal in the spectrum for PVC (except for a trace oxygen signal, which will shortly be discussed). Similarly, the key peaks in the PVC negative spectrum, at $m/z=35^-$ and 70^-, have no corresponding signal in the PMMA spectrum. The negative ion spectrum therefore is most suitable for observing the normalized peak intensities of ions, as a function of bulk composition. Figure 6.6(c) shows that the negative ToFSIM spectrum for a 50/50 blend distinctly displays all of the relevant peaks from the homopolymers.

6.4.2.2 Oxygen containing contamination

Before a discussion on the NPI-bulk composition plots is given, the trace presence of the oxygen peak at $m/z=16^-$ in the PVC spectrum should be addressed. This is probably due to contamination by poly(dimethyl siloxane) (PDMS). This is a common problem for users of highly surface sensitive techniques such as ToFSIMS. PDMS can be present in trace amounts from any number of sources along the sample preparation route. Because of its low surface free energy (see discussion of PDMS-containing copolymers, page 45) it migrates to the surface of samples and can dominate the spectrum. This usually manifests itself more in the positive ion spectrum, especially at $m/z=73^+$, indicative of the trimethyl silyl ion, however, the presence of PDMS also shows itself in the negative ion spectrum at $m/z=16^-$. Workers in this field have a number of ways of dealing with such contamination, depending on the nature of the sample, which range from rinsing or refluxing in a solvent (a non-solvent for the sample) to scraping the surface with a scalpel blade. PDMS contamination did occur on many samples used in this study, but ToFSIMS showed that this was not due to either polymer as received from the manufacturer. For this part of the study, each time PDMS contamination occurred and the apparent source was located, the samples were remade using new glassware and freshly distilled solvent. This resulted in one of three situations: 1) PDMS-free spectra, 2) a continuation of PDMS dominated spectra (in which case a different source had to be identified, followed by further sample preparation), or 3) spectra in which an acceptable level of PDMS contamination was detected. An acceptable level was defined as an $m/z=73^+$ peak which was not dominant in the mass range 70-80amu of the positive ion spectrum.

6.4.2.3 Errors in NPI-bulk composition plots

During the period in which this set of results were acquired, two serious problems occurred, which severely hindered the progress of the experiments. The first was involved with general instrumentation faults. Because of severe ion gun instability,

detector channel plate replacement, an extraction optics overhaul and most serious, a vacuum leak which proved very difficult to pinpoint, a total of six months ToFSIMS downtime was incurred. The second problem was concerned with PDMS contamination, as mentioned in the previous section. The identification of PDMS sources proved to be a very time consuming process.

Due to this combination of difficulties, only one reliable set of spectra, from which NPI data across the composition range could be extracted, was acquired. This obviously is not a statistically advantageous situation, though it is thought that the general trends shown in the NPI-bulk composition plots are extremely valid.

Because of the lack of several data points from which to determine a mean and standard deviation for each NPI-bulk composition point, it is necessary to infer an error range for these results. Recalling the discussion in chapter five regarding the errors in normalized peak intensities (page 72), it would not be valid to directly transfer the NPI standard deviations or standard errors found in that study, onto the data points shown in the NPI-bulk composition plots. The reason for this is that the previous study examined the NPI's for one composition only, 100% PMMA, whereas here the whole composition range is examined. What the previous study provided however, was an *indication* of what the error in results might be. For elementals and quasi-elementals (*e.g.* CH^-) the standard error in the PMMA study was found to be within ±2%. It would therefore seem fair to apply error bars on elemental ions of ±4% in the present study, and expect NPI's to fall within that range.

The PMMA study found that for molecular ions, using an appropriate normalizing range, the standard errors were found to be within ±5%. A fair error range for molecular ions would seem to be ±10% for NPI-bulk composition data. The NPI error ranges therefore shown in these plots were ±4% for elementals and quasi-elementals, and ±10% for molecular ions. The error bars were defined as the appropriate percentage error in the *maximum* NPI reading, this being applied to all NPI points in the remainder of the bulk composition range.

6.4.2.4 NPI-bulk composition behaviour of PMMA ions

Figure 6.7 shows the NPI-bulk composition behaviour for the m/z=16^- ion. It reaches a maximum at 100% PMMA, after gradually increasing from its minimum point at 100% PVC. This point is not zero as would be expected, but slightly positive due to the trace amount of PDMS contamination previously discussed, and seen in the PVC homopolymer spectrum in figure 6.6(b). The increase in the m/z=16^- ion is essentially linear, although a slightly cubic curve has been fitted to the data points.

For the m/z=31^- ion (figure 6.8) there is again a linear increase in NPI from the zero point at 100% PVC to a maximum at 100% PMMA. Figures 6.10 and 6.12 also show approximately linear increases in NPI for the m/z=55^- and 85^- ions, from a minimum at 100% PVC to a maximum at 100% PMMA. For the 55^- peak there is a point at 60% PMMA concentration for which the error range does not coincide with the fitted line. For the 85^- peak there are similar points at 60% and 70% PMMA concentration. These are considered to be spurious points.

It should be pointed out that before a spectrum was accepted for being part of this study, the optimum charge neutralisation conditions available with this instrument were achieved. This was determined by only accepting spectra in which the intensity of the m/z=85$^-$ peak was "reasonable" with respect to that of the m/z=55$^-$ peak. For bulk compositions which contained mainly PMMA, a reasonable intensity for the 85$^-$ peak was defined as one which was greater than that for the 55$^-$ peak. For compositions containing mostly PVC, the effects of differential charging on the 85$^-$ peak were much more severe, possibly a result of the highly intense emission of Cl^- and Cl_2^- ions. For those compositions, a reasonable intensity for the 85$^-$ peak was defined as one which was equal to or only slightly less than that of the 55$^-$ peak.

6.4.2.5 NPI-bulk composition behaviour of PVC ions

Figure 6.9 shows the NPI-bulk composition plot for the m/z=35$^-$ ion due to chlorine emission. As would be expected, it has a maximum NPI at 100% PVC and falls to zero NPI at 100% PMMA. The decrease is approximately linear, but as in the case for the m/z=16$^-$ ion, a slightly cubic curve gives the best fit.

The plot shown in figure 6.11 indicates that the m/z=70$^-$ peak due to Cl_2^- decreases in NPI at a slightly greater rate than the 35$^-$ ion. Between 100% PVC and a PMMA concentration of 70%, this decrease is linear. Beyond this point the rate of NPI decrease reduces until a zero point is reached at 100% PMMA. This is evidence that the presence of PMMA reduces the formation probability of Cl_2^- with respect to singly ionised chlorine. As in the case for the m/z=85$^-$ ion this is possibly due to differential charging effects.

6.4.2.6 Predicted NPI-bulk composition behaviour for ions from a preferentially adsorbed overlayer

Figure 6.13 shows the positive ToFSIM spectrum for a PVC/PMMA 50/50 blend made from BASF industrial grade polymers. The m/z=73$^+$ peak dominates the spectrum and is indicative of PDMS contamination. Analysis of the homopolymer films showed that the source of the contamination was the particular batch of PVC that was being used. The homo-PMMA spectrum did not give any indication of being contaminated by PDMS.

The NPI of the m/z=73$^+$ peak is plotted as a function of blend composition in figure 6.14. At 100% PVC, the NPI of the 73$^+$ peak is at its maximum value (within the error range). This value is constant throughout the whole of the blend composition, except when it reaches 100% PMMA. At this point the NPI sharply reduces to a negligible level. The interpretation of this plot is as follows: whenever PVC is present, so is PDMS. Although present only in trace amounts, its low surface free energy with respect to either PVC or PMMA drives the PDMS to the surface, thus forming a preferentially adsorbed layer.

From their XPS data, Schmidt *et al* [54] predicted that preferentially adsorbed PMMA was a possibility, although their surface data was within error limits of the bulk composition, across the whole composition range for miscible blends. The XPS data in the present study (section 6.3) has shown similar findings. ToFSIMS under static SIMS conditions is more surface sensitive than XPS. If these blends exhibited preferential

surface adsorption of the PMMA component, detectable by XPS, it would also be detectable by ToFSIMS only much more distinctly.

It is proposed that any polymer in a polymer blend, which forms a preferentially adsorbed layer at the surface, would have an NPI-bulk composition plot similar to that shown in figure 6.14, for any of the characteristic ions in its ToFSIM spectrum. For the PVC/PMMA blend, if the PMMA component underwent preferential surface adsorption, the NPI-bulk composition plot for the m/z=16$^-$, 31$^-$, 55$^-$ or 85$^-$ peak would have a shape similar to that shown in figure 6.17. Although the shape shown here may be exaggerated, one would expect the NPI to rise with PMMA concentration, until at some intermediate point, a maximum NPI value is reached which is maintained until the limit of the composition range. As this NPI value is the same as that for homo-PMMA, the point at which the maximum value is first attained corresponds to the composition at which complete surface enrichment by PMMA is reached.

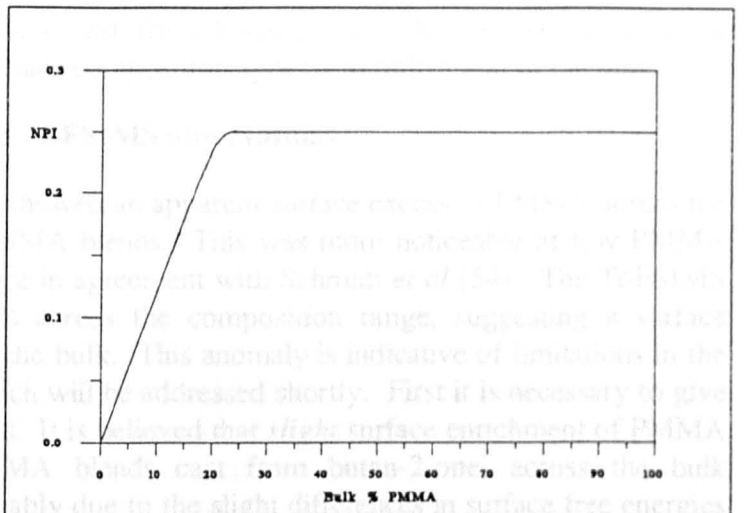

Figure 6.17: Predicted NPI-bulk composition behaviour for PMMA ions, for PVC/PMMA blends in which preferential surface adsorption of the PMMA component occurs

Based on this argument, the predicted NPI behaviour of PVC ions for blends exhibiting preferential surface adsorption of PMMA is seen in figure 6.18. As in the predicted case for PMMA ions, the shape of the plot may be exaggerated, but it would be expected that the NPI would have a maximum value at 100% PVC and then sharply decline with increasing PMMA concentration, until at a certain composition, corresponding to the point of complete surface enrichment by PMMA, the NPI value would reduce to zero, and maintain that value for the remainder of the compositional range.

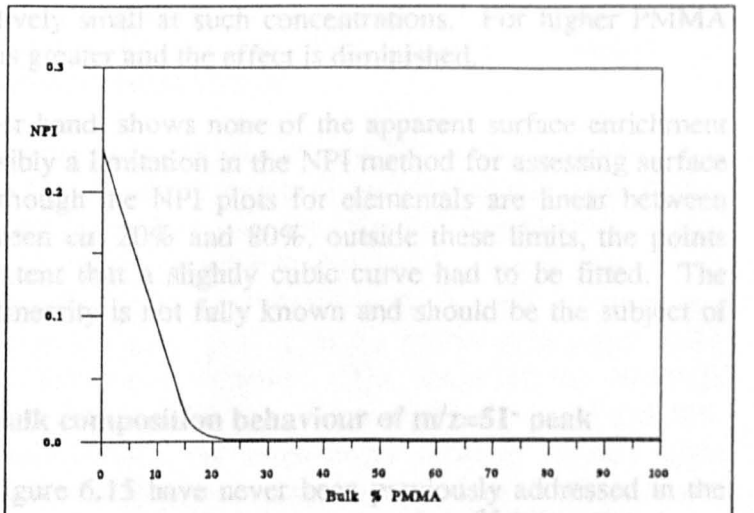

Figure 6.18: Predicted NPI-bulk composition behaviour for PVC ions, for PVC/PMMA blends in which preferential surface adsorption of the PMMA component occurs

It can be clearly seen that the experimental plots obtained do not correspond with the models for preferential surface adsorption of PMMA. From this it can be concluded that under the sample preparation conditions described surface enrichment by PMMA does not occur in PVC/PMMA blends cast from butan-2-one. As the NPI plots show essentially linear trends, the surface composition appears to reflect that of the bulk.

6.4.2.7 Differences in XPS and ToFSIMS observations

The XPS data displayed earlier showed an apparent surface excess of PMMA across the composition range for PVC/PMMA blends. This was more noticeable at low PMMA concentrations. These results are in agreement with Schmidt *et al* [54]. The ToFSIMS NPI data showed linear trends across the composition range, suggesting a surface structure which reflects that of the bulk. This anomaly is indicative of limitations in the data analysis methods used, which will be addressed shortly. First it is necessary to give an interpretation on these results. It is believed that *slight* surface enrichment of PMMA occurs for miscible PVC/PMMA blends cast from butan-2-one, across the bulk composition range. This is probably due to the slight differences in surface free energies for the two homopolymers. This enrichment does not manifest itself as a PMMA overlayer. As there is no significant differences in XPS data acquired at 60° and 30° take-off angles, the PMMA surface enrichment is constant over the outer 3.6nm of the surface. The observation that PMMA surface enrichment is greater at low PMMA concentrations is perhaps a limitation of the method for finding ω values. The form of the ω equation (page 54) means that at low PMMA concentrations, slight errors in the XPS quantification of the O 1s signal result in greater errors in the ω value. This is because the O1s signal is relatively small at such concentrations. For higher PMMA concentrations, the O 1s signal is greater and the effect is diminished.

The ToFSIMS data on the other hand, shows none of the apparent surface enrichment suggested by XPS. This is possibly a limitation in the NPI method for assessing surface composition. For example, although the NPI plots for elementals are linear between PMMA concentrations of between *ca.* 20% and 80%, outside these limits, the points deviate from linearity to the extent that a slightly cubic curve had to be fitted. The reason for this deviation from linearity is not fully known and should be the subject of further investigation.

6.4.2.8 Assignment and NPI-bulk composition behaviour of m/z=51⁻ peak

The series of peaks shown in figure 6.15 have never been previously addressed in the literature. As suggested in chapter five, it is likely that m/z=47⁻ is $^{35}ClC^-$. This being the case, the next three peaks are likely to be due to $^{35}ClCH^-$, $^{37}ClC^-$ and $^{37}ClCH^-$ respectively. The m/z=51⁻ peak is a little more difficult. There are two realistic assignments it can be given which will shortly be proposed. First, it is necessary to observe the NPI-bulk composition behaviour of this ion (figure 6.16). The very small base levels of this ion in the homopolymers have been subtracted proportionally across the composition range. From 100% PVC, the NPI increases sharply to a maximum at between 40 and 50% PMMA concentration. This then gradually drops off, back to the baseline at 100% PMMA. It is apparent that this ion must be formed by contributions from both polymers. Its shape can be compared to that of the curve shown in figure 3.14 (page 49), which showed the compositional dependence of the m/z=213⁺ ion in a

nylon-6/nylon-66 copolymer. This was identified by Briggs [63] as being a fragment due to parts of both monomers in the copolymer structure.

With this comparison in mind, it is tentatively proposed that the m/z=51$^-$ peak is due to $^{35}ClO^-$, the chlorine arising from the PVC, the oxygen from the PMMA. This would lead to assignments of the m/z=52$^-$, 53$^-$ and 54$^-$ peaks of $^{35}ClOH^-$, $^{37}ClO^-$ and $^{37}ClOH^-$ respectively. The m/z=51$^-$ and 53$^-$ peaks have the same intensity ratio as the two Cl isotopes at m/z=35$^-$ and 37$^-$. The immediate conceptual difficulty with this assignment is in understanding how oxygen and chlorine can combine, given their respective sources. There are three possibilities: (1) recombination of sputtered chlorine and oxygen species above the surface; (2) combination of associated oxygen and chlorine at the surface; (3) combination of a surface species with a species that originates from beneath the surface. Of the three, the least likely appears to be option (1), because as pointed out by Brown and Vickerman [101], the density of atoms leaving the surface would be insufficient in SSIMS to make this a probable process. In option (2), "associated" refers to the only oxygen and chlorine likely to be in close enough proximity to combine at the surface, *i.e.* oxygen and chlorine that is taking part in a specific interaction. This too seems unlikely as, although not reproduced here, the 51$^-$ peak was observed in immiscible blends which presumably did not experience such specific interactions. The most likely option is (3). Although SSIMS is a surface technique which probes the outermost surface monolayer, it is possible that elemental species can be sputtered from just beneath the surface , which then go on to combine with other elementals at the surface monolayer, *i.e.* a PMMA oxygen sputtered from just beneath the surface could combine with a PVC chlorine at the surface monolayer and be detected as a negative ion species. This concept can also explain the presence of oxygen in negative ion spectra, at the highest ion doses in which the surface monolayer has essentially a graphite like structure (see section 5.5.2).

This assignment does not explain the trace presence of m/z=51$^-$ in homo-PMMA. For homo-PVC a small amount of 51$^-$ should be expected because of the trace PDMS presence, the oxygen from which can combine with the chlorine. For PMMA though, no chlorine was detected, so it is highly improbable that the 51$^-$ ion in this case involved chlorine. Assuming no other form of contamination, the only structure this peak can be realistically assigned to is $C_4H_3^-$, part of the C_4 hydrocarbon series which is present in small proportions starting at m/z=48$^-$. The shape of the NPI-bulk composition curve shown in figure 6.16 is of interest. It peaks at between 40 and 50% PMMA concentration and is asymmetric. Its shape might seem to indicate slight preferential surface adsorption of PMMA, but given the previous ToFSIMS-bulk composition results, the asymmetry is more likely to be due to the comparatively rapid decrease of the m/z=70$^-$ ion (included in the normalising range) in the presence of PMMA.

Having made a number of observations on miscible PVC/PMMA blends, immiscible blends are now examined.

CHAPTER SEVEN - Surface Studies on Immiscible Polymer Blends

7.1 Overview

In this chapter, following a brief look at bulk analysis results, immiscible PVC/PMMA blends are examined by surface analysis. The blends used in this part of the study were all prepared using BASF PVC and PMMA. All blends were cast from THF. Although solution casting was the main method of blend preparation, a number of blends were prepared by spin casting. The preparation method will be specified as the results are presented. The surface techniques used were conventional XPS, microanalytical XPS, imaging XPS and imaging ToFSIMS.

7.2 Bulk analysis

7.2.1 Results

All blends examined were prepared by solution casting. A DSC thermogram for a 50/50 blend is shown in figure 7.1. Two transition regions can be observed, the transition

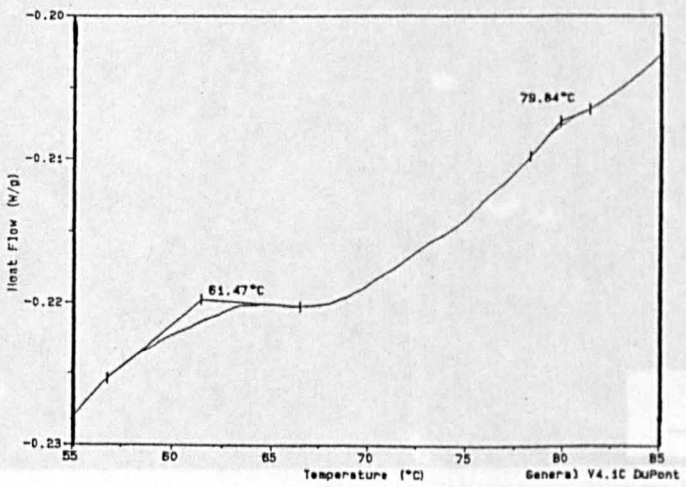

Figure 7.1: DSC thermogram for a PVC/PMMA 50/50 blend cast from THF

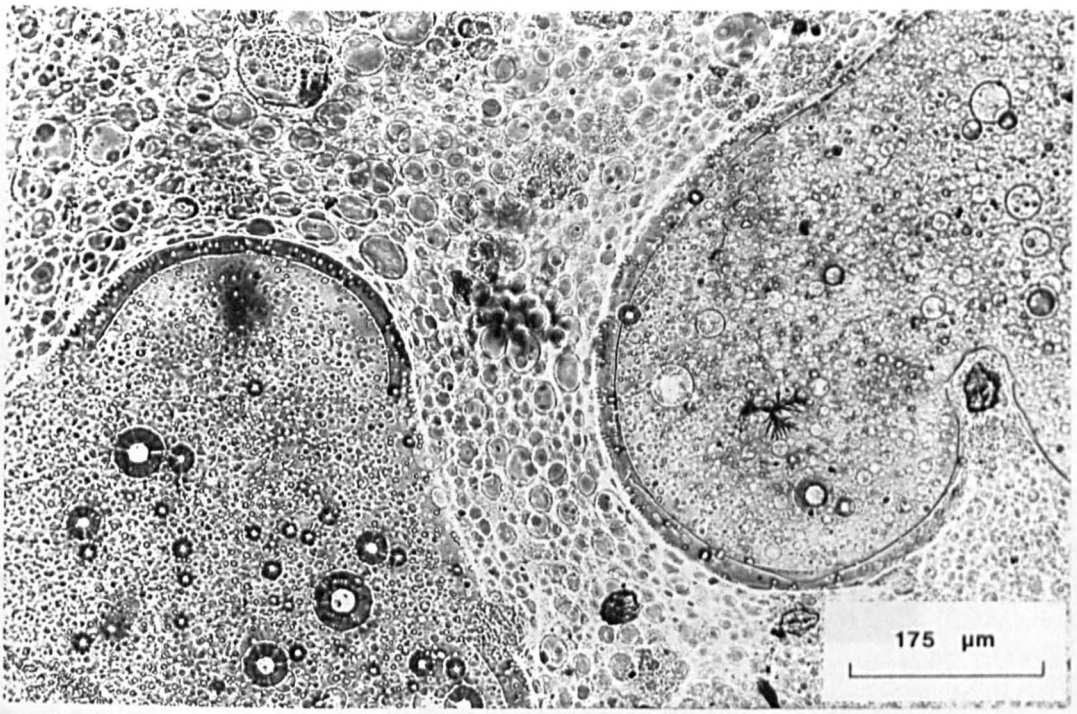

Figure 7.2: Optical micrograph of PVC/PMMA 30/70 blend

temperatures being defined as the onset of the transition region.

Figure 7.2 shows an optical micrograph of a PVC/PMMA 30/70 blend. A scanning electron micrograph of the same region is shown in figure 7.3.

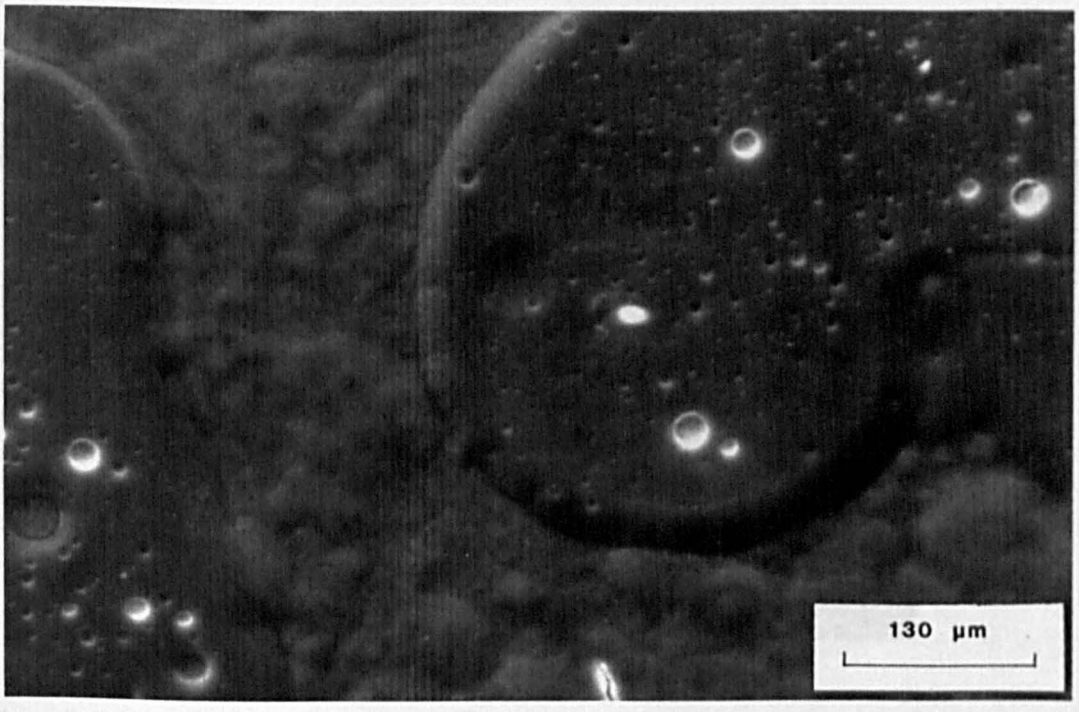

Figure 7.3: Scanning electron micrograph of PVC/PMMA 30/70 blend

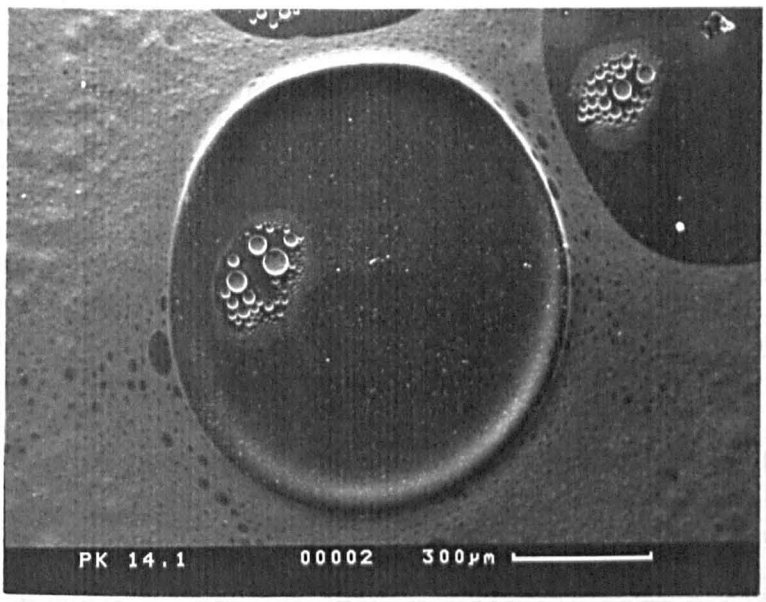

Figure 7.4: Scanning electron micrograph of a PVC/PMMA 50/60 blend prepared in a vacuum oven

A circular feature is displayed in figure 7.4. This is an SEM of a PVC/PMMA 40/60 blend which was prepared in a vacuum oven. A different sample of the same composition was prepared by allowing the solvent to evaporate in a fume cupboard, *i.e.* a vacuum oven was not used. An SEM of part of the film formed using this method is shown in figure 7.5.

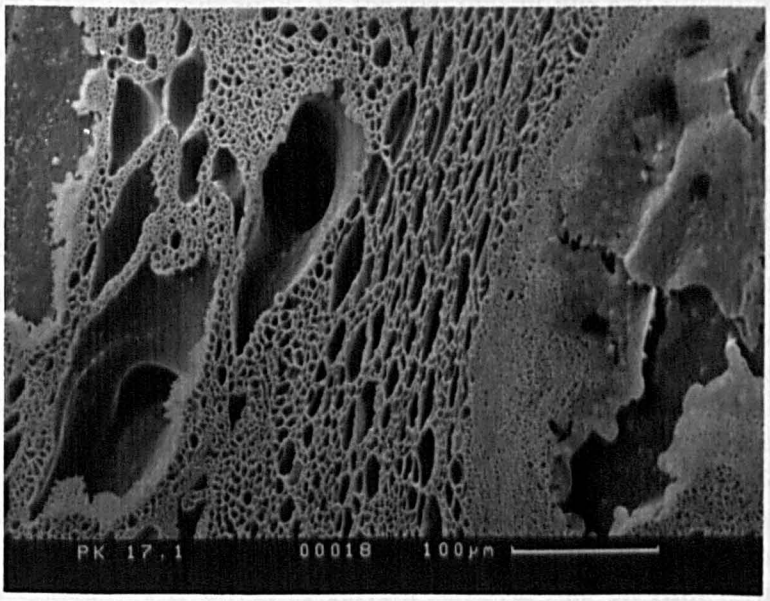

Figure 7.5: Scanning electron micrograph of a PVC/PMMA 40/60 blend prepared in a fume cupboard

7.2.2 Discussion

The DSC thermogram shows two glass transition temperatures, one at 61°C, the other at 78°C. These are the T_g's of the PVC and PMMA homopolymers respectively. Two glass transition temperatures were observed for all blends cast from THF. This is evidence of immiscibility. This becomes more obvious when the optical and scanning electron micrographs are examined. Figures 7.2 and 7.3 are micrographs of the same area of a PVC/PMMA 30/70 blend. This clearly shows that the sample is phase separated in the bulk. By comparing these figures, it is observed that the phase separation in the bulk continues on the same lateral resolution up to at least the outer 1μm, the depth of features identified by SEM.

This sample was prepared in a vacuum oven. The solvent was evacuated at room temperature, and the pressure in the oven during the evacuation was *ca.* $5x10^{-2}$ mb [102]. This also was the case for the PVC/PMMA 40/60 sample shown in figure 7.4. This concentrates on a large, dark shaded, circular domain, within a lighter shaded matrix. The domain is *ca.* 850μm in diameter. Although the film was transparent, the phase boundaries between such large domains and the matrix could quite easily be seen by the naked eye. The identification of phases is unimportant at this point. What is of importance is that within the large dark shaded domain, to the left of centre, secondary domains have formed which are lighter in shade. These are the same shade as the matrix, indicating that the matrix component has formed a secondary domain phase within the primary domain phase. This behaviour has been previously reported by Razinskaya *et al* [89] in their SEM observations of PVC/PMMA blends cast from THF. Within the secondary domains, it can just be seen that there are smaller, dark shaded spots present. This is the primary domain component forming a tertiary domain phase within the secondary domains.

Apart from the secondary domains area, the dark shaded primary domain appears fairly homogeneous [103]. Stereographic SE micrographs of this and similar primary domains showed that they were slightly raised above the matrix phase. Such homogeneity is not the case for the majority of the matrix phase, in which can be seen many, much smaller, primary domains.

The rate of solvent removal had a large bearing on the formation of the precipitated film. If a slow solvent withdrawal rate was used, *e.g.* by placing the uncovered petri dish containing the solution in a fume cupboard and allowing the solvent to evaporate, a very uneven, cloudy film was formed. Solvent entrapment occurred in such films and this had to be removed in a vacuum oven prior to analysis by any UHV technique. Despite this final, rapid removal of remnant solvent, the non-uniform structure of the film was retained. This can be seen in figure 7.5, an SE micrograph of a PVC/PMMA 40/60 blend prepared in a fume cupboard. By contrast, using a fast solvent removal method such as that obtained with a vacuum oven, a comparatively uniform (but phase separated) film was precipitated from solution, as already seen in figure 7.4. The vacuum oven was used to produce films for the main body of the samples used in the study of this system. The effect of solvent removal rate on film formation is again discussed later in this chapter.

7.3 XPS studies

7.3.1 Conventional XPS

7.3.1.1 Results

XP spectra were acquired on spin cast samples across the composition range at intervals of 10%. A take-off angle of 60° was used with respect to the sample surface. Carbon to oxygen ratios were obtained from the C 1s and O 1s raw peak data, using appropriate sensitivity factors. The surface weight percentage of PMMA, ω, was obtained for each blend by inserting values of the C:O ratio in equation 3.9 (page 54). The empirical value of the C:O ratio for PMMA was kept constant throughout the composition range. Figure 7.6 shows a plot of ω as a function of blend composition. As in the equivalent study for miscible blends, the diagonal line indicates values of ω which are equivalent to the bulk composition. Three separate series of spin cast samples were analysed in this way, but only one set of results is shown (*i.e.* this is not an average of the three sets of results)

The same procedure was carried out on blends which had been solution cast, the only difference being that five sets of experiments were performed on each set of films. When the films had been peeled away from the petri dishes, both the air facing side of the films (henceforth called the film/air interface) and the glass facing side (the film/glass interface) were analysed at 60° and 30° take-off angles. A different area of each film was used for each of these experiments. A fifth set of XPS data was acquired by re-analysing the film/air samples which had already been run at 60°, using a take-off angle of 30°.

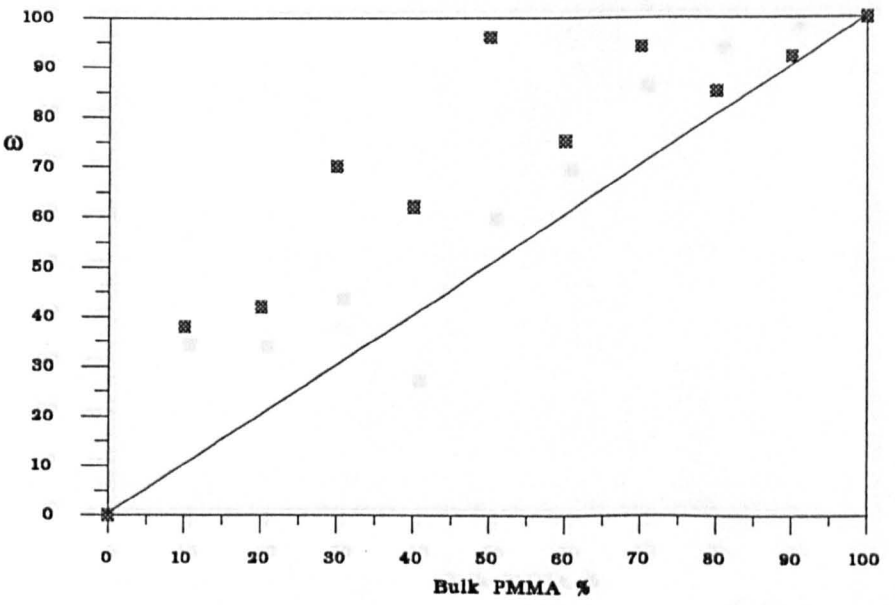

Figure 7.6: Surface weight composition as a function of bulk composition in spin cast PVC/PMMA immiscible blends (take-off angle=60°)

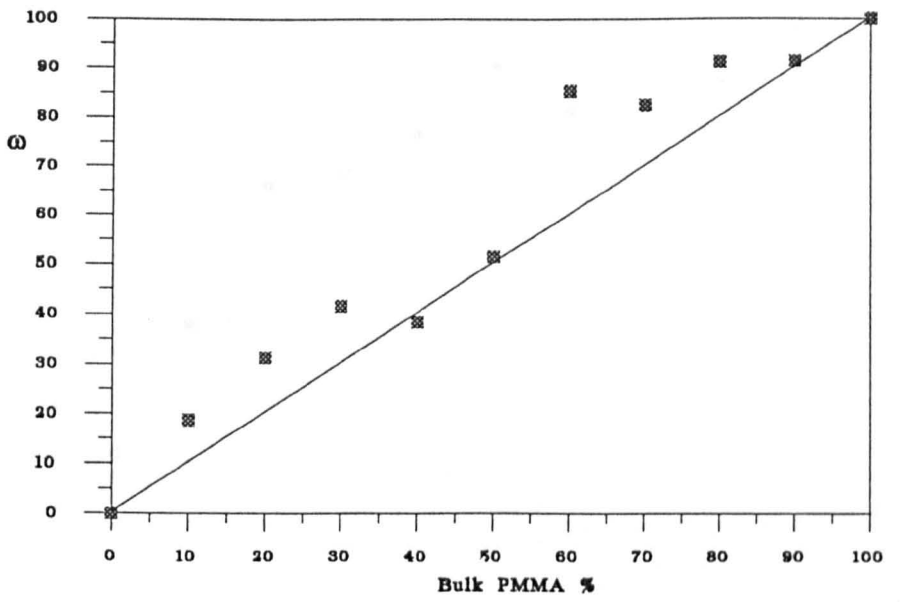

Figure 7.7: Surface weight composition as a function of bulk composition in solution cast PVC/PMMA immiscible blends (film/air interface, take-off angle=60°)

The ω versus bulk composition plots for the film/air interface at 60° take-off angle is shown in figure 7.7. The corresponding plot for the 30° take-off angle (using different samples) is shown in figure 7.8.

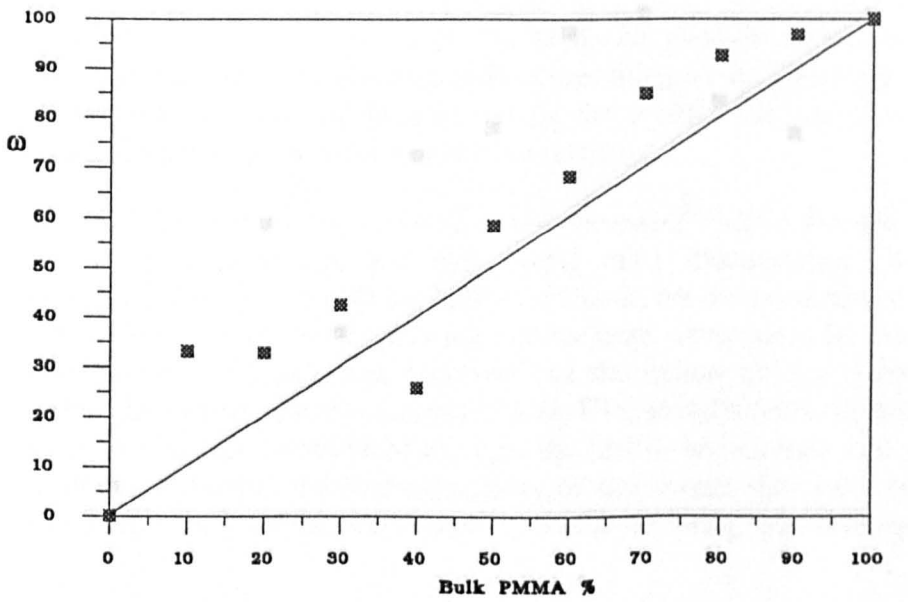

Figure 7.8: Surface weight composition as a function of bulk composition in solution cast PVC/PMMA immiscible blends (film/air interface, take-off angle=30°)

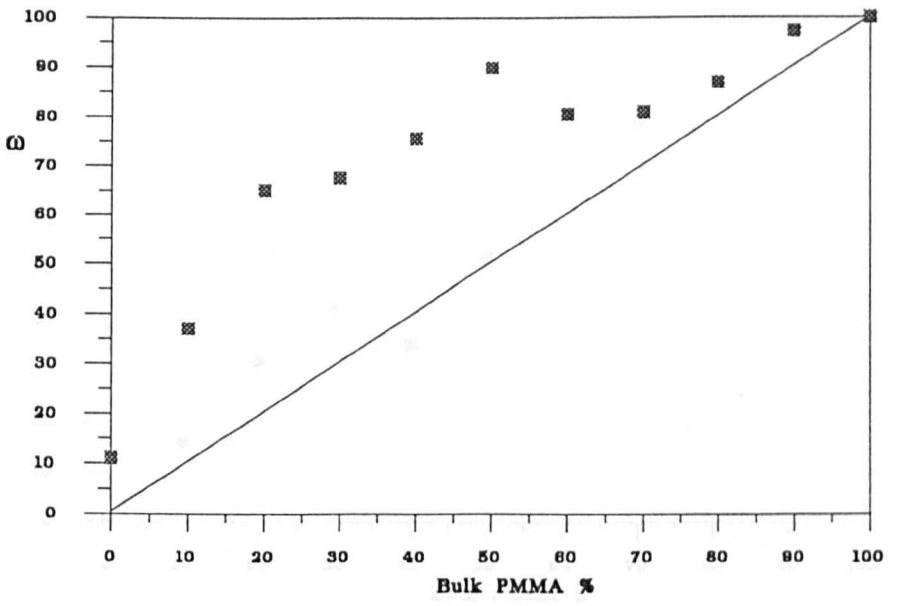

Figure 7.9: Surface weight composition as a function of bulk composition in solution cast PVC/PMMA immiscible blends (film/glass interface, take-off angle=60°)

For the film/glass interfaces, the ω versus bulk composition plots for the 60° and 30° take off angles, are shown in figures 7.9 and 7.10 respectively.

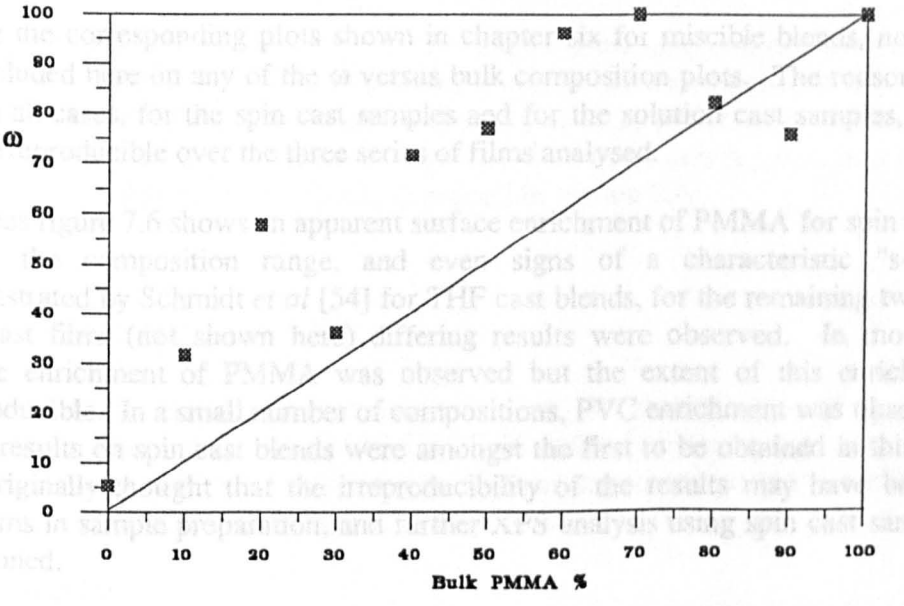

Figure 7.10: Surface weight composition as a function of bulk composition in solution cast PVC/PMMA immiscible blends (film/glass interface, take-off angle=30°)

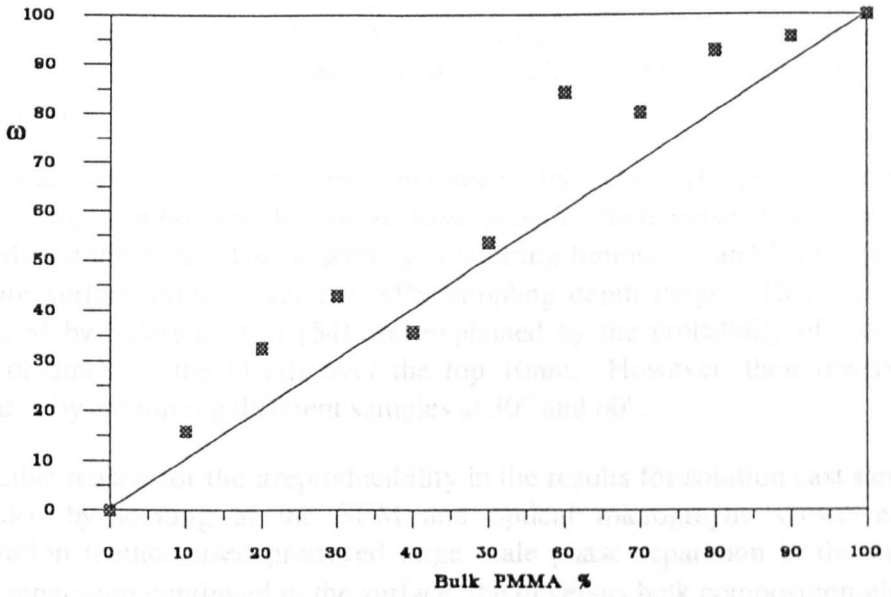

Figure 7.11: Surface weight composition as a function of bulk composition in solution cast PVC/PMMA immiscible blends (film/air interface, take-off angle=30°, samples previously analysed at 60°)

Finally, the ω versus bulk composition plot for the film/air interface samples analysed at 30°, which had previously been analysed at 60°, is shown in figure 7.11.

In all cases for the solution cast samples, three separate series of films were analysed in this way. The plots do not show an average of data from the three sets of films.

7.3.1.2 Discussion

Unlike the corresponding plots shown in chapter six for miscible blends, no error bars are included here on any of the ω versus bulk composition plots. The reason for this is that in all cases, for the spin cast samples and for the solution cast samples, the results were irreproducible over the three series of films analysed.

Whereas figure 7.6 shows an apparent surface enrichment of PMMA for spin cast blends across the composition range, and even signs of a characteristic "s-shape" as demonstrated by Schmidt *et al* [54] for THF cast blends, for the remaining two series of spin cast films (not shown here) differing results were observed. In most cases, a surface enrichment of PMMA was observed but the extent of this enrichment was irreproducible. In a small number of compositions, PVC enrichment was observed. The set of results on spin cast blends were amongst the first to be obtained in this study. It was originally thought that the irreproducibility of the results may have been due to problems in sample preparation, and further XPS analysis using spin cast samples were abandoned.

For solution cast samples however, the irreproducibility in ω versus bulk composition plots continued. For the film/air interface samples (figure 7.7 and 7.8), over three series

of films, the only reproducible trend that could be observed was that most of the plots showed PMMA enrichment across most of the composition range. The extent of this enrichment was irreproducible. Plots obtained from the other two series of films exhibited a mixture of PVC and PMMA enrichment with no apparent compositional dependence.

There was one exception to this irreproducibility: when XP spectra were acquired at take-off angles of 60° and 30° *on the same sample*, the ω versus bulk composition plots were almost identical. This is seen by comparing figures 7.7 and 7.11. This suggests a constant surface profile over the XPS sampling depth range. This was a conclusion arrived at by Schmidt *et al* [54] and explained by the probability of local equilibrium being obtained by the blends over the top 10nm. However, their observations were arrived at by examining different samples at 30° and 60°.

A possible reason for the irreproducibility in the results for solution cast samples may be explained by looking at the SEM and optical micrographs shown earlier. The preparation method used produced large scale phase separation in the bulk. If such phase separation continued to the surface, the ω versus bulk composition plots would be dependant on whether the analysis area included one of the large domains, *i.e.* on the same sample it would be possible to acquire XP spectra on an area which contained either an excess of PMMA or an excess of PVC. If this were the case and phase separation did continue to the surface, then XP spectra obtained at 60 and 30° on the same area, would give very similar ω versus bulk composition plots, as seen in figures 7.7 and 7.11.

For the solution cast films analysed at the film/glass interface, for all three series of films analysed, the ω versus bulk composition plots for both 60° and 30° were irreproducible, but the trend in each case was to an apparent surface enrichment of PMMA at high PVC concentrations. The main problems with this observation was that the trend was also seen at 100% PVC. This indicated one of three possibilities: (1) migration of oxygen containing contamination in the PVC to the film/glass interface, (2) residual solvent in the glass facing side of the film, or (3) oxygen containing contaminants on the glass transferring onto the films. At this stage, if option (1) was correct, it was not thought that this could be due to PDMS contamination, as Si 2p peaks could not be detected in any of the spectra. Before further interpretation on this result is given, it is necessary to examine the ToFSIMS data. This is discussed in section 7.4.

7.3.2 Microanalytical XPS

In the previous section, it was proposed that irreproducibility in ω versus bulk composition plots was a result of PVC/PMMA bulk phase separation continuing to the surface. The possibility of observing such phase separation within the XPS sampling depth was examined using the Scienta ESCA 300.

7.3.2.1 Results

A highly bulk phase separated sample, a solution cast PVC/PMMA 30/70 blend, was chosen for Scienta linescan analysis. A Cl 2p "peak minus background" linescan on this

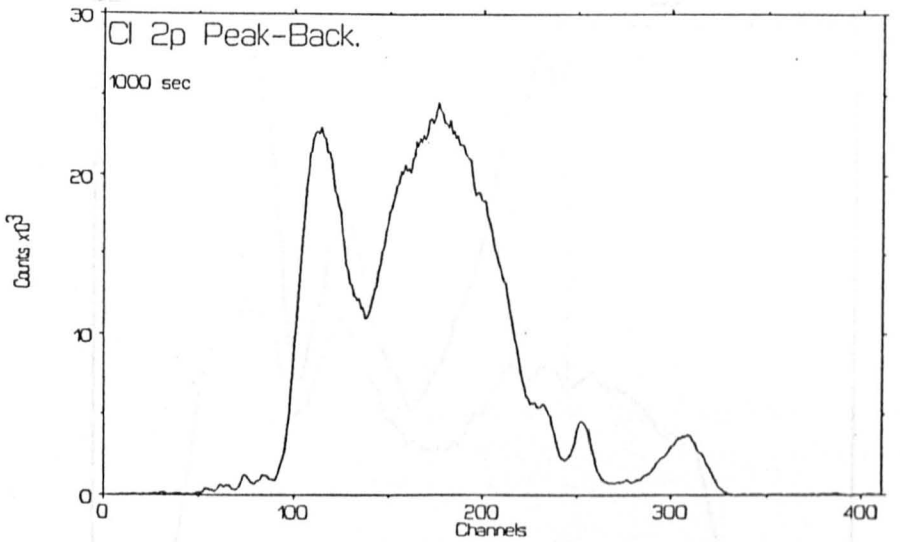

Figure 7.12: Scienta ESCA300 linescan of Cl 2p signal (peak-background) for PVC/PMMA 30/70 blend

sample is shown in figure 7.12. The line was *ca.* 3mm in length and on the linescan, 100 channels is approximately equal to 1mm. the O 1s peak minus background linescan on the same area is shown in figure 7.13.

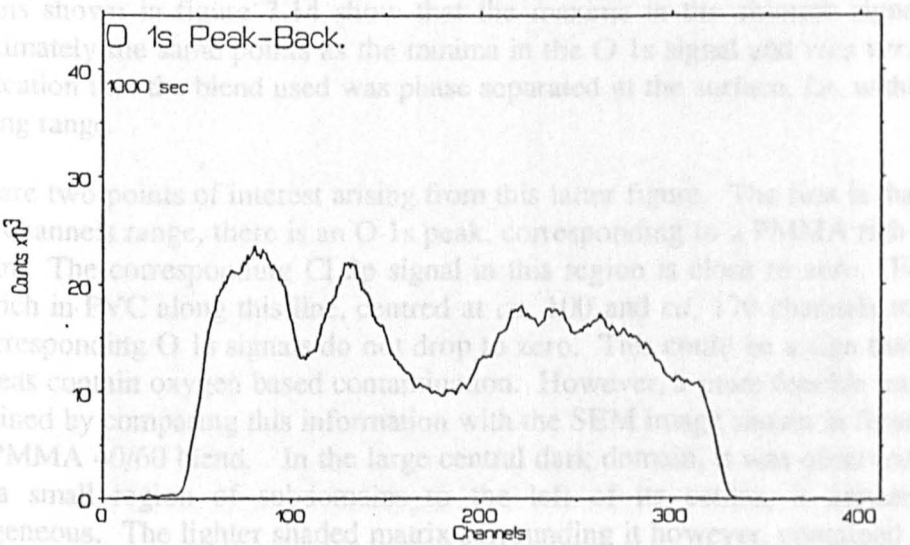

Figure 7.13: Scienta ESCA300 linescan of O 1s signal (peak-background) for PVC/PMMA 30/70 blend

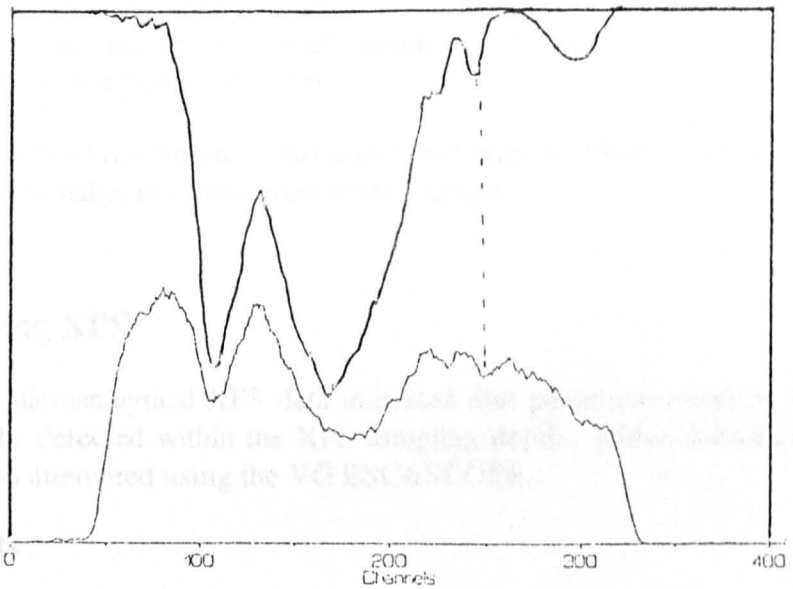

Figure 7.14: Scienta ESCA300 showing both O 1s and Cl 2p linescans (peak-background) for PVC/PMMA 30/70 blend

A comparison of the two signals along the line is shown in figure 7.14. Here, the Cl 2p linescan was rotated through 180°, laterally inverted and positioned above the O 1s linescan.

7.3.2.2 Discussion

Both the Cl 2p and O 1s linescans show maxima and minima. In the Cl 2p linescan (figure 7.12) the maxima indicate areas of the linescan which are rich in PVC. maxima in the O 1s linescan (figure 7.13) are areas which are rich in PMMA. The comparison of linescans shown in figure 7.14 show that the maxima in the chlorine signal occur at approximately the same points as the minima in the O 1s signal and *vice versa*. This is an indication that the blend used was phase separated at the surface, *i.e.* within the XPS sampling range.

There are two points of interest arising from this latter figure. The first is that in the 50 to 100 channels range, there is an O 1s peak, corresponding to a PMMA rich area in the linescan. The corresponding Cl 2p signal in this region is close to zero. For the two areas rich in PVC along this line, centred at *ca.* 100 and *ca.* 170 channels respectively, the corresponding O 1s signals do not drop to zero. This could be a sign that the PVC-rich areas contain oxygen based contamination. However, a more feasible interpretation is obtained by comparing this information with the SEM image shown in figure 7.4 for a PVC/PMMA 40/60 blend. In the large central dark domain, it was observed that apart from a small region of subdomains to the left of its centre, it appeared largely homogeneous. The lighter shaded matrix surrounding it however, contained many dark shaded microdomains. If the lighter shaded component was PVC and the darker component was PMMA, on the Scienta linescan it would be expected that for PMMA-rich areas, the Cl 2p signal would be negligible, whereas in PVC-rich areas, a significant O1s signal would still be observed. This is the behaviour shown in figure 7.14.

The second point of interest from this figure is indicated by the dashed line. This shows a small peak in the Cl 2p signal and corresponding trough in the O 1s signal, in what is essentially a PMMA-rich region. Again by comparing this with the SEM image in figure 7.4, this can be interpreted as a small region of PVC secondary domains contained within the PMMA-rich primary domain.

The maximum lateral resolution on this instrument was *ca.* 25μm. This did not allow for resolution of the smaller microdomains on this sample.

7.3.3 Imaging XPS

The previous microanalytical XPS data indicated that phase separation in PVC/PMMA blends could be detected within the XPS sampling depth. Direct chemical mapping of the surface was attempted using the VG ESCASCOPE.

7.3.3.1 Results

The ESCASCOPE images for a solution cast PVC/PMMA 80/20 blend are shown in this section. The peak minus background image for the Cl 2p signal is shown in figure 7.15.

The corresponding image for the O 1s signal is seen in figure 7.16.

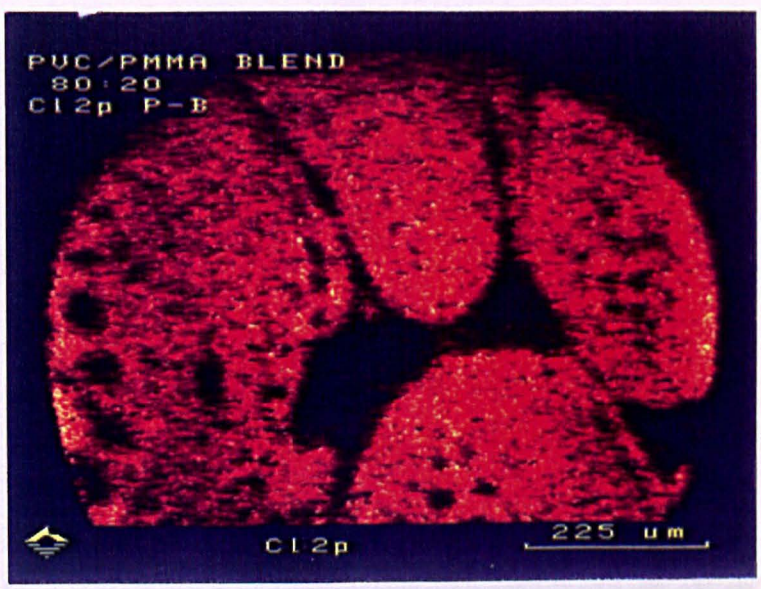

Figure 7.15: VG ESCASCOPE image of Cl 2p signal (peak-background) for PVC/PMMA 80/20 blend

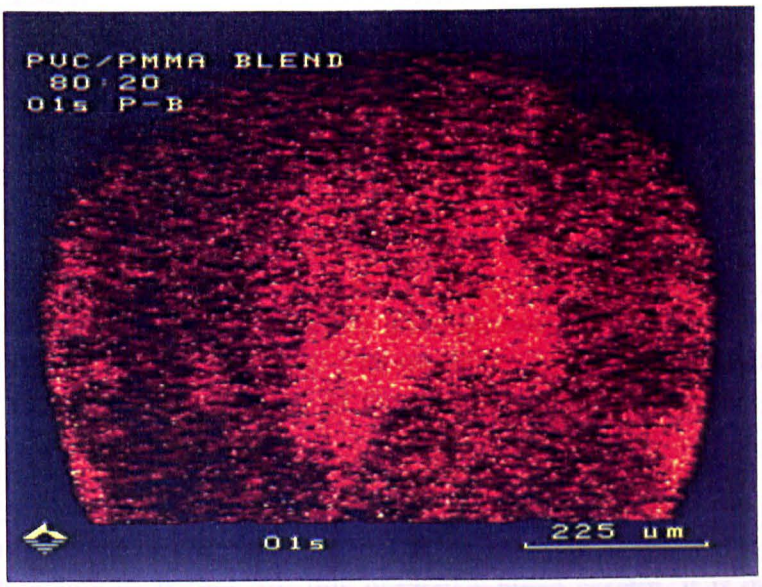

Figure 7.16: VG ESCASCOPE image of O 1s signal (peak-background) for PVC/PMMA 80/20 blend

The imaging software for the VG ESCASCOPE allows one image to be superimposed on the other. This is known as an "overlay image" and figure 7.17 shows the overlay of the Cl 2p and O 1s signals.

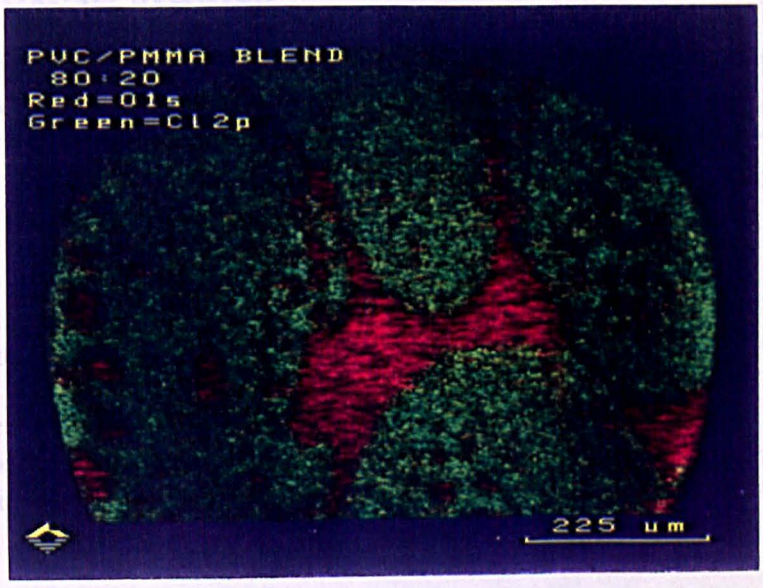

Figure 7.17: VG ESCASCOPE overlay image of Cl 2p and O 1s signals (peak-background) for PVC/PMMA 80/20 blend

7.3.3.2 Discussion

The spatial distribution of the Cl 2p signal in figure 7.15 is indicative of the spatial resolution of PVC. That for the O 1s signal as seen in figure 7.16 represents PMMA. The dark areas in each image corresponds with the light areas in the other. This is shown more distinctly in the overlay image, where the PMMA distribution is displayed in red and the PVC distribution is shown in green. There appears to be very little Cl 2p signal in PMMA rich areas, but much O 1s signal is seen in the PVC rich areas. Given the discussion of the previous section, this behaviour should be expected as it indicates that the PMMA-rich regions are largely homogeneous, whereas the PVC-rich regions contain many PMMA microdomains. The maximum lateral resolution of this instrument is of the order of *ca.* 10μm. Many of the PMMA microdomains had diameters below this value and were unresolved.

These results have shown that direct chemical mapping of phase separated polymer blends can be achieved within the sampling depth range of XPS. The main disadvantage of using this technique is that, for this particular blend system, it is destructive. Low power X-rays (100W) were used to acquire XP spectra throughout this study. This was because PVC is known to dechlorinate when irradiated by X-rays [104]. In addition to this, the heat produced by high power sources caused thermal damage to the PVC. In the ESCASCOPE imaging experiments, in order to obtain reasonably intense signals, the sample had to be irradiated for two hours using X-rays of power 510W. This caused considerable thermal degradation to the sample which manifested itself as discolouration, folding and wrinkling of the film.

7.4 ToFSIMS studies

A non-destructive alternative to ESCASCOPE imaging for phase separated PVC/PMMA blends was that of ToFSIMS imaging. In this section, a series of ToFSIMS images for blends across the composition range are presented, as well as various other images. The data presented here helps to further explain some of the observations made in previous sections.

7.4.1 Results

The negative ion ToFSIM spectrum for a PVC/PMMA 40/60 blend is shown in figure 7.18. Five peaks of interest are labelled, these being due to O^-, OH^-, CH_3O^-, $^{35}Cl^-$ and $^{37}Cl^-$. The first three peaks are due to PMMA and the latter two to PVC.

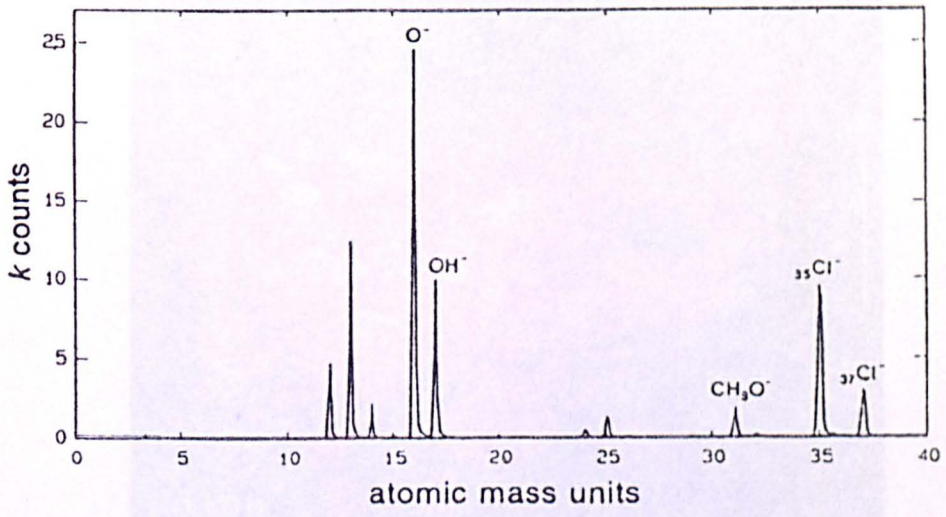

Figure 7.18: ToFSIM negative ion spectrum for an immiscible PVC/PMMA 40/60 blend

The spatial distribution of the m/z=35⁻ and 37⁻ peaks for a PVC/PMMA 40/60 blend was obtained at 200x magnification and is shown in figure 7.19.

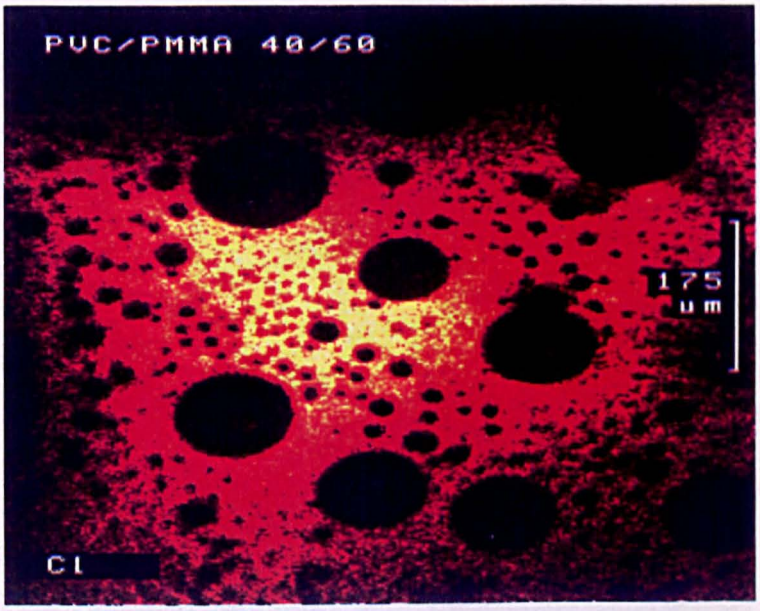

Figure 7.19: ToFSIMS Cl⁻ image for an immiscible PVC/PMMA 40/60 blend

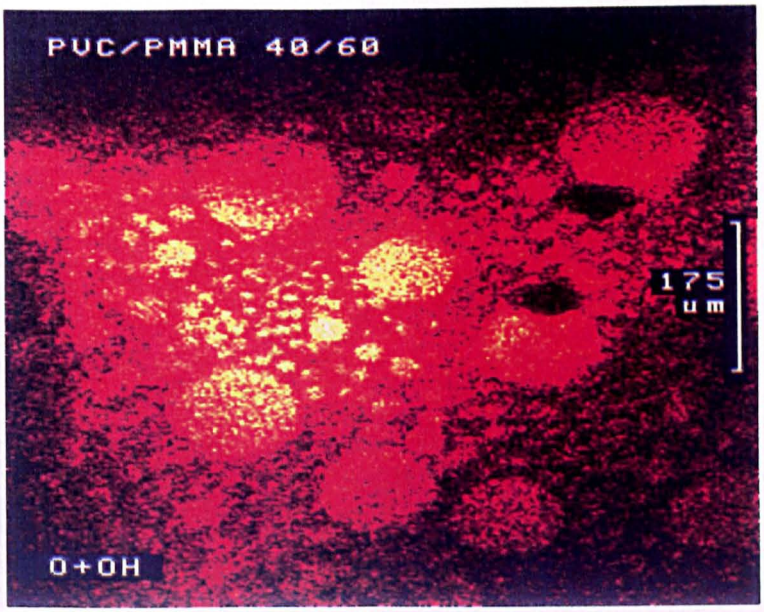

Figure 7.20: ToFSIMS O^-+OH^- image for an immiscible PVC/PMMA 40/60 blend

The spatial distribution of the O^- and OH^- ions at m/z=16^- and 17^- for the same area was also acquired and is shown in figure 7.20.

Assuming no oxygen containing contamination in either polymer, the Cl^- image is indicative of PVC and the O^-+OH^- image is due to PMMA. As for the VG ESCASCOPE, the VG ToFSIMS imaging software allows superimposition of one image onto the other. The overlay of the previous two images is shown in figure 7.21.

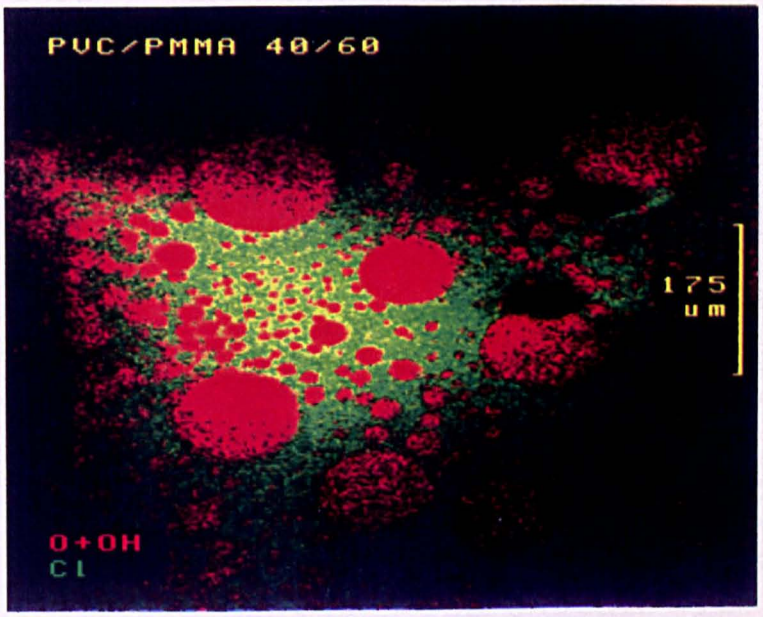

Figure 7.21: ToFSIMS negative ion overlay image for an immiscible PVC/PMMA 40/60 blend

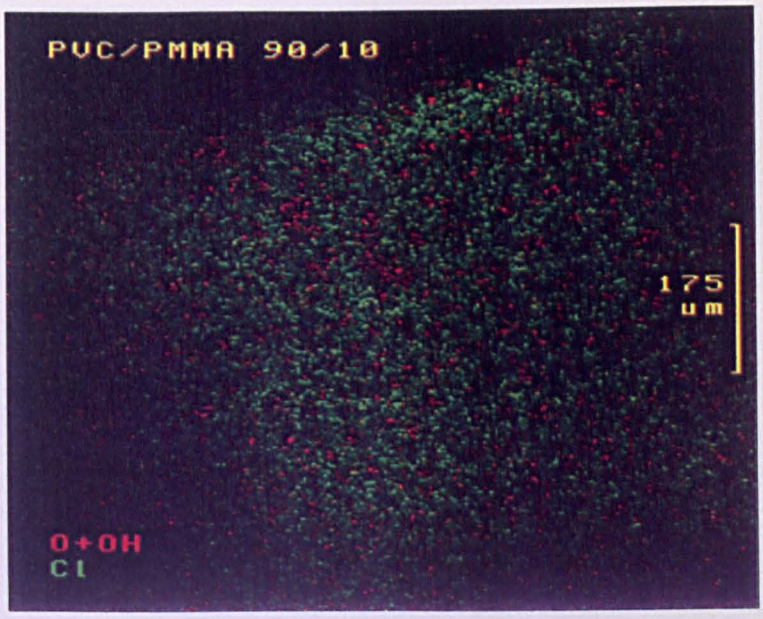

Figure 7.22: ToFSIMS negative ion overlay image for an immiscible PVC/PMMA 90/10 blend

Here the red areas are due to PMMA and the green areas are PVC. This first set of images has been shown for demonstration purposes. Except in a few cases, the remaining images in this chapter will be shown as overlay images of Cl^- and O^-+OH^- signals, the Cl^- being shown in green and the O^-+OH^- shown in red. Unless specified, all images were acquired at the film/air interface of the samples.

A series of negative ion images across the composition range were obtained (not

Figure 7.23: ToFSIMS negative ion overlay image for an immiscible PVC/PMMA 90/10 blend

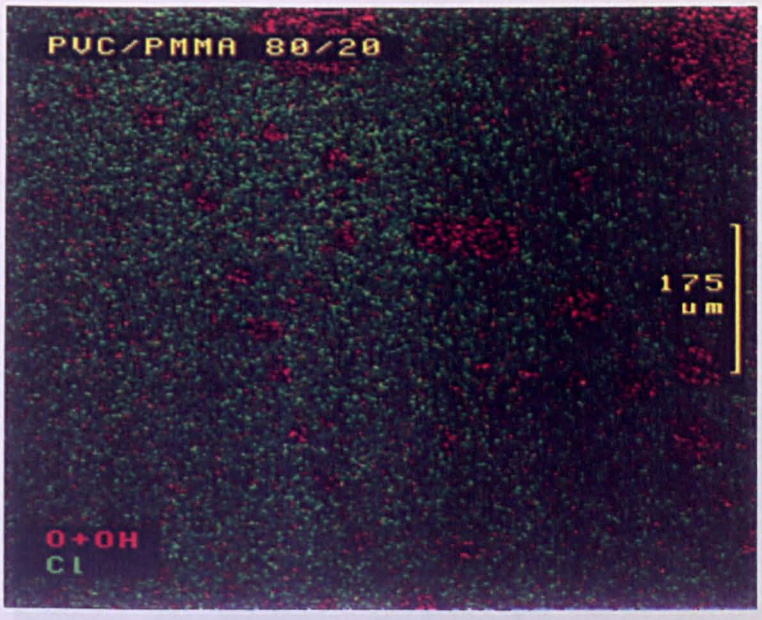

Figure 7.24: ToFSIMS negative ion overlay image for an immiscible PVC/PMMA 80/20 blend

including the homopolymers) at intervals of 10%. Figure 7.22 shows the overlay image for a PVC/PMMA 90/10 blend at 200x magnification. Figure 7.23 shows an image for the same blend at a magnification of 1000x.

An overlay image for a PVC/PMMA 80/20 blend is shown in figure 7.24 whilst that for a 70/30 blend is displayed in figure 7.25.

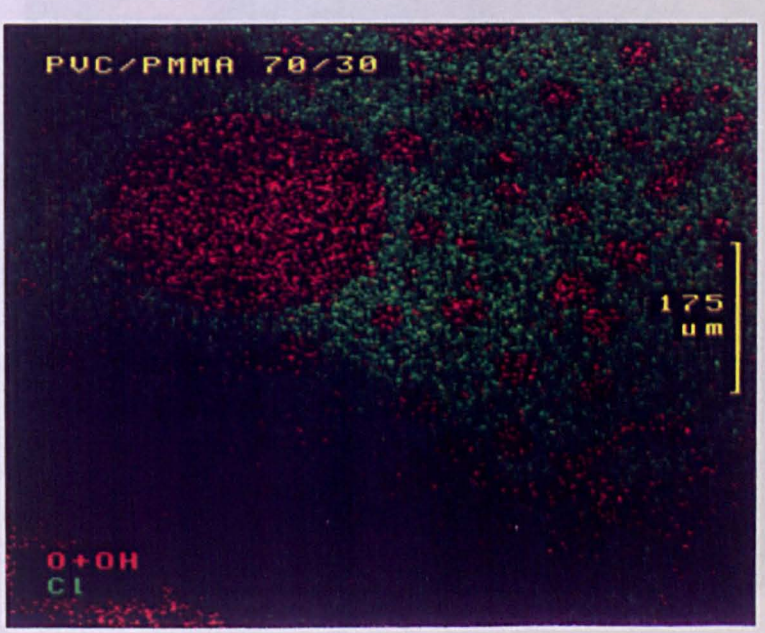

Figure 7.25: ToFSIMS negative ion overlay image for an immiscible PVC/PMMA 70/30 blend

Figure 7.26: ToFSIMS negative ion overlay image for an immiscible PVC/PMMA 60/40 blend

Figures 7.26 and 7.27 show the overlay images for the PVC/PMMA 60/40 and 50/50 blends respectively.

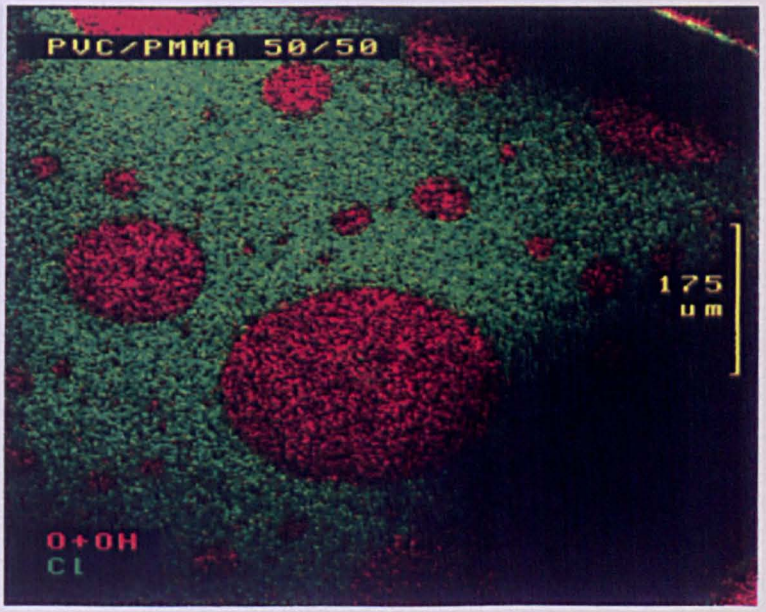

Figure 7.27: ToFSIMS negative ion overlay image for an immiscible PVC/PMMA 50/50 blend

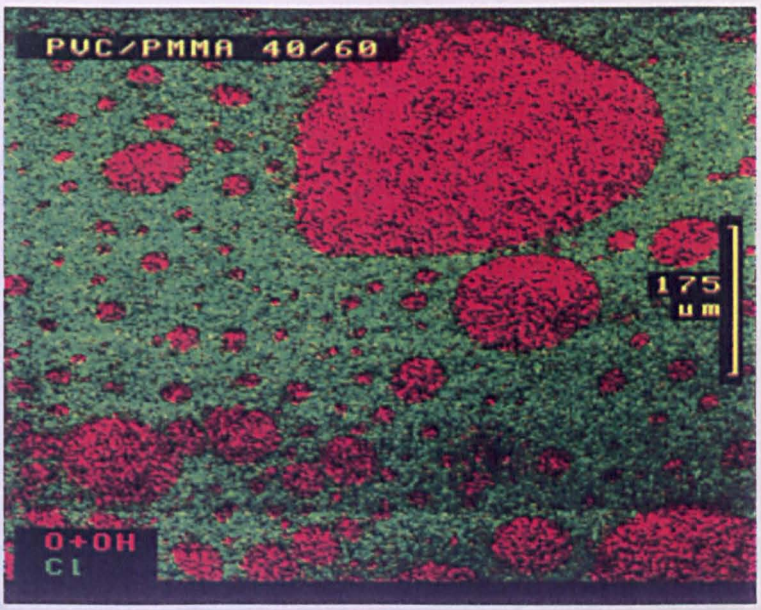

Figure 7.28: ToFSIMS negative ion overlay image for an immiscible PVC/PMMA 40/60 blend

Figures 7.28 and 7.29 were both acquired on the same area of a PVC/PMMA 40/60 blend. Figure 7.28 shows the overlay of Cl^- and O^-+OH^- images, whereas figure 7.29 displays the spatial distribution of the CH_3O^- ion.

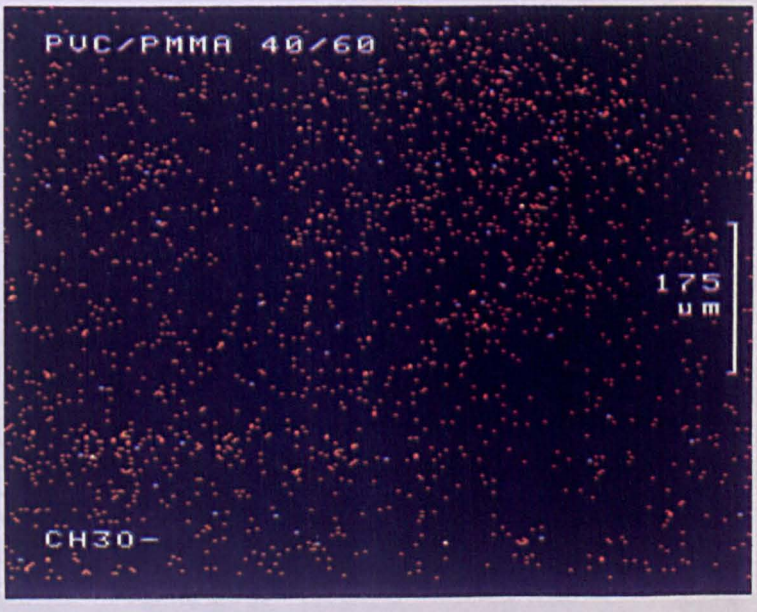

Figure 7.29: ToFSIMS CH_3O^- image for an immiscible PVC/PMMA 40/60 blend

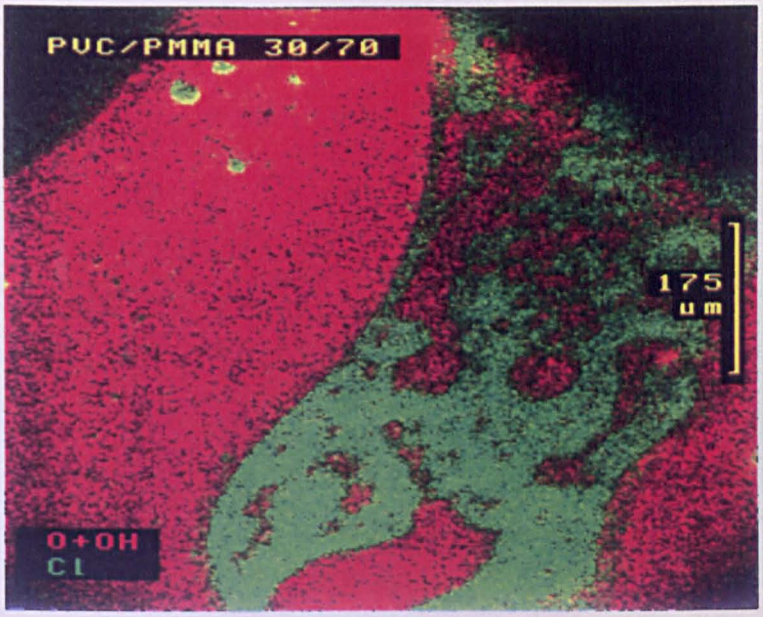

Figure 7.30: ToFSIMS negative ion overlay image for an immiscible PVC/PMMA 30/70 blend

Figure 7.30 shows the overlay image for a PVC/PMMA 30/70 blend, and figure 7.31 displays the image for a 20/80 blend.

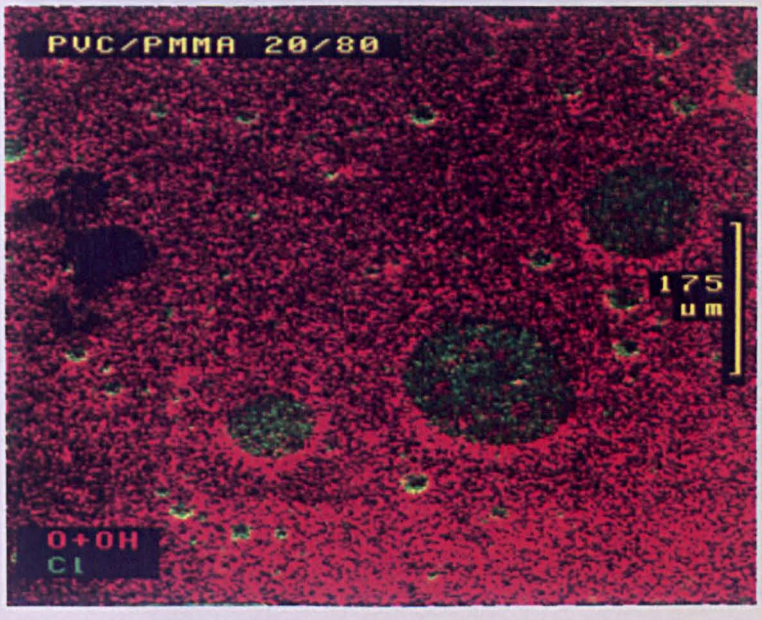

Figure 7.31: ToFSIMS negative ion overlay image for an immiscible PVC/PMMA 20/80 blend

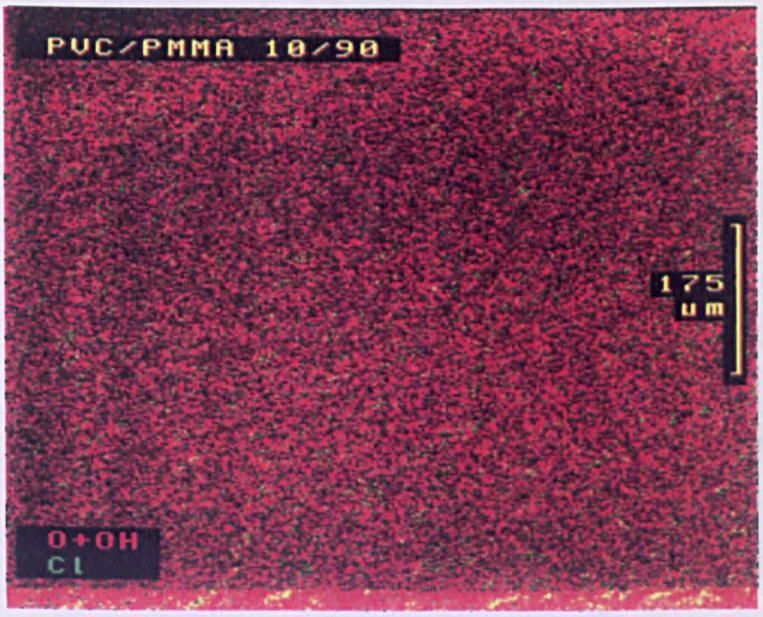

Figure 7.32: ToFSIMS negative ion overlay image for an immiscible PVC/PMMA 10/90 blend

Figure 7.32 and 7.33 show the overlay images for a PVC/PMMA 10/90 blend. The former is at a magnification of 200x while the latter is a 1000x magnification image.

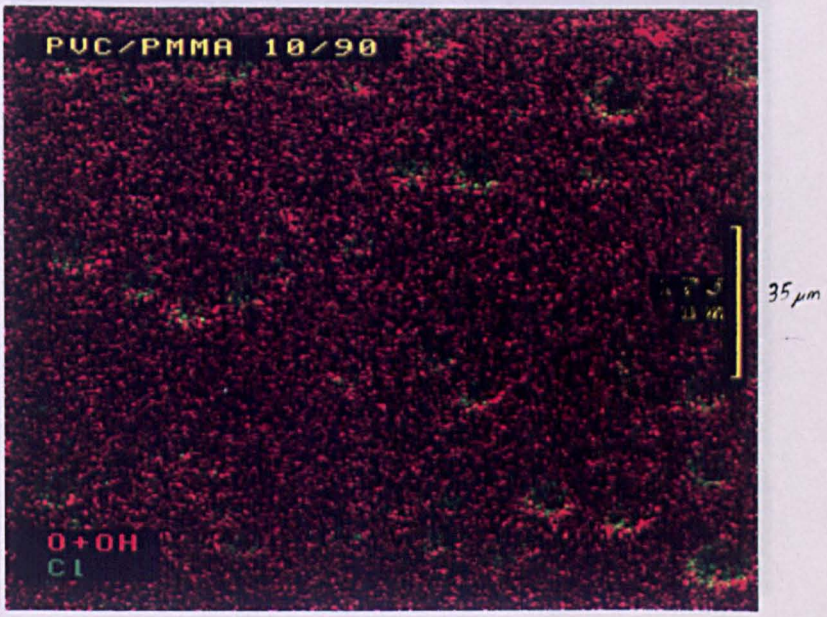

Figure 7.33: ToFSIMS negative ion overlay image for an immiscible PVC/PMMA 10/90 blend

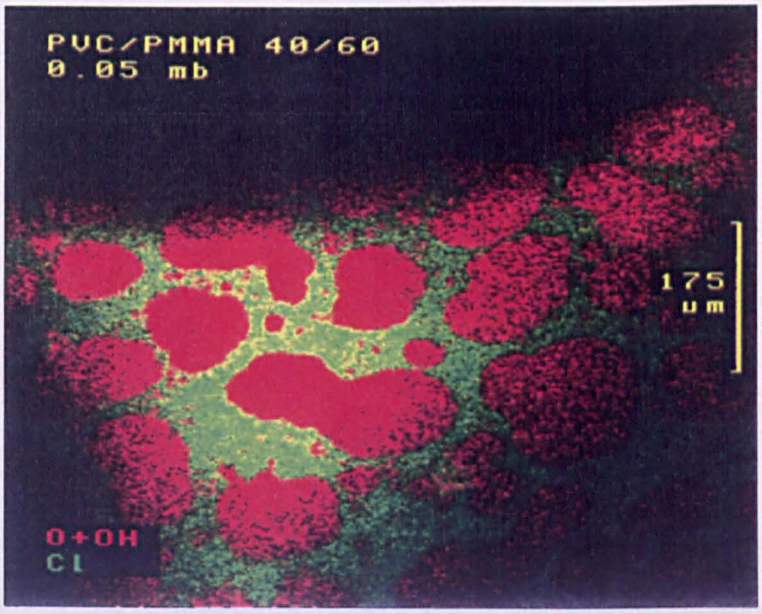

Figure 7.34: ToFSIMS negative ion overlay image for an immiscible PVC/PMMA 40/60 blend for which the solvent was removed at a pressure of $5x10^{-2}$ mb

The effects of solvent removal rate are shown in figures 7.34 and 7.35, both on a PVC/PMMA 40/60 blend. The sample imaged in figure 7.34 had its solvent removed in a vacuum oven at $5x10^{-2}$ mb. For the sample shown in figure 7.35, the pressure in the oven had been $1x10^{-2}$ mb. Both samples had had their solvent removed at room temperature.

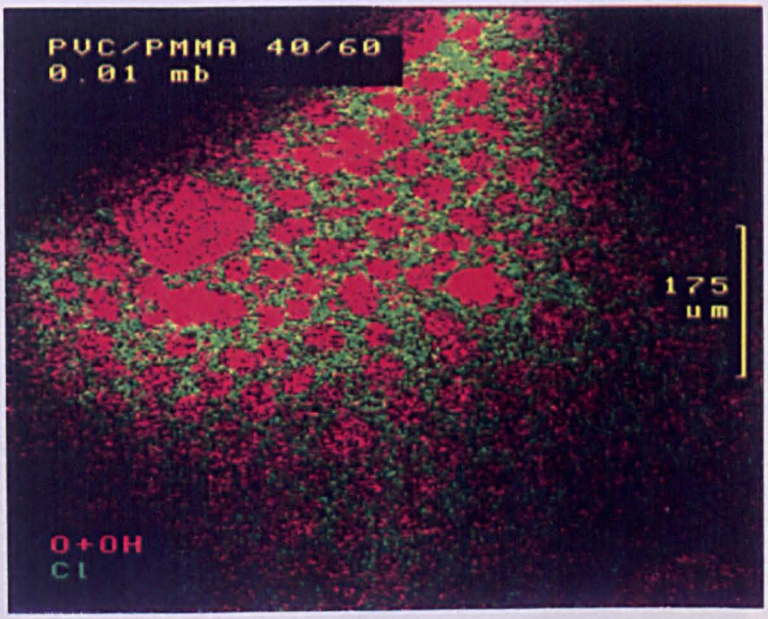

Figure 7.35: ToFSIMS negative ion overlay image for an immiscible PVC/PMMA 40/60 blend for which the solvent was removed at a pressure of $1x10^{-2}$ mb

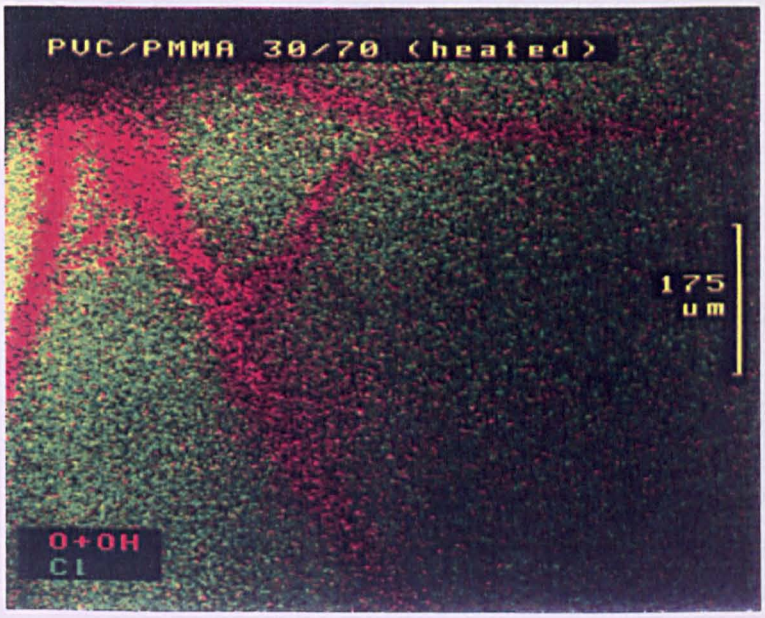

Figure 7.36: ToFSIMS negative ion overlay image for an immiscible PVC/PMMA 30/70 blend heated to 60°C during solvent removal

The effect of solvent removal temperature was examined. The sample whose overlay image is shown in figure 7.36, a PVC/PMMA 30/70 blend, had its solvent removed in a vacuum oven at 60°C.

Figure 7.37 shows the Cl^- image of a PVC/PMMA 50/50 blend which had been spin cast onto a silver coupon.

Figure 7.37: ToFSIMS Cl^- image for an immiscible PVC/PMMA 50/50 blend spin cast onto Ag

Figure 7.38: ToFSIMS negative ion overlay image for an immiscible PVC/PMMA 30/70 blend analysed at the film/glass interface

The images in figures 7.38 to 7.40 are of the same area of a PVC/PMMA 30/70 blend analysed at the film/glass interface. The overlay image of the Cl^- and O^-+OH^- signals is shown in figure 7.38. The Cl^- image is shown in figure 7.39.

Figure 7.39: ToFSIMS Cl^- image for an immiscible PVC/PMMA 30/70 blend analysed at the film/glass interface

Figure 7.40: ToFSIMS O^-+OH^- image for an immiscible PVC/PMMA 30/70 blend analysed at the film/glass interface

Figure 7.40 shows the O^-+OH^- image for the same area of film. Part of the negative ion spectrum for this area is shown in figure 7.42.

Finally, figure 7.41 shows the ToFSIMS overlay image of Cl^- and O^-+OH^- signals from a PVC/PMMA 30/70 blend, the same area that was analysed by optical and scanning electron microscopy in figures 7.2 and 7.3.

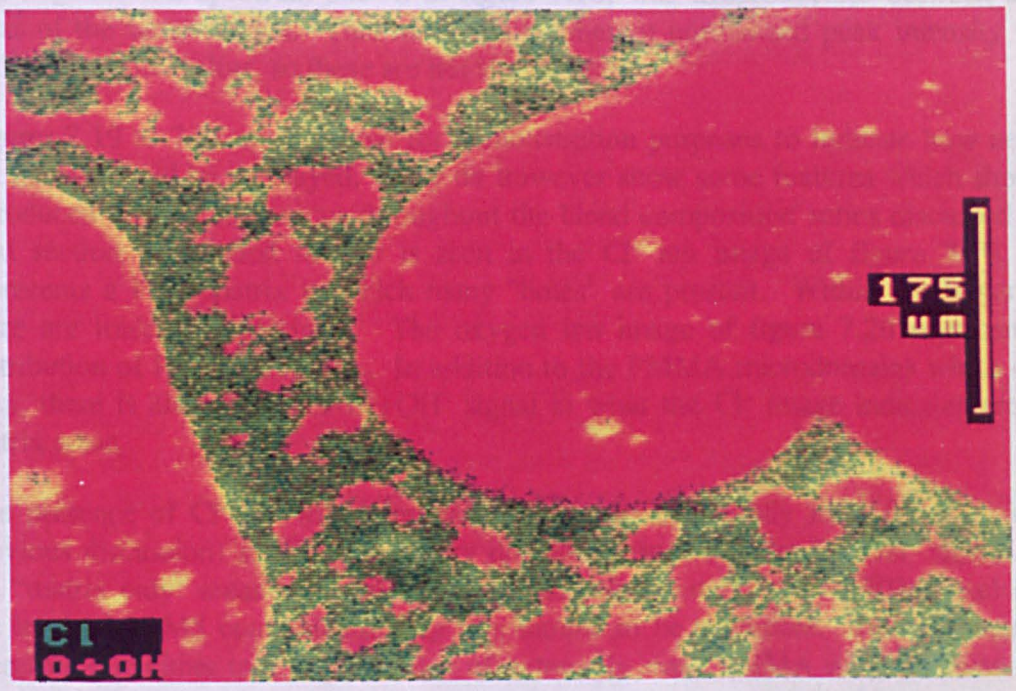

Figure 7.41: ToFSIMS negative ion overlay image for an immiscible PVC/PMMA 30/70 blend (same area as shown in figures 7.2 and 7.3)

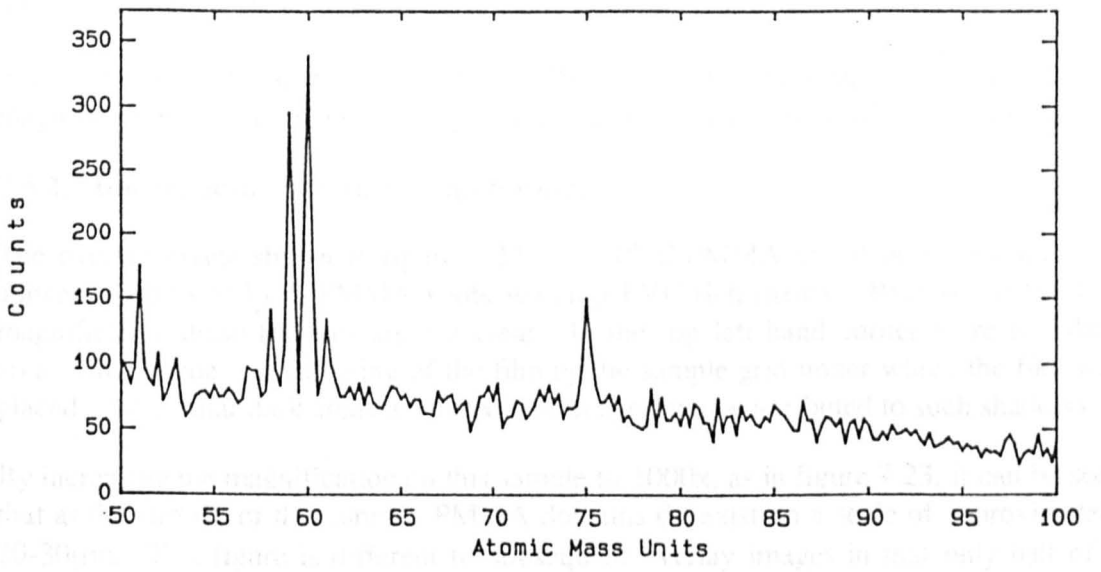

Figure 7.42: ToFSIM negative ion spectrum for an immiscible PVC/PMMA 30/70 blend analysed at the film/glass interface

7.4.2 Discussion

7.4.2.1 ToFSIMS imaging of PVC/PMMA blends

The negative ion spectrum shown in figure 7.18, was irreproducible between several areas of the same sample. This made for incoherent normalized peak intensity versus bulk composition plots, so these are not shown here.

Figures 7.19 to 7.21 were shown for demonstration purposes to indicate how negative ion images could be overlayed. They do however show some features which should be introduced now as they occur throughout the blend composition series discussed in the next section. The first feature is seen in the Cl^- ion image of figure 7.19. This represents a PVC matrix in which many "holes" are present. Within the larger holes there are traces of Cl^- signal. The oxygen ion image of figure 7.20 represents the distribution of PMMA domains. In addition to the PMMA microdomains which can be seen, there is also a weaker O^-+OH^- signal in what the Cl^- image indicates are PVC matrix areas.

The presence of Cl^- in PMMA primary domain areas is easily interpreted (given the previous discussion) as PVC secondary domain formation. The O^-+OH^- signal across the "matrix only" areas however are more difficult to interpret. ToFSIMS had shown the level of PDMS contamination for this sample to be negligible. This observation is therefore due either to a huge number of extremely small PMMA microdomains within the matrix area, or alternatively, a non-uniform overlayer of PMMA at the surface. These possibilities will be discussed more in the next section.

An additional feature is shown in figure 7.21 by the two dark areas to the left and to the upper left of the scale bar. These arise from topographical features, *i.e.* pits in the film.

For all images shown, a scale bar of 175μm indicates an image acquired at 200x magnification. For a scale bar of 35μm, the image was acquired at 1000x magnification.

7.4.2.2 Images across the composition range

The overlay image shown in figure 7.22 for a PVC/PMMA 90/10 blend, shows what appears to be small red PMMA spots within a PVC-rich matrix. Because of the low magnification these features are not clear. In the top left hand corner there is a dark area. This is due to shadowing of the film by the sample grid under which the film was placed. All similar dark areas in subsequent images can be attributed to such shadows.

By increasing the magnification on this sample to 1000x, as in figure 7.23, it can be seen that at the surface of this sample, PMMA domains do exist on a scale of approximately 20-30μm. This figure is different to subsequent overlay images in that only half of it contains imaging information. This was due to a software fault when imaging this specimen.

The phase separation at the surface of the PVC/PMMA 80/20 blend shown in figure 7.24 is more obvious at 200x magnification than for the previous blend. Here the PMMA domains have increased in size but the matrix is still PVC.

Increasing the concentration of PMMA to 30% increases the size of the PMMA domains, as shown in figure 7.25. Ignoring the very large domain in the top left hand side of the image, the average size of PMMA domains has increased to around 60μm. The large domain was focused upon using the ToFSIMS optical microscope when setting up the experiment, but none of the other domains could be seen. The large domain could also be seen with the naked eye, which suggests that this was a bulk rather than a strictly surface feature.

With an increase in PMMA concentration to 40%, figure 7.26 shows that the average size of the PMMA domains increase to *ca.* 80μm. The image shows two areas of increased brightness just above and below the centre of the image. This suggests that either the film was thicker at these points, or more likely, that the film had folded a little underneath the sample grid, causing these areas to raise.

In figure 7.27, the overlay image for a PVC/PMMA 50/50 blend, there is no average PMMA domain size as the size of the domains varied so much. What is clear however is that PVC still forms the matrix, and there are a lot more larger PMMA domains (which were also visible to the naked eye) than in previous samples. In the middle of the large central PMMA domain, a small green area may just be observed. This is a secondary PVC domain within a primary PMMA domain.

For the sample shown in figure 7.28, the PMMA concentration is increased to 60%. Despite this the PVC is still the dominant phase. The PMMA domains are highly irregular, in terms of average size, and for the larger domains, shape. The horizontal line towards the bottom of this image, which separates light and dark areas, was due to a fault with the imaging software.

The only non-overlay image of this series is shown in figure 7.29. This is the negative ion image of the CH_3O^- signal, a PMMA-unique ion, on the same sample area as shown in the previous figure. Although the signal is very faint, it can be seen that the areas in which the CH_3O^- is being detected correspond with the PMMA areas of figure 7.28. Due to the very low intensity of the CH_3O^- signal, this ion was not imaged in further experiments.

Figure 7.30 shows that for the PVC/PMMA 30/70 blend, in the area imaged, PMMA appears to be the dominant phase and very large, irregularly shaped domains are present. This suggests that at this composition, the blend is at or very near to the point of phase inversion. This is in broad agreement with Razinskaya's observations by SEM [89] who found that phase inversion took place at a PMMA concentration of between 75 and 80%.

For the PVC/PMMA 20/80 blend shown in figure 7.31, it is seen that phase inversion is complete, that PMMA forms the matrix, and that the PVC domains are now smaller and more regular in shape than in the previous sample.

Figure 7.32 shows the overlay image for the PVC/PMMA 10/90 blend. It is not immediately obvious at 200x magnification that PVC domains exist within a PMMA matrix. Increasing the magnification to 1000x however shows that this is indeed the case, and therefore, that every blend examined across the composition range was phase separated, and this phase separation could be imaged in each case by ToFSIMS.

7.4.2.3 Effects of solvent removal rate

It was known that the rate of solvent removal could dramatically affect the formation of the film (figures 7.4 and 7.5). For the full composition range discussed in the previous section, the pressure in the vacuum oven during solvent removal had ranged between $5\text{-}7\text{x}10^{-2}$ mb.

Figures 7.34 and 7.35 show the ToFSIMS overlay images for two different samples which had been prepared from the same solution, a PVC/PMMA 40/60 blend. The image in figure 7.34 is of a sample which had undergone solvent removal in a vacuum oven at a pressure of $5\text{x}10^{-2}$ mb. It can be seen that although some PMMA domains have merged, the larger domain diameters range from 60-150μm.

Figure 7.35 shows the image for a sample which had its solvent removed at $1\text{x}10^{-2}$ mb. The PMMA domains are now reduced in size and range in diameter (not including the large domain to the upper left of centre) from 10-30μm. Despite this the total PMMA coverage area does not seem that much different from the previous image.

It is clear that the more rapidly the solvent is removed from the sample, the smaller the average domain diameter of the dispersed phase. It is likely that no matter what solvent removal rate is used, phase separation will always be present. This is because for PVC/PMMA blends in the presence of THF, at PMMA concentrations below the phase inversion point, PMMA will tend to agglomerate. This will be further addressed in section 7.4.2.8. Providing the solvent removal rate is relatively low, these agglomerations can grow in volume. If the solvent removal rate however is relatively

high, the film will form more quickly and the associated increase in viscosity will inhibit the PMMA agglomerations from further growth.

Films which had their solvent removed in the fume cupboard, *i.e.* not in the vacuum oven, could not be imaged as they were not laterally homogeneous, which in the case of PVC/PMMA blends, was a pre-requisite for imaging of insulators.

7.4.2.4 Effects of temperature increase during solvent removal

The vast majority of solution cast blends in this study had their solvent removed at room temperature. In order to assess effects due to possible solvent entrapment in the films, a number of blends, after solvent removal, were heated to just above the boiling point of the solvent. For the miscible blends cast from butan-2-one, this annealing temperature was between 85-90°C. For the THF cast blends, this temperature was between 70-75°C. The only significant effect that this treatment had on the blends was to thermally degrade the PVC. This was indicated by discolouring of the films. No significant differences in surface behaviour either by XPS or ToFSIMS was observed. The only exception to this was in cases where PDMS contamination had been observed in the room temperature formed films. The annealed versions of these films showed an increase in PDMS contamination, which suggests that low molecular weight PDMS contaminants have greater mobility at high temperatures.

When the oven temperature was increased *during* solvent removal, differences in sample behaviour were observed. If oven temperatures were used above the boiling point of the solvent during solvent removal, highly non-uniform films resulted. Therefore, only solvent removal temperatures between room temperature and the boiling point of the solvents were used. For the miscible blends cast from butan-2-one, no significant differences in surface behaviour were observed between blends which had solvent removed at room temperature, and those for which solvent was removed at 75°C, just below the boiling point of butan-2-one. For immiscible blends, when the solvent removal temperature was increased to 60°C (just below the boiling point of THF), the films produced were still phase separated, but as can be seen in figure 7.36 which shows an overlay image of a PVC/PMMA 30/70 blend, more than one type of phase separation pattern is indicated. Within the green PVC matrix areas, there are many thousands of dispersed PMMA microdomains, as in previous images. However, there are also thick PMMA-rich bands which are interconnected across the sample. In accordance with the discussion on mechanisms of phase separation in chapter three (page 21) such interconnectivity is evidence of spinodal decomposition. For miscible PVC/PMMA blends, phase separation by this mechanism would not normally be expected until temperatures in excess of 150° were reached [91]. The phase separation effects observed are indicative of the PVC/PMMA/THF tertiary system. Further examination of this system by bulk analysis techniques was beyond the scope of this study.

7.4.2.5 Irreproducibility of data in spin cast blends

The irreproducibility in surface analysis results for solution cast blends was readily explained by considering phase separation effects in the bulk which continued to the surface.

For spin cast blends there was also irreproducibility in the XPS data, but due to the nature of the films, bulk analysis could not easily be performed. The ToFSIMS image shown in figure 7.37 gives an indication of why this irreproducibility was observed. It shows the Cl^- spatial distribution for a spin cast 50/50 blend. The O^-+OH^- image, not shown here, shows that these ions are detected from all areas of the sample. This was probably due to a mixture of PMMA and oxides on the silver substrate. The Cl^- image shows bright areas to the top of the image which are surrounded by streaky lines. These features are due to PVC. The bright areas at the top of the image are likely to be PVC which had very quickly precipitated onto the surface in the time between sample injection onto the substrate and spinning. The streaks are due to PVC precipitated from solution onto the substrate during the first few milliseconds of spinning. Even with such very rapid solvent removal, a phase separated film is produced. This is thought to be the cause of irreproducibility in the XPS data.

7.4.2.6 Surface analysis of blends at the film/glass interface

In section 7.3 the surface weight percentage of PMMA versus bulk composition plots as determined by XPS were discussed. The films had been solution cast directly into petri dishes, and after solvent removal, had been peeled away from the glass surface prior to analysis. The XPS data had suggested that there was evidence of oxygen containing contamination at high PVC concentrations.

Figure 7.38 shows the ToFSIMS overlay image for a PVC/PMMA 30/70 blend analysed at the film/glass interface. As usual, the green areas represent PVC and the red areas, PMMA. The "scratched" areas that can be seen are imprints from the petri dish. Looking at the Cl^- image in figure 7.39, it is seen that this matches with the green areas in the previous figure. The O^-+OH^- ion image shown in figure 7.40 however, does not correspond only to the red areas of the overlay image. The oxygen is distributed evenly across the whole sample area. The ToFSIM spectrum from this area shown in figure 7.42 is noisy, but it can be clearly observed that there are no $m/z=55^-$ or 85^- peaks, which would have indicated PMMA. The cluster of peaks centred at $m/z=60^-$ and the peak at $m/z=75^-$ are indicative of PDMS. None of the films in the blend series for which ToFSIMS images were earlier shown, had been washed with a non-solvent prior to reduce the level of PDMS contaminants, but none of these images had shown total coverage by oxygen and hydroxyl ions. From this it can be concluded that trace amounts of PDMS in immiscible PVC/PMMA blends preferentially migrated to the film glass interface. Such results were observed at the film/glass interface for films across the composition range. No ToFSIMS peaks were observed which suggested that oxygen containing contamination from the surface of the glass had transferred to the film.

The XP spectra used to obtain the ω versus bulk composition plots at the film/glass interface (figures 7.9 and 7.10) did not give Si 2p signals, so it is unlikely that the O 1s signals contained a contribution from PDMS. This would suggest that the PDMS detected by ToFSIMS was of monolayer coverage, reducing its detectability by XPS. It is possible that the O 1s signal across the composition range contained a contribution from residual solvent. This contribution would also have had corresponding contributions in the C 1s curve but these were indistinguishable from the polymer peaks. Looking at the form of the ω equation (page 54) it can be seen that a slight increase in

the O 1s peak due to such solvent contributions would reduce the $(C/O)_{blend}$ term. This in term would increase the ω value. The high values of ω shown by XPS for low concentrations of PMMA at the film/glass interface is therefore due to these additional oxygen containing contributions. This also explains the non-zero value of ω at 100% PVC.

7.4.2.7 Imaging bulk phase separation at the surface

In the bulk materials section shown earlier in this chapter, an optical micrograph and a scanning electron micrograph were shown of the same area of a PVC/PMMA 30/70 sample (figures 7.2 and 7.3 respectively). The ToFSIMS overlay image of this area is shown in figure 7.41. This series of three images gives a direct comparison of phase separation in the bulk and that at the surface. It is clear that the phase separation in the surface is of the same lateral resolution as that which occurs in the bulk. The comparison of ToFSIMS images with those from bulk sensitive techniques shows that bulk phase separation of large scale features in PVC/PMMA blends prepared in this way, can continue to the surface without being distorted by surface energy effects, with an apparent "vertical" morphology from bulk to surface. This explains the previous observation by XPS on studies of the same sample, that there is no difference in composition shown by spectra taken at 60° and 30° take-off angles, because from the outermost surface down to the bulk, there is no major compositional variation.

7.4.2.8 Possible reasons for PMMA surface adsorption in immiscible blends.

Throughout the XPS results and ToFSIMS images, it has been observed that for immiscible PVC/PMMA blends, there is a large amount of PMMA at the surface. It is possible that this could be due, in the absence of specific interactions between the two polymers, to the small difference in surface free energies. If this were the case it is likely that the PMMA would be able to form a continuous overlayer at the blend surface. This was *not* observed in any of the experiments performed on these blends. The more feasible reason for the observation of PMMA surface excess is that it is an effect due to a difference in specific gravities of the materials. The manufacturers quote a specific gravity for PVC as 1.42 g cm^{-3}, and that for PMMA as 1.18 g cm^{-3}. These values are within the ranges quoted by Brandrup and Immergut [105] which for PVC is 1.35-1.43 g cm^{-3} and for PMMA is 1.15-1.195 g cm^{-3}. When the film is forming, still in a low viscosity state, demixing occurs. It is believed that this is because THF preferentially interacts with PVC, to the exclusion of PMMA. At blend compositions in which PVC forms the matrix, PMMA forms agglomerates, as previously discussed. Sometimes these can be very large (as in figure 7.4), depending on the solvent evacuation rate used, but mostly, they will be small microdomains within the matrix. Density differences between these PMMA agglomerates and the PVC matrix drive the PMMA to the surface. It is unlikely that these domains exist through the bulk of the material. For the larger primary domains however, comparison of the bulk images with the surface images suggest that they can be present through the whole of the material.

7.4.2.9 The sampling depth for elementals by ToFSIMS analysis

Throughout this discussion on ToFSIMS images it has been assumed that the information depth for elemental ions has been in the region of 1nm. This was the

analysis depth quoted for SSIMS analysis for elementals by Hearn *et al* [65] using a 4keV ion source. In the present study, a 30keV ion source was used. There was a severe lack of imaging information obtainable from the CH_3O^- ion (figure 7.29) yet the intensity of this ion in ToFSIM spectra was not insignificant, compared to the elementals, as seen in figure 7.18. This raises doubts as to whether the imaging of elementals in this way gave a true representation of the outer monolayer, *i.e.* it is possible that because of the very high energy of the primary ions, the collision cascade process within the material could have allowed oxygen and chlorine to be sputtered from a depth greater than 1nm below the surface, despite the total ion dose being within static SIMS regime limits. This possibility has not been examined during the course of this study, but should be addressed in future work.

CHAPTER EIGHT - Conclusions

A surface analysis study using XPS and ToFSIMS has been performed on PVC, PMMA and their miscible and immiscible blends.

From ToFSIMS studies on different areas of a sample of PMMA, the method of normalization of peak intensities (NPI's) for partial quantification of spectra was assessed. It was found that for elemental and quasi-elemental ions, a standard error in NPI of ±2% could be expected. For molecular ions this was increased to ±5%, providing an appropriate normalizing range was chosen.

For homo-PVC and homo-PMMA, NPI-ion dose profiles were obtained for specific ions, for the ion dose range $2x10^{10}$ - $2x10^{14}$ ions cm^{-2}. From this it was shown that the fragmentation routes of secondary ions with similar NPI-ion dose profiles could be related, and that the limit of the static SIMS regime is not at a fixed point, but is dependent on the specific ion being observed. The formation of poly(cyclic aromatic) (PCA) ions was shown to be in evidence at the lowest ion doses examined. An increase in NPI for PCA ions corresponded with a decrease in NPI for ions unique to the homopolymers. The maximum NPI for PCA ions was observed at *ca.* $7x10^{13}$ ions cm^{-2}, beyond which the sample surface resembled that of graphite.

Studies on miscible PVC/PMMA blends by XPS showed that there was a slight surface enrichment of PMMA across the blend composition range, probably due to differences in surface free energies of the homopolymers. ToFSIMS showed that this enrichment did not manifest itself as an overlayer of PMMA. The partial quantification method used for ToFSIMS did not show the surface enrichment observed by XPS. This is an anomoly between the quantitative technique used for the XPS data and the partially quantative ToFSIMS NPI method,which requires further investigation.

An ion at m/z=51$^-$ was assigned to ClO^-, arising from both PVC and PMMA. The NPI of this ion reached a maximum near the middle of the bulk composition range. It is possible that the formation of this ion involves sputtering of one species from beneath the surface, followed by combination with the other species at the surface.

Studies on immiscible PVC/PMMA blends showed by XPS that there was surface enrichment of PMMA at the film/air interface. The extent of surface enrichment was irreproducible on different samples of the same composition. ToFSIMS imaging was used to map the spatial distribution of PVC and PMMA specific ions. It was found that phase separation in the bulk of the material could continue to the ToFSIMS sampling depth for elemental ions. Phase separation was detected by ToFSIMS in each film across the blend composition range. This explained the irreproducibility in the XPS

data. The PMMA surface enrichment was never observed to manifest itself as a PMMA overlayer, and was probably more an effect of a difference in specific gravities, rather than a difference in surface free energies. The domain size of the dispersed phase in these blends was found to be a function of the rate of solvent removal. The greater this rate, the smaller the domain size.

At the film/glass interface for solution cast films, ToFSIMS showed an overlayer of PDMS not detectable by XPS. The latter technique did however show an excess of oxygen, possibly due to residual solvent.

This study was the first to show that phase separation in polymer blends can be imaged using ToFSIMS. Comparison of ToFSIMS imaging with microanalytical and imaging XPS, has shown the ToFSIMS technique to be superior both in terms of lateral resolution and in its non-destructive nature for samples that are susceptible to thermal degradation. However, throughout the course of this study, doubts have been raised regarding the surface sensitivity of ToFSIMS for elemental ions using a 30keV source.

CHAPTER NINE - Further Work

For ToFSIMS experiments this study has shown that there is a distinct possibility that elemental ions are sputtered from below the outer surface monolayer. This possibility needs to be examined by comparative ToFSIMS and angular dependent XPS studies.

The method of normalised peak intensities for partial quantification of SSIMS spectra needs re-examination and fine tuning. A suitable starting point would be to acquire ToFSIM spectra for miscible PVC/PMMA blends for very low and very high concentrations of PMMA. The NPI-bulk composition plots for elementals in these regions deviate from linearity. Further investigation on such samples may explain such deviations and allow for better correlation with XPS data.

It was acknowledged that the NPI-ion dose profile data presented here was not of the highest standard. This was due to instrument problems and time limitations. A repeat experiment on both PMMA and PVC for ion doses between $2x10^{10}$ and $2x10^{14}$ ions cm^{-2} would be beneficial. Magnification steps could be eliminated by (a) using a fixed magnification of 500x, and (b) adjusting the primary ion pulse width from 5ns at low ion doses to 50ns at high ion doses.

The blend examined in this study was amorphous. Further examination of blend surfaces could include blends in which one of the components was partially crystalline. The effect of varying the molecular weight in the components would also be of interest.

This study has shown that advanced spectroscopies may be used to make observations on surface chemistries in the outer few molecular layers of polymer blends. The most obvious next step would be to attempt to correlate experimental data with theoretical models. Data obtained from this study or similar studies could be used to support thermodynamical modelling of surface behaviour in polymer blends. A particularly fruitful line of investigation would be to develop a model based on the Flory-Huggins lattice theory, with the introduction of an additional term to describe the effect of surface free energies of the components.

APPENDICES

Appendix A: XPS curve fitting

For curve fitting of XPS peaks using VGS5250 software, a synthesis envelope is used, the form of which was originally devised by Ansell *et al* [106]. The peak is fitted with a function that takes into account a total of seven parameters: peak centre, peak height, peak width, Gaussian/Lorentzian peak shape mixing ratio, constant tail height, Exponential tail height, and constant/exponential tail height mixing parameter. The function is

$$f(x) = H(GL + T(1 - GL)) \qquad ...(A1)$$

where T is the tail function, defined by

$$T = TM.CT + (1 - TM)\exp(-D.ET), \qquad ...(A2)$$

CT being the constant tail ratio, ET the exponential tail ratio, TM the tail mixing ratio and D the separation from the peak centre in channels. Back in equation A1, H is the peak height and GL is the Gaussian/Lorentzian product function, given by

$$GL = \frac{1}{[1 + M(x - x_0)^2/\beta^2]\exp\{(1 - M)[\ln 2(x - x_0)^2]/\beta^2} \qquad ...(A3)$$

in which M is the mixing ratio (1 for Lorentzian, 0 for Gaussian), x is the binding energy value, x_0 is the peak centre, and β is *ca.* 0.5 of the full width at half maximum.

The background is taken to be linear and this is subtracted before fitting. For the synthesis to take place at least one peak must be defined, *i.e.* a peak centre, height, width and associated tailing parameters.

Appendix B: The VG Scientific ESCASCOPE

The VG Scientific (now Fisons Surface Science) ESCASCOPE [107] is a combined high energy resolution XPS/imaging XPS instrument. A schematic representation of the instrument is shown in figure A.1. The main ways in which it differs from conventional XPS instruments are two-fold, and results from the electrostatic lens and detector arrangement. Firstly, the high resolution capability arises from the first two lenses in the primary lens column. These will only allow photoelectrons within a highly defined energy range to enter the analyser. Spectra are detected at the channeltron arrangement at the rear of the analyser.

Secondly, unlike most analysers, the channeltrons are arranged so that there is an "exit slit" at their centre. This is to facilitate imaging and it works with the help of lenses 3 and 5, the analyser itself acting as the fourth lens: as the photoelectrons pass through the third lens they are spatially orientated in a Fourier transform of the spatial orientation of the atoms from which they were emitted. This Fourier transform orientation is maintained through the analyser and is passed through the channeltron gap. Lens 5 reorientates the photoelectrons and focuses them onto a two-dimensional image detector. The image detected here is thus a real, erect two-dimensional representation of the surface.

During image acquisition, two-dimensional images of the spatial orientation of a particular core level can be made by tuning the analyser to accept only those photoelectrons which have the peak binding energy. The analyser is then retuned to accept photoelectrons with an appropriate background energy, the chosen background being as close to the peak as possible. The acquisition times for peak and background must be equal. When the acquisition is completed, the data system allows manipulation of the images such that the background image can be subtracted from that of the peak. This leaves an image which is due only to core level photoelectrons.

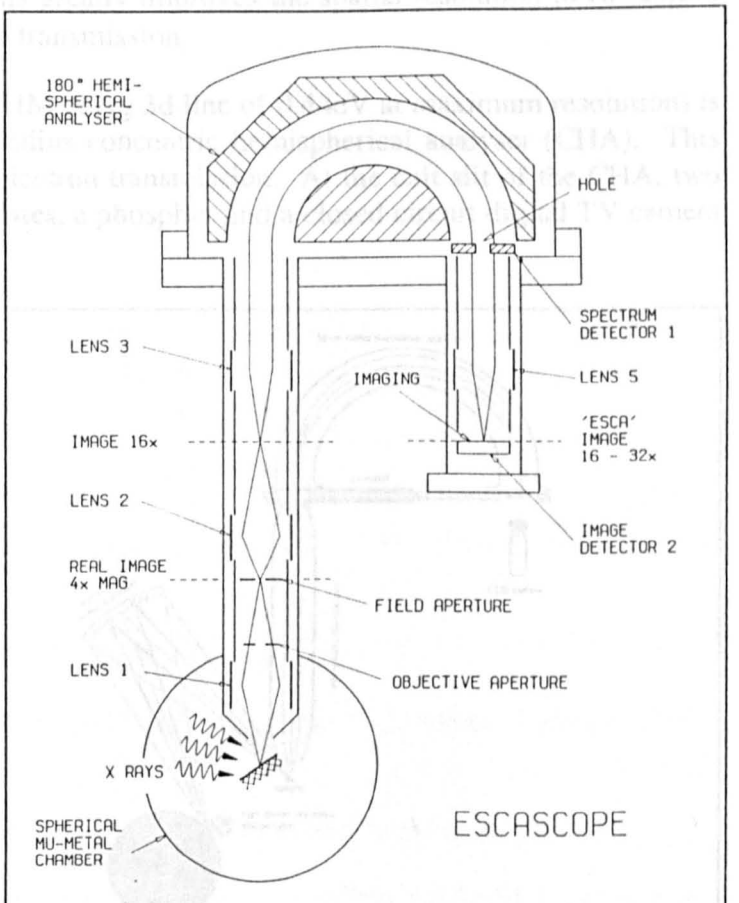

Figure A.1: Schematic diagram of the VG ESCASCOPE (after Adem *et al* [107])

Appendix C: The Scienta ESCA 300

The Scienta ESCA 300 instrument [108], developed at the University of Uppsala, Sweden, is a combined high energy resolution/microanalysis XPS instrument. A schematic diagram of the Scienta is shown in figure A.2. This instrument combines a high power rotating anode X-ray source with a crystal monochromator, high transmission electron optics which allow for linescan imaging, a multichannel detector and a sophisticated data collection system.

The 300mm diameter aluminium anode is rotated at 10,000rpm and the maximum electron beam power used is 8kW. Al$K\alpha$ X-ray radiation is then collected by the monochromator, a series of toroidal quartz crystals, and directed onto the sample. The monochromator virtually eliminates Brehmsstrahlung radiation from the Al$K\alpha$ emission spectrum to leave a single intense X-ray line of energy 1486.7eV with a line width of 0.35eV.

The electrostatic column is operated in high transmission or high spatial resolution mode. For the former mode, the column acts as a finely focusing single lens, the spatial resolution being relatively poor at 500µm. For the latter mode, a pre-lens is placed in position which only allows electrons from a small part of the X-ray line to be accepted into the main lens. This greatly improves the spatial resolution to *ca.* 25µm, but at the cost of greatly reduced transmission.

The high energy resolution (FWHM at Ag 3d line of 0.44eV at maximum resolution) is largely due to a 300mm mean radius concentric hemispherical analyser (CHA). This also allows for improved photoelectron transmission. At the exit slit of the CHA, two 40mm diameter microchannel plates, a phosphor and a closed circuit digital TV camera make up the detector assembly.

Microanalysis can be performed with this instrument in the form of linescans of a particular core line. The CCD camera in this mode is rotated through 90° so it can move along the axis of the X-ray slit. The software can then be set to only allow the entry of particular core electrons into the analyser. The intensity of this core line can then be recorded by the camera as a function of distance along the sample.

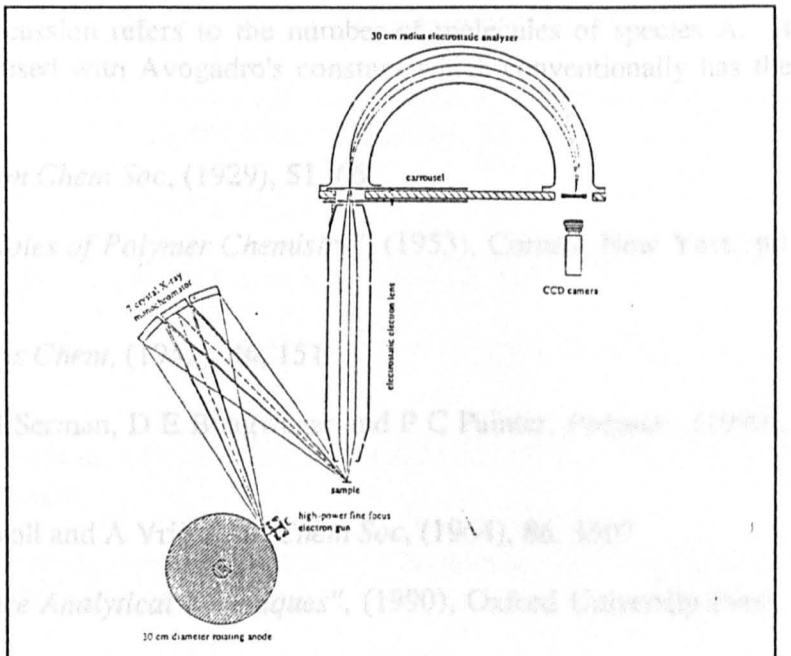

Figure A.2: Outline of the Scienta ESCA300, after Beamson *et al* [108]

REFERENCES

1. R A Emmett, *Ind Eng Chem*, (1944), **36**, 730

2. E Badum, US Patent 2,297,194 (1942)

3. E P Cizek, US Patent 3,383,435 (1968)

4. M L Fernandez, *Sci Progress*, (1990), **74**, 257

5. O Olabisi, L M Robeson and M T Shaw in *"Polymer-Polymer Miscibility"*, (1979), Academic Press, New York, pp 19-104

6. D K Carpenter in *"The Encylclopedia of Polymer Science and Engineering: Volume 15"*,(1989), Wiley, New York, pp 419-481

7. R A Orwoll in *"The Encyclopedia of Polymer Science and Engineering: Volume 15"*,(1989), Wiley, New York, pp 380-402

8. J W Gibbs, *Trans Conn Acad Arts Sci*, (1873), **2**, 309

9. N_A used in this discussion refers to the number of molecules of species A. It should not be confused with Avogadro's constant which conventionally has the same notation.

10. J H Hildebrand, *J Am Chem Soc*, (1929), **51**, 66

11. P J Flory in *"Principles of Polymer Chemistry"*, (1953), Cornell, New York, pp 495-548.

12. M L Huggins, *J Phys Chem*, (1942), **46**, 151

13. M M Coleman, C J Serman, D E Bhagwagar and P C Painter, *Polymer*, (1990), **31**, 1187

14. P J Flory, R A Orwoll and A Vrij, *J Am Chem Soc*, (1964), **86**, 3507

15. J C Riviere, *"Surface Analytical Techniques"*, (1990), Oxford University Press, Oxford

16. P D Innes, *Proc R Soc*, (1907), **A79**, 442

17. E Rutherford, *Phil Mag*, (1914), **28**, 305

18. P Auger, *J Phys Radium*, (1925), **6**, 205

19. K Siegbahn, C N Nordling, A Fahlman, R Nordberg, K Hamrin, J Hedman, G Johansson, T Bermatk, S E Karlsson, I Lindgren and B Lindberg,*"ESCA: Atomic, Molecular and Solid State Structure studied by means of Electron Spectroscopy"*, (1967), Almqvist and Wiksells, Uppsala.

20. J C Riviere in *"Practical Surface Analysis: 2nd Edition, Volume 1"*, (1991), Wiley, Chichester, p71 Eds D Briggs and MP Seah

21. D Briggs and J C Riviere in reference [20], p114

22. L C Lopez, D W Dwight and M B Folk, *Surf Interface Anal*, (1986), **9**, 405

23. D Briggs in reference [20], p443

24. J J Thomson, *Phil Mag*, (1910), **20**, 252

25. K S Woodcock, *Phys Rev*, (1931), **38**, 1696

26. R F K Herzhog and F Viehbok, *Phys Rev*, (1949), **76**, 855

27. R E Honig, *J Appl Phys*, (1958), **29**, 549

28. A Benninghoven, *Phys Status Solidi*, (1969), **34**, K169

29. M J Hearn, *PhD Thesis*, (1988), Leicester Polytechnic, pp39-61

30. D Briggs, A Brown and JC Vickerman, *"Handbook of Static Secondary Ion Mass Spectrometry (SIMS)"*, (1989), Wiley, Chichester, p6

31. C W Magee, *Int J Mass Spec Ion Phys*, (1983), **49**, 211

32. W P Poschenrieder, *Int J Mass Spec Ion Phys*, (1972), **9**, 357

33. B A Mamyrin, V I Kartaev, D V Schmikk and V A Zagulin, *Sov Phys - JETP*, (1973), **37**, 45

34. D T Clark and A Harrison, *J Polym Sci Polym Chem Ed*, (1981), **19**, 1945, and papers referenced therein

35. A Dilkes in *"Electron Spectroscopy - Theory, Techniques and Applications, Volume 4"* Eds C R Brundle and A D Baker, (1981), Academic Press, London

36. G Beamson and D Briggs, *"High Resolution XPS of Organic Polymers: the Scienta ESCA 300 Database"*, (1992), Wiley, Chichester

37. G Beamson, D T Clark, J Kendrick and D Briggs, *J Electron Spectrosc Relat Phenom*, (1990), **52**, 747

38. G Beamson and D Briggs, *Mol Phys*, (1992), **76**, 919

39. D Briggs and G Beamson, *Anal Chem*, (1992), **64**, 1729

40. W A Zisman, *Ind Eng Chem*, (1963), **55**, 18

41. A K Sha'aban, S McCartney, N Patel, I Yilgor, J S Riffle, D W Dwight and J E McGrath, *Polym Preprints*, (1983), **24**, 130

42. N M Patel, D W Dwight, J L Hedrick, D C Webster and J E McGrath, *Macromolecules*, (1988), **21**, 2689

43. Y Tezuka, H Kazama and K Imai, *J Chem Soc Faraday Trans*, (1991), **87**, 147

44. Li and B Huang, *Polym Bulletin*, (1988), **20**, 531

45. R L Schmitt, J A Gardella, L Salvati, *Macromolecules*, (1986),**19**, 648

46. H R Thomas and J J O'Malley, *Macromolecules*, (1979), **12**, 323

47. J J O'Malley, H R Thomas and G M Lee, *Macromolecules*, (1979), **12**, 996

48. L H Lee, *Adv Chem Ser*, (1968), **87**, 106

49. D H K Pan and W M Prest Jr, *J Appl Phys*, (1985), **58**, 2867

50. D D Davies and T K Kwei, *J Polym Sci Polym Phys Ed*, (1980), **18**, 2337

51. A Lobard and D Patterson, *Macromolecules*, (1977), **10**, 1021

52. Q S Bhatia, D H Pan and J T Koberstein, *Macromolecules*, (1988), **21**, 2166

53. H J Busscher, W Hoogsteen, L Dijkema, G A Sawatsky, A W J van Pelt, H P de Jong, G Challa and J Arends, *Polym Commun*, (1985), **26**, 252

54. J J Schmidt, J A Gardella Jr and L Salvati Jr, *Macromolecules*, (1989), **22**, 4489

55. D Briggs and A B Wooton, *Surf Interface Anal*, (1982), **4**, 109

56. J A Gardella and D M Hercules, *Anal Chem*, (1980), **52**, 226

57. D Briggs, *Surf Interface Anal*, (1982), **4**, 151

58. D Briggs, *Surf Interface Anal*, (1983), **5**, 113

59. D Briggs, M J Hearn and B D Ratner, *Surf Interface Anal*, (1984), **6**, 184

60. D Briggs and M J Hearn, *Spectrochimica Acta*, (1985), **40B**, 707

61. D Briggs and M J Hearn, *Int J Mass Spec Ion Proc*, (1985), **67**, 47

62. D Briggs, *Surf Interface Anal*, (1986), **8**, 133

63. D Briggs, *Org Mass Spec*, (1987), **22**, 91

64. M J Hearn, B D Ratner and D Briggs, *Macromolecules*, (1988), **21**, 2950

65. M J Hearn, D Briggs, S C Yoon and B D Ratner, *Surf Interface Anal*, (1987), **10**, 384

66. D Briggs and H S Munro, *Polym Commun*, (1987), **28**, 307

67. D Briggs and B D Ratner, *Polym Commun*, (1988), **29**, 6

68. M J Hearn and D Briggs, *Surf Interface Anal*, (1988), **11**, 198

69. D Briggs, *Surf Interface Anal*, (1989), **14**, 209

70. D Briggs, *Surf Interface Anal*, (1990), **15**, 734

71. W J van Ooij and R H G Brinkhuis, *Surf Interface Anal*, (1988), **11**, 430

72. A Chilkoti, B D Ratner and D Briggs, *Surf Interface Anal*, (1992), **17**, 397

73. I V Bletsos, D M Hercules, D van Leyen and A Benninghoven, *Macromolecules*, (1987), **20**, 407

74. J Lub, D van Leyen and A Benninghoven, *Polym Commun*, (1989), **30**, 74

75. D van Leyen, B Hagenhoff, E Niehuis, A Benninghoven, I V Bletsos and D M Hercules, *J Vac Sci Technol A*, (1989), **7**, 1790

76. L O'Toole, R D Short, F A Bottino, A Pollicino and A Recca, *Polym Deg Stab*, (1992), **38**, 147

77. R A P Lynn, S S Davis, R D Short, M C Davies, J C Vickerman, P Humphrey, D Johnson and J Hearn, *Polym Commun*, (1988), **29**, 365

78. M C Davies, R D Short, M A Khan, J F Watts, A Brown, A J Eccles, P Humphrey, J C Vickerman and M Vert, *Surf Interface Anal*, (1989), **14**, 115

79. M C Davies, R A P Lynn, J F Watts, A J Paul, J C Vickerman and J Heller, *Macromolecules*, (1991), **24**, 5508

80. M C Davies, M A Khan, A Domb, R Langer, J F Watts and A J Paul, *J Appl Polym Sci*, (1991), **42**, 1597

81. Q S Bhatia and M C Burrell, *Polymer*, (1991), **32**, 1948

82. S Waddington and D Briggs, *Polym Commun*, (1991), **32**, 506

83. P M Thompson, *Anal Chem*, (1991), **63**, 2447

84. M Alexander, *PhD Thesis*, (1992), University of Sheffield

85. L O'Toole, R D Short, F A Bottino, G Di Pasquale and A Pollicino, *Surf Interface Anal*, (1992), **18**, 667

86. E J Vorenkamp and G Challa, *Polymer*, (1988), **29**, 86

87. Reference [5], pp217-224

88. S Krause in *"Polymer Blends"*, ed D R Paul and S Newman, (1978), Academic Press, London, p15

89. J N Razinskaya, B P Shtarkman, L I Batuyeva, B S Tyves and M N Shlykova, *Vysokomol Soedin*, (1979), **A21**, 1860

90. D J Walsh and J G McKeown, *Polymer*, (1980), **21**, 1330

91. H J Jager, E J Vorenkamp and G Challa, *Polym Commun*, (1983), **24**, 290

92. C Tremblay and R E Prud'homme, *J Polym Sci Polym Phys Ed*, (1984), **22**, 1857

93. T G Vargo and J A Gardella, *J Polym Sci Polym Chem Ed*, (1989), **27**, 1267

94. M Clark, C Burkhardt and J A Gardella, *Macromolecules*, (1989), **22**, 4495

95. Reference [30], pp22 and 30

96. J Lub and A Benninghoven, *Org Mass Spec*, (1989), **24**, 164

97. G J Leggett and J C Vickerman, *Appl Surf Sci*, (1992), **55**, 105

98. D Briggs and M J Hearn, *Vacuum*, (1986), **36**, 1005

99. A Ameen, private communication

100. P Denison, private communication.

101. A Brown and J C Vickerman, *Surf Interface Anal*, (1984), **6**, 1

102. The operating pressure in the vacuum during solvent removal was always very close to the base pressure when all the solvent had been removed.

103. The very small lighter coloured specks on the large, dark shaded domain, are contaminants, probably dust, that the sample picked up between removal from the vacuum oven and sputtering with gold.

104. H P Chang and J H Thomas, *J Electron Spectrosc*, (1982), **26**, 203

105. J Brandrup and E H Immergut in *"Polymer Handbook, Third Edition"*, (1989), Wiley, Chichester

106. R O Ansell, T Dickinson, A F Povey and P M A Sherwood, *J Electroanalysis Chem*, (1979), **98**, 79

107. E Adem, R Champaneria and P Coxon, *Vacuum*, (1990), **41**, 1695

108. G Beamson, D Briggs, S F Davies, I W Fletcher, D T Clark, J Howard, U Gelius, D Wannberg and P Balzer, *Surf Interface Anal*, (1990), **15**, 541

109. $1\ dyn\ cm^{-1} \equiv 1\ mN\ m^{-1}$

"Went to one of the great British universities, I suppose...
Oxford...Cambridge...Hull."

E. Blackadder, 1917